INFORMATION TO USERS

This manuscript has been reproduced from the microfilm master. UMI films the text directly from the original or copy submitted. Thus, some thesis and dissertation copies are in typewriter face, while others may be from any type of computer printer.

The quality of this reproduction is dependent upon the quality of the copy submitted. Broken or indistinct print, colored or poor quality illustrations and photographs, print bleedthrough, substandard margins, and improper alignment can adversely affect reproduction.

In the unlikely event that the author did not send UMI a complete manuscript and there are missing pages, these will be noted. Also, if unauthorized copyright material had to be removed, a note will indicate the deletion.

Oversize materials (e.g., maps, drawings, charts) are reproduced by sectioning the original, beginning at the upper left-hand corner and continuing from left to right in equal sections with small overlaps.

Photographs included in the original manuscript have been reproduced xerographically in this copy. Higher quality 6" x 9" black and white photographic prints are available for any photographs or illustrations appearing in this copy for an additional charge. Contact UMI directly to order.

ProQuest Information and Learning
300 North Zeeb Road, Ann Arbor, MI 48106-1346 USA
800-521-0600

Study of Locally Unfolded Forms of Cytochrome c by Fourier Transform Infrared and of H_2O_2-mediated Oxidation of Ferricytochrome c and Metmyoglobin by Mass Spectrometry

Angelo Filosa

A Thesis

In

The Department

Of

Chemistry and Biochemistry

Presented in Partial Fulfillment of the Requirements
for the Degree of Doctor of Philosophy at
Concordia University
Montreal, Quebec, Canada

July 16, 2001

Abstract

Study of Locally Unfolded Forms of Cytochrome c by Fourier Transform Infrared and of H_2O_2-mediated Oxidation of Ferricytochrome c and Metmyoglobin by Mass Spectrometry

Angelo Filosa, Ph.D.
Concordia University, 2001

The reaction of hydrogen peroxide (H_2O_2) with metmyoglobin (Mb) and ferricytochrome c (cyt c) forms highly reactive intermediates that are believed to be important in myocardial reperfusion injuries and in triggering apoptosis, respectively. Furthermore, the alkaline isomer(s) of cyt c have been implicated in the apoptotic process. Hence, a detailed study was performed to characterize the locally unfolded forms of cyts c, and to identify reactive intermediates generated in the cyt c and Mb polypeptide upon their reaction with H_2O_2.

Raising the temperature at neutral pH can induce the alkaline isomerization of cyts c. The intensity of the 695-nm absorption and Fourier transform infrared (FTIR) amide II band as a function of temperature was monitored, revealing that the alkaline form of tuna cyt c appears about 20°C lower (~ 35°C) than those of horse and cow cyts c (~ 55-60°C). This is consistent with an increased susceptibility to proteolytic attack for tuna cyt compared to horse or cow cyts c, as reflected in thermodynamic parameters calculated from 695-nm thermal titration. The cyts c also exhibit increased susceptibility to tryptic digestion at temperatures approaching their alkaline-transition temperature. Curve-fitting of FTIR amide I' bands revealed essentially identical secondary structure in horse and cow cyts c, whereas splitting of α-helical absorption was observed in tuna cyt

c, indicating the presence of less stable helical structures. Nevertheless, these were found not to contribute to the lower alkaline transition temperature of tuna cyt c observed from FTIR analysis of the amide II band. Resolution enhanced 2D IR correlation analysis of the FTIR amide I' band revealed that an extended-chain structure adjacent to the heme unfolds first in tuna cyt c. However, this is the most stable region in horse and cow cyts c, indicating a less stable heme crevice in tuna cyt c compared to the mammalian cyts c. Hence, subtle structural differences located in the heme crevice between the cyts c can explain their different alkaline isomerization temperatures.

In the second part of this thesis, the reactions of H_2O_2 with cyt c and Mb were examined. By monitoring the Soret absorption of cyt c, it was found that the presence of excess H_2O_2 caused heme degradation with no evidence for the formation of an oxyferryl heme intermediate in cyt c on the stopped-flow time scale ($t_{½} < 1$ ms). However, H_2O_2-mediated damage of cyt c was inhibited in the presence of cyanide, confirming that the cyt c/H_2O_2 reaction is ferric heme-mediated. Interestingly, at alkaline pH, cyt c was more resistant to H_2O_2-mediated heme degradation indicating an improved stability compared to native cyt c. Spin-trapping was coupled to peptide mass mapping (ST/LC/MS) to locate protein-based radicals formed during the reaction of cyt c and Mb with H_2O_2. Tyr74 in horse and cow cyts c and Trp33 in tuna cyt c were inferred as possible radical sites formed during the cyt c/H_2O_2 reaction, while Tyr103 was confirmed and Lys42 was inferred as possible radical sites formed during the Mb/H_2O_2 reaction. However, pitfalls inherent in using ST/LC/MS to identify protein-based radical sites were encountered when using 3,5-dibromo-4-nitrosobenzenesulfonic acid (DBNBS) as a spin trap. Noncovalent DBNBS-cyt c mass adducts due to ion-pair formation between the

negatively charged DBNBS and positively charged cyt c were observed in the electrospray mass spectrum, which complicates the analysis of any spin adducts formed.

Acknowledgements

I would like to begin by thanking Dr. Ann English for her guidance, support and endless research ideas during my Ph.D. Her enthusiasm and dedication to research are traits I truly admire and I hope I too will have the same energy with my future research endeavors as she has with hers.

I wish to thank the members of my committee, Drs. Kevin Bateman, Robin Rye and Oswald Tee for some interesting yearly meetings. I would especially like to thank Dr. Joanne Turnbull for agreeing, on such short notice, to serve as an alternate examiner for my thesis defence.

I would like to acknowledge everyone at Concordia that has played some part in my development as a scientist, especially Drs. George Tsaprailis and Craig Fenwick who showed me the "ropes" on the mass spectrometer when I started in the lab. Notable mentions are extended to Line D'Astous, Yazhen Hu, Iolie Bakas, Jim Kolokotronis, Christina Esposito, John Wright, Tyrone Shephard and Drs. Susan Aitkens, Araz Jakalian and Ashraf Ismail. I would particularly like to thank Andrea Romeo who has made the last two years of my Ph.D. extremely entertaining and enjoyable.

I am also appreciative for the introduction to mass spectrometry provided to me Dr. Josie Visentini. I would like to express my thanks to all my football buddies who reminded me that there was a life outside of the lab.

I am grateful to my parents, sisters and in-laws for all the love and support they have given me over the years. Finally, I would like to thank my wife for all her patience, understanding and love. This degree is as much hers as it is mine.

Dedications

To my father,

Giovanni Filosa (1936 – 1996),

Wish you were here;

and to my daughter,

Eva Filosa (April 15, 2001),

For giving me the greatest gift in life.

Table of Contents

List of Figures xiii

List of Tables xviii

List of Abbreviations xix

1.0 Introduction 1

1.1 Structure of Cytochrome c 1
1.2 Alkaline Isomerization of Ferricytochromes c 4
1.3 Oxidation of Ferricytochrome c and Metmyoglobin by H_2O_2 7
1.4 Overview of Techniques Used in the Thesis 9
1.4.1 Fourier Transform Infrared Spectroscopy 9
1.4.2 Spin Trapping Coupled with Liquid Chromatography/ Electrospray Mass Spectrometry 11
1.5 Hypotheses, Scope and Organization of Thesis 13
1.6 Contributions of Colleagues 15

2.0 Probing Local Thermal Stabilities of Bovine, Horse and Tuna Ferricytochromes c at pH 7 17

2.1 Abstract 17
2.2 Introduction 18
2.3 Experimental 20
2.4 Results and Discussion 21
2.4.1 Temperature Dependence of the Soret Maxima 21
2.4.2 Temperature Dependence of the 695-nm Absorbance 22
2.4.3 Analysis of the Local Stability of Cytochromes c by Limited Proteolysis 24
2.4.4 Properties of the Low and High Temperature Conformers 26

2.4.5 Structural Basis for Differences in Thermodynamic and Local Stabilities of the Cytochromes c 33
2.5 Conclusions 34

3.0 FTIR-monitored Thermal Titration Reveals Different Mechanisms for the Alkaline Isomerization of Tuna Compared to Horse and Bovine Cytochromes c 36

3.1 Abstract 36
3.2 Introduction 37
3.3 Experimental Procedures 40
3.3.1 Materials 40
3.3.2 Methods 41
3.4 Results and Discussion 42
3.4.1 Thermal Titration of the FTIR Spectra of the Cytochromes c at pD 7.0 42
3.4.2 Implications of the FTIR Results for the Mechanism of Alkaline Isomerization of Tuna vs Horse and Bovine Cytochromes c 48
3.4.3 Curve Fitting of the Amide I/I' Regions of the 25°C FTIR Spectra 51
3.4.4 Structural Basis for Splitting of α-helical Absorption in Tuna Cytochrome c 59
3.5 Conclusions 62

4.0 Two-dimensional Infrared Correlation Spectroscopy as a Probe of Sequential Events in the Thermal Unfolding of Cytochromes c 64

4.1 Abstract 64
4.2 Introduction 65
4.3 Experimental Procedures 67
4.3.1 IR Spectroscopy 67

4.3.2 2D IR Analysis 68
4.3.3 Interpretation of 2D IR Correlation Plots 69
4.4 Results and Discussion 69
4.4.1 Thermal Unfolding of Horse, Cow and Tuna Cyts c 69
4.4.2 2D IR Correlation Plots of Horse Cyt c 71
4.4.3 2D IR Correlation Plots of Cow Cyt c 78
4.4.4 2D IR Correlation Plots of Tuna Cyt c 80
4.5 Conclusions 84

5.0 Heme-mediated Oxidation of Ferricytochrome c by H_2O_2: An Apoptotic trigger? 86

5.1 Abstract 86
5.2 Introduction 87
5.3 Experimental Procedures 90
5.3.1 Materials 90
5.3.2 UV/Vis Studies 90
5.3.3 Mass Spectrometry 90
5.4 Results and Discussion 91
5.4.1 UV/Vis Monitoring of the Ferricytochrome c/H_2O_2 Reaction 91
5.4.2 Trapping Protein-based Radicals Formed in the Ferricytochrome c/H_2O_2 Reaction 95
5.5 Conclusions 100

6.0 Mass Spectral Analysis of Protein-based Radicals Using DBNBS: Non Radical Adduct Formation vs Spin Trapping 106

6.1 Abstract 106
6.2 Introduction 107
6.3 Experimental Procedures 109
6.3.1 Materials 109
6.3.2 Methods 109

6.4 Results and Discussion 110
6.4.1 Analysis of DBNBS Mass Adduct Formation with Ferricytochrome c in the Presence and Absence of H_2O_2 110
6.4.2 Analysis of DBNBS Mass Adduct Formation with Metmyoglobin and α-lactalbumin in the Presence and Absence of H_2O_2 116
6.4.3 DBNBS Adduct Formation with Horse Cyt c in the Absence of H_2O_2 at pH 2.0 119
6.5 Conclusions 124

7.0 A Mass Spectrometric Investigation of Protein-based Radicals Formed in the Metmyoglobin/H_2O_2 Reaction using DBNBS 126

7.1 Abstract 126
7.2 Introduction 126
7.3 Experimental Procedures 128
7.3.1 Materials 128
7.3.2 Spin Trapping 129
7.3.3 Peptide Mass Mapping 129
7.3.4 Peptide Sequencing 130
7.3.5 Analysis of Electron-transfer Pathways in Mb 130
7.4 Results and Discussion 131
7.4.1 DBNBS Mass Adduct Formation in the Mb/H_2O_2/DBNBS Reaction 131
7.4.2 pH Dependence of DBNBS Spin Trapping in the Mb/H_2O_2 Reaction 133
7.4.3 Peptide Mass Mapping of Mb/H_2O_2/DBNBS Reaction Products 135
7.4.4 Absorption Difference Spectroscopy of Mb/H_2O_2 Reaction Products 142
7.4.5 Analysis of Electron-transfer Pathways in Mb 143
7.5 Conclusions 148

8.0 Conclusions and Suggestions for Future Work 150

8.1 Chapters 2, 3 and 4 150
8.2 Chapters 5 and 6 151
8.3 Chapter 7 152
8.4 Suggestions for Future Work 153

9.0 References 155

List of Figures

Figure 1.1. Amino acid sequences of horse, cow and tuna cytochromes c. 2

Figure 1.2. C_α backbone horse heart ferricytochrome c with its heme (red) and its two axial ligands, Met80 (green) and His18 (yellow). 3

Figure 2.1. Soret absorption maxima vs temperature of 19-22 μM (■) cow, (◆) horse, and (Δ) tuna ferricytochromes c. 23

Figure 2.2. van't Hoff plots for (a) cow, (b) horse, and (c) tuna ferricytochromes c. 28

Figure 2.3. Time course of tryptic digestion at (a) 37°C and (b) 25°C of (■) cow, (◆) horse and (Δ) tuna ferricytochromes c, and (c) the extent of tryptic digestion over 3 h of each cytochrome at different temperatures in 50 mM sodium phosphate/0.2 M KCl buffer, pH 7.0. 30

Figure 2.4 Electronic absorption spectra of 19-22 μM (a) cow and (b) horse ferricytochromes c at 25°C (——), 50°C (– – –), 65°C (·····) and 78°C (– ·· –), and (c) tuna ferricytochrome c at 25°C (——), 45°C (– – –), 60°C (·····) and 78°C (– ·· –). 31

Figure 3.1. Deconvolved spectra in the amide I' (D_2O) region of 4 mM horse cytochrome c in 50 mM sodium phosphate/0.2 M KCl buffer (pD 7.0) vs temperature. 44

Figure 3.2. Plot of the integrated intensities of the (Δ) amide I' (1700-1600 cm^{-1}) and (o) residual amide II (1600-1525 cm^{-1}) bands of (a) horse, (b) cow and (c) tuna cytochromes c at pD 7.0 vs temperature. 46

Figure 3.3. Plot of the integrated intensities of the (Δ) amide I' (1700-1600 cm^{-1})

and (o) amide II (1560-1525 cm^{-1}) bands at pD 7.0 vs temperature for the CN^--adducts of (a) horse and (b) tuna cytochromes c. 50

Figure 3.4. Deconvolved and curve-fitted FTIR spectra in the amide I (H_2O) and I' (D_2O) regions of (a,b) horse, (c,d) cow and (e,f) tuna cytochromes c. 54

Figure 3.5. Deconvolved and curve-fitted FTIR spectra in the amide I' (D_2O) region of the CN^--adducts of (a) horse and (b) tuna cytochromes c. 60

Figure 4.1. Horse heart cyt c C_α backbone with its heme (red), helical (yellow), turns (green) and extended-chain (blue) structures. 66

Figure 4.2. Stacked absorbance vs temperature (25-81°C) plots of the deconvolved amide I' (D_2O) bands of 4 mM (a) horse, (b) cow and (c) tuna cyts c in 50 mM sodium phosphate buffer containing 0.2 M KCl (pD 7.0). 73

Figure 4.3. 2D IR (a, c) synchronous and (b, d) asynchronous maps of the amide I' absorption of horse cyt c constructed from the spectral data in Figure 4.2a. 77

Figure 4.4. 2D IR (a, c) synchronous and (b, d) asynchronous maps of the amide I' absorption of cow cyt c constructed from the spectral data in Figure 4.2b. 82

Figure 4.5. 2D IR (a, c) synchronous and (b, d) asynchronous maps of the amide I' absorption of tuna cyt c constructed from the spectral data in Figure 4.2c. 83

Figure 5.1. Structures of (a) α-(4-Pyridyl-1-oxide)-N-t-butylnitrone (POBN), (b) 5,5-dimethylpyrroline-N-oixde (DMPO), (c) 2-methyl-2-nitroso propane (MNP) and (d) 3,5-dobromo-4-nitrosobenzenesulfonate

(DBNBS) spin traps. 89

Figure 5.2. Absorption spectra of 10 μM horse cyt c plus (a) 10 μM, (b) 100 μM, (c) 1 mM and (d) 10 mM H_2O_2; and of (e) tuna and (f) cow cyts c plus 10 mM H_2O_2. 94

Figure 5.3. Absorption spectra of 10 μM (a) horse, (b) tuna and (c) cow cyts c plus 3 mM KCN recorded 20 min after the addition of 10 mM H_2O_2. 96

Figure 5.4. Observed pseudo-first-order rate constants (k_{obs}) vs pH for heme degradation in 10 μM horse (• —) and tuna (■ - - -) cyts c by 12 mM H_2O_2. 97

Figure 5.5. Deconvolved ESI mass spectra of the products of a 10-min reaction of 500 μM horse cyt c with 2.5 mM H_2O_2 in the presence of (a) 20 mM MNP and (b) 50 mM DMPO. 101

Figure 5.6. Deconvolved ESI mass spectra of the products of a 10-min reaction of 500 μM (a) cow and (b) tuna cyts c with 2.5 mM H_2O_2 in the presence of 50 mM POBN. 102

Figure 5.7. Peptide mass maps and extracted-ion chromatograms of (a) POBN-modified horse, (b) native horse, (c) POBN-modified tuna and d) native tuna cyts c. 103

Figure 6.1. Deconvolved ESI mass spectra of the products of a 10-min reaction of 500 μM cyt c with H_2O_2 in the presence of 10 mM DBNBS. 113

Figure 6.2. Absorption spectra of 132 μM DBNBS following a 10-min incubation with 660 μM H_2O_2 (trace 1) and untreated 111 μM DBNBS (trace 2). 114

Figure 6.3. Deconvolved ESI mass spectra of the products of a 10-min reaction of 500 μM horse heart metmyoglobin with H_2O_2 in the presence of 10 mM DBNBS: with 2.5 mM H_2O_2 (a); without H_2O_2 (b); and with 500 μM H_2O_2 (c). 120

Figure 6.4. Deconvolved ESI mass spectra of the products of a 10-min reaction of 500 μM α-lactalbumin with H_2O_2 and 10 mM DBNBS: with 2.5 mM H_2O_2 (a); and without H_2O_2 (b). 121

Figure 6.5. Soret absorption spectra of 10 μM non-oxidized (a) and oxidized (b) horse cyt c incubated for 30 min in 0.05% TFA (pH 2.0) in the presence of 0 (trace 1), 1 (trace 2), 5 (trace 3), 15 (trace 4), 20 (trace 5) and 25 (trace 6) molar equivalents of DBNBS. 122

Figure 6.6. Deconvolved ESI mass spectra of 20 μM horse cyt c incubated for 30 min in 0.05% TFA (pH 2.0) in the presence of 0 (a), 1 (b), 10 (c), 15 (d), 20 (e) and 25 (f) molar equivalents of DBNBS. 123

Figure 7.1. Deconvolved ESI mass spectra of the products of the reaction of 500 μM Mb and 10 mM DBNBS with (a) 2.5 mM H_2O_2, (b) 5 mM and (c) 500 μM H_2O_2. 134

Figure 7.2. Deconvolved ESI mass spectra of the products the reaction of 500 μM Mb and 10 mM DBNBS with (a) 0.5 mM H_2O_2 at pH 5, (b) 2.5 mM H_2O_2 at pH 5, (c) 2.5 mM H_2O_2 at pH 6.6 and (d) 2.5 mM H_2O_2 at pH 8.65. 136

Figure 7.3. LC/ESI-MS peptide mass maps of (a) R-DBNBS-labeled Mb and (b) native Mb. 138

Figure 7.4. MALDI-TOF peptide mass maps of (a) R-DBNBS-labeled Mb and (b) native Mb. 139

Figure 7.5. Mass spectrometric sequencing of R-DBNBS-modified tryptic peptide (a) 97-118 by MALDI PSD, (b) 103-118 by LC/MS/MS and (c) the predicted y and b fragment ions. 140

Figure 7.6. Absorption spectra of 111 μM DBNBS (trace 1), and difference absorption spectrum of the HPLC-purified products from the Mb/H_2O_2/DBNBS (1:5:20) reaction minus those from the Mb/H_2O_2 (1:5) reaction (trace 2). 144

Figure 7.7. C_α backbone of horse heart myoglobin with its heme (red) and potential electron donors to the heme (black). 145

List of Tables

Table 2.1. Thermodynamic parameters[a] for the heme-crevice transitions of cow, horse and tuna ferricytochromes c as determined from the temperature dependence of their 695-nm absorption band. 29

Table 2.2. Transition temperatures for the alkaline isomerization of ferricytochromes c. 32

Table 3.1. Curve-fitting Parameters [Frequency (ν, cm^{-1}), % Area, and HWHH (cm^{-1})] for FTIR Amide I and I' Bands of Native Horse, Cow, and Tuna Cytochromes c and the CN^--Adducts of the Horse and Tuna Proteins[a] 55

Table 3.2. Assignment of Secondary Structural Elements to FTIR Amide I and I' Absorption Bands for Native Horse, Cow, and Tuna Cytochromes c and the CN^--Adducts of the Horse and Tuna Proteins 56

Table 3.3. Comparison of Amide I and I' Assignment for Horse, Cow, and Tuna Cytochromes c with Literature FTIR, X-ray and NMR Data 57

Table 4.1. Correlation table for the deconvolved FTIR spectra of horse cyt c over the temperature range 25-81°C[a-e] 74

Table 4.2. Correlation table for the deconvolved FTIR spectra of cow cyt c over the temperature range 25-81°C[a-e] 75

Table 4.3. Correlation table for the deconvolved FTIR spectra of tuna cyt c over the temperature range 25-81°C[a-e] 76

List of Abbreviations

A	acceptor
ACN	acetonitrile
ANS	8-anilino-1-naphthalenesulfonate
CD	circular dichroism
CID	collision induced dissociation
CN^-	cyanide anion
Cyt c	ferricytochrome c
D	donor
DBNBS	3,5-dibromo-4-nitrosobenzenesulfonic acid
$DBNBS^{\bullet+}$	oxidized DBNBS
DMPO	5,5-dimethylpyrroline-N-oxide
DTPA	diethylenetriamine-N,N,N',N",N"-pentaacetic acid
EPR	electron paramagnetic resonance
ESI	electrospray ionization
FPLC	fast protein liquid chromatography
FSD	Fourier self-deconvolution
FTIR	Fourier transform infrared
H/D	hydrogen/deuterium;
HWHH	half-width-at-half-height
HPLC	high-presssure liquid chromatography

H_2O_2	hydrogen peroxide
IMAC	immobilized metal-affinity chromatography
K_d	dissociation constant
K factor	enhancement factor
$OH^{\bullet}$	hydroxyl radical
LC/MS	liquid chromatography with mass spectrometric detection
MALDI-TOF	matrix-assisted laser desorption ionization-time-of-flight
Mb	metmyoglobin
MNP	2-methyl-2-nitrosopropane
$MNP^{\bullet+}$	oxidized MNP
MS	mass spectrometry
MS/MS	tandem mass spectrometry
NaPi	sodium phosphate
NMR	nuclear magnetic resonance
POBN	α-(4-Pyridyl-1-oxide)-N-t-butylnitrone
PSD	post-source decay
R	lipids
R-DBNBS	reduced-DBNBS adduct
ROS	reactive oxygen species
ST/LC/MS	coupling spin trapping to liquid chromatography with mass spectrometric detection
TFA	triflouroacetic acid
T_{DA}	electronic matrix element
T_c	transition temperature

T_m	midpoint temperature
XIC	extracted ion chromatogram
$X^{\bullet}$	radical species in the form of a porphrin π-cation radical or an amino acid radical
$XST^{\bullet}$	spin adduct of $X^{\bullet}$
XMA	diamagnetic mass adduct of $X^{\bullet}$
2D IR	two-dimensional infrared
$\Delta G°$	Gibbs free energy

1.0 Introduction

1.1 Structure of Cytochrome c

Cytochrome c (cyt c) is a small (MW ~ 12 kDa) water soluble heme protein that exists in the cytosol between the inner and outer membranes of mitochondria. Its function is to mediate one step in the transfer of electrons along the respiratory chain in eukaryotes, where electrons are shuttled from cytochrome c reductase to cytochrome c oxidase which reduces dioxygen to water. Figure 1.1 contains the amino acid sequences from horse, cow and tuna cyts c. The crystal structures of five eukaryotic cyts c from horse, tuna, yeast, rice and bonito have been determined, revealing that cyt c (Figure 1.2) consists of a single polypeptide chain with a globular tertiary structure, and a covalently bound heme buried within the hydrophobic interior of the protein (*1, 2*). Only about ~ 4-7% of the heme is exposed at the molecular surface (*1, 2*). All of the internal residues in van der Waals contact with the heme are bulky hydrophobic groups, which contribute to the stability of cyt c. The polypeptide chain is organized into five α-helical segments that contain ~ 45% of the amino acids, interconnected by turns and loops. In eukaryotic cyts c the heme prosthetic group is covalently bonded by thioether bonds to Cys14 and Cys17 (*1-3*). The six-coordinate, low-spin iron present in the heme is coordinated to four nitrogens on the porphyrin ring and the fifth and sixth axial positions are occupied by a relatively weak bond between the iron and the sulfur of Met80, and a stronger bond between the iron and N3 of His18 (*4, 5*). The Fe^{III}-S(Met80) bond gives rise to an absorption band at 695 nm (*4-7*) which is believed to arise from a porphyrin $\rightarrow Fe^{III}$ transition (*1, 8*). The electronic transition involved is

```
          1                 10                  20                  30
Horse     GDVEKGKKIF VQKCAQCHTV EKGGKHKTGP
Cow       GDVEKGKKIF VQKCAQCHTV EKGGKHKTGP
Tuna      GDVAKGKKTF VQKCAQCHTV ENGGKHKVGP

                    40                  50                  60
Horse     NLHGLFGRKT GQAPGFTYTD ANKNKGITWK
Cow       NLHGLFGRKT GQAPGFSYTD ANKNKGITWG
Tuna      NLWGLFGRKT GQAEGYSYTD ANKSKGIVWN

                    70                  80                  90
Horse     EETLMEYLEN PKKYIPGTKM IFAGIKKKTER
Cow       EETLMEYLEN PKKYIPGTKM IFAGIKKKGER
Tuna      NDTLMEYLEN PKKYIPGTKM IFAGIKKKGER

                  100
Horse     EDL I AYLKKATNE
Cow       EDL I AYLKKATNE
Tuna      QDLVAYLKSATS
```

Figure 1.1. Amino acid sequences of horse, cow and tuna cytochromes c (*1*).

Figure 1.2. C_α backbone horse heart ferricytochrome c with its heme (red) and its two axial ligands, Met80 (green) and His18 ( ). This model was generated using Rasmol from the crystal-structure coordinates in the Protein Data Bank, entry 1HRC (*2*).

not known but the correlation with Met80 ligation is due to the influence of the axial ligand on the iron d-orbitals (*1*). The Fe^{III}-S(Met80) bond is sensitive to the conformational state of the protein, as seen by displacement of Met80 by exogenous high-affinity ligands, such as cyanide (CN^-), or by small changes in temperature, pH or ionic strength, which can be easily monitored via the 695-nm band (*5, 7, 8*).

1.2 Alkaline Isomerization of Ferricytochromes c

Cyts c possess remarkably similar secondary and tertiary structures, despite their relatively low sequence homology (*1, 2*). Nonetheless, cyts c from different species exhibit different local stabilities as probed by tryptic digestion (*9-11*) and 695-nm absorption (*4, 8, 11, 12*). Differences in the local stability can be attributed to differences in flexibility of the Met80 loop of the various cyts c, as seen for example, in the protease susceptibility of metalloderivatives of horse cyt c (*10*). This study revealed that the strength of Met80 ligation is the main determinant of *local* conformational stability since weakening or removal of the metal-Met80 bond greatly increased the local flexibility of the protein.

The well-documented alkaline isomerization of horse cyt c is also associated with increased flexibility about the Met80 loop (*1, 13*). The alkaline isomer(s) are reported to possess six-coordinate low-spin heme iron that retains His18 ligation but substitute Met80 ligation by one or more unknown strong-field ligand(s) (*1*). The process is complex involving ionization with a pK_a of 11, followed by conformational change and ligand replacement with a pK_c of -2 at room temperature (*14*):

$$H^+N_{H/M} \overset{K_a}{\rightleftharpoons} N_{H/M} + H^+ \quad (1.1)$$

$$N_{H/M} \overset{K_c}{\rightleftharpoons} A_{H/X} + A_{H/Y} \quad (1.2)$$

where $N_{H/M}$ refers to the native protein with His18 and Met80 ligation, and $A_{H/X}$ and $A_{H/Y}$ to alkaline conformations with His18 and different axial sixth ligands (*13, 15-19*). The identity of the group that ionizes in eqn 1.1 is unknown but is speculated to be a Lys residue (*16, 18*). The X and Y ligands in eqn 1.2 are proposed to be Lys72 and Lys79 in horse cyt c (*19*), and Lys73 and Lys79 in yeast cyt c (*18*), where Lys72 is trimethylated. The temperature dependence of the *apparent* pK_a ($pK_{app} = pK_a + pK_c$), which is ~ 9 at 25°C, arises mainly from that of K_c in step 2 (*13, 14*). Nuclear magnetic resonance (NMR) experiments have established the interdependence between the pH- and temperature-induced local conformational changes occurring during the conversion of native horse cyt c to its alkaline isomers (*13*).

The biological relevance of its alkaline isomer(s) lies in the fact that upon binding to some of its biological partners (*20*) or associating with synthetic anionic phospholipid vesicles (*21*) cyt c undergoes conformational changes related to its alkaline isomerization. This suggests that cyt c is in the alkaline form when bound to the phospholipid-rich inner mitochondrial membrane and during electron transfer. Furthermore, the phospholipid-bound form of cyt c exhibits a decreased reduction potential (*22*) compared to native cyt c (225 vs 273 mV), which facilitates electron transfer, lending credence to its importance.

The role of cyt c as an electron-transfer protein in the mitochondria has been known for quite a long time (*1*). However, cyt c was only recently identified as one of the factors necessary for activation of cell-death proteases during apoptosis (*23*). Once again the alkaline form of cyt c plays an important role in its function, since a conformational change in mouse cyt c resembling that of the alkaline isomer(s) was found to activate caspases in apoptotic and necrotic T hybridoma cells (*24*). Interestingly, apoptosis induced in Jurkat cells by staurosporine or ultraviolet irradiation resulted in rapid mitochondrial alkalinization (from pH 7.8 to 8.5), followed by cyt c release, caspase activation and mitochondrial swelling/depolarization, suggesting that change in intracellular pH may be an early event that regulates apoptosis (*25*). Mitochondrial alkalinization would enhance the formation of alkaline forms of cyt c, since the apparent pK_a for its alkaline isomerization is ~ 9 (*14*). Furthermore, it was observed that cyt *c* preparations from various vertebrate species but not from *Saccharomyces cerevisiae*, which forms an altered alkaline isomer(s) compared to eukaryotic cyts c since it is trimethylated at Lys72, were able to initiate all signs of apoptosis in *Xenopus* egg extracts and murine interleukin-3 dependent cells (*26, 27*). Interestingly, the redox activity of cyt c, which is essential for its function in the respiratory chain, is not required for its cytosolic pro-apoptotic activity, indicating that critical protein-protein interactions are involved in the apoptosomic complex (*26-28*). The cited studies establish the importance of the alkaline isomer(s) of cyt c in its contrasting functions in electron-transfer and apoptosis.

1.3 Oxidation of Ferricytochrome c and Metmyoglobin by H_2O_2

Reactive oxygen species (ROS), such as superoxide and H_2O_2, are generated by all aerobic cells as byproducts of metabolic reactions and in response to various stimuli. H_2O_2 is produced via the dismutation of superoxide or the incomplete reduction of dioxygen (*29*). Under normal physiological conditions, levels of H_2O_2 are kept relatively low (10^{-9}-10^{-7} M) by antioxidant enzymes such as glutothione peroxidase (*29*) and catalase (*30, 31*). However, the damage caused to mitochondria during oxidative stress, which is an excess production of ROS, includes lipid peroxidation (*30-32*), protein oxidation (*32, 33*), mitochondrial DNA mutation (*32, 34*) and the initiation of apoptosis (*32, 35, 36*). Cyt c, present in mM concentrations in the intermembrane space, has been implicated in mitochondrial damage via its reaction with H_2O_2, which has been shown to produce highly reactive species that are capable of oxidizing peptides (*37*), organic substrates (*38*) and initiate lipid peroxidation (*30, 31, 39*). Initially, it was believed that cyt c damage was caused by conversion of H_2O_2 to the highly reactive hydroxyl radical ($OH^{\bullet}$) in Fenton-like reactions (eqn 1.3-1.4) or by Haber-Weiss-type reactions (eqn 1.5-1.7), resulting in hydrogen abstraction from lipids (R) by $OH^{\bullet}$ (*40, 41*). However, it was demonstrated that

$$HOOH + Fe^{II} \rightarrow Fe^{III} + OH^{-} + OH^{\bullet} \quad (1.3)$$

$$OH^{\bullet} + RH \rightarrow R^{\bullet} + H_2O \quad (1.4)$$

$$HOOH + Fe^{III} \rightarrow Fe^{II} + O_2^{\bullet -} + 2H^{+} \quad (1.5)$$

$$HOOH + Fe^{II} \rightarrow Fe^{III} + OH^{-} + OH^{\bullet} \quad (1.6)$$

$$O_2^{\bullet -} + Fe^{III} \rightarrow Fe^{II} + O_2 \quad (1.7)$$

cyt c-catalyzed peroxidation of phosphatidylcholine liposomes by H_2O_2 was not inhibited by hydroxyl radical scavengers such as benzoate and dimethylsulfoxide, nor by the metal chelator, diethylenetriamine-N,N,N',N",N"-pentaacetic acid (DTPA), but was inhibited by CN^-, which binds to the heme iron of cyt c by displacing Met80 (*30*). Increasing evidence suggests that the reaction of cyt c with H_2O_2 produces a highly reactive oxyferryl heme ($Fe^{IV}=O$) and transient protein-based radical species ($X^{\bullet}$) in an analogous fashion to heme peroxidases (*30, 31, 37, 38, 42-46*). For example, in the reaction of H_2O_2 with cytochrome c peroxidase, heterolytic cleavage of the O-O bond presumably forms $Fe^{V}=O$ (eqn 1.8) and rapid intramolecular electron transfer from an amino acid residue reduces the $Fe^{V}=O$ moiety to $Fe^{IV}=O$ (eqn 1.9). Thus, one oxidizing equivalent remains at the heme iron and one is stored as $X^{\bullet}$ on Trp191 to yield the intermediate termed Compound I (*47*).

$$HOOH + XFe^{III} \rightarrow XFe^{V}=O + H_2O \qquad (1.8)$$

$$XFe^{V}=O \rightarrow X^{\bullet}Fe^{IV}=O \qquad (1.9)$$

Compound I

There is no direct evidence for the formation of compound I-type species in cyt c, since no spectral intermediates were observed following manual mixing of H_2O_2 and cyt c. Thus, any $Fe^{IV}=O$ species are short-lived ($t_{½}$ < 2 s) (*41*), while the bimolecular rate constant for $Fe^{IV}=O$ formation via reaction 1.8 likely falls between that of horse heart metmyoglobin (210 $M^{-1}s^{-1}$), and cytochrome c peroxidase (1.4 x 10^7 $M^{-1}s^{-1}$) (*48, 49*). Trapping of a tyrosyl radical generated in cyt c on reaction with H_2O_2 by the spin trap 2-methyl-2-nitroso propane (MNP) was detected by electron paramagnetic resonance (EPR), suggesting a tyrosine residue as a possible site for $X^{\bullet}$ formation (eqn 1.9) (*45*).

Furthermore, using the spin trap 3,5-dibromo-4-nitrosobenzenesulfonate (DBNBS), peaks corresponding to $(DBNBS)_n$-cyt c adducts with n = 1-4 were observed by matrix-assisted laser desorption ionization time-of-flight (MALDI-TOF), suggesting that as many as four $X^\bullet$ species were trapped by DBNBS during the reaction of horse cyt c with 5 molar equivalents of H_2O_2 (*37, 45*). Tyr74 was identified as a possible site for radical formation in the cyt c/H_2O_2 reaction by combining spin trapping and peptide mass mapping (*44, 50*). However, there is still much debate as to the translocation and specific location(s) of $X^\bullet$ on the cyt c polypeptide.

Recently, Slezak and coworkers (*51*) demonstrated that H_2O_2 was produced upon introduction of oxygen-containing perfusate to an ischemic heart. Formation of compound I-type species of metmyoglobin (Mb) has been detected in isolated ischemic-reperfused rat hearts (*52*) and such species are considered important in the development of myocardial reperfusion injuries after a period of ischemia (*53, 54*). Presumably, the excess H_2O_2 produced during reperfusion can react readily with Mb, which is present at mM concentrations in cardiac myocytes. Several amino acids have been proposed as sites of $X^\bullet$ formation in Mb upon its reaction with H_2O_2 (eqn. 1.8 and 1.9), including tyrosine, lysine, histidine, phenylalanine and tryptophan (*48, 55-62*). The most convincing evidence, however, points to Tyr103 as the major site of $X^\bullet$ formation in the Mb/H_2O_2 reaction.

1.4 Overview of Techniques Used in the Thesis

1.4.1 Fourier Transform Infrared Spectroscopy

Fourier transform infrared (FTIR) spectroscopy is a highly sensitive probe of protein conformation under a variety of experimental conditions (*63, 64*). This has been clearly demonstrated in its ability to distinguish structural differences between the oxidized and reduced forms of cyt c (*65*). Secondary structural information is obtained from the amide I region (H_2O), which is composed primarily of peptide carbonyl stretching vibrations. These vibrations are sensitive to backbone conformation and the degree of H-bonding of the carbonyls (*63*). Upon deuteration the amide I band downshifts by ~ 5 cm^{-1} (and is labelled the amide I' band) due to small contributions to the amide I mode from peptide NH in-plane-bending vibrations (*63*).

Fourier self-deconvolution (FSD) can be used to enhance the resolution of spectral data by separating overlapping spectral features that cannot be resolved by collecting data at a higher resolution setting. By setting two parameters, bandwidth, which is an estimate of the widths of the overlapped bands and enhancement, which is a measure of the degree to which the data are resolved experimentally, the FSD process can be controlled to optimize the resolving power applied to the data. One can obtain a quantitative estimate of secondary structural elements in a protein by curve-fitting the FSD amide I (H_2O) or amide I' (D_2O) bands. If it is assumed that the amide I absorptivities of the secondary structural elements are the same, the areas under the curve-fitted bands correspond to the number of residues found in a given secondary structure (*65, 66*).

The FTIR amide II bands are composed primarily of NH bending vibrations of peptide groups, which red-shift following deuteration (*21, 67, 68*). By monitoring H/D exchange of the peptide protons using amide II band-intensity, one can gain insight into

tertiary folding states of proteins (*63, 64*). For example, Holzbaur and coworkers identified unfolding intermediates with increased solvent accessibility but intact secondary structures on heating horseradish and cytochrome c peroxidases by following peptide H/D exchange at temperatures well below those required for secondary structure unfolding (*68*).

To enhance the power of FTIR in probing protein conformation, a more sensitive analysis method, two-dimensional infrared (2D IR), has been recently developed. This method can detect subtle out-of-phase variations due to non-cooperative events (69). For example, 2D IR analysis revealed that the Cro repressor protein forms stable intermediates only after specific secondary structures are unfolded, which could not be inferred from 1D FSD analysis (*69*). Similarly, Wang and coworkers (*70*) observed ovalbumin protein peaks by 2D IR that were not detected in either raw or second-derivative 1D spectra. Synchronous and asynchronous 2D correlation plots are generated, which represent the in-phase and out-of-phase variation, respectively, between spectral components to an applied perturbation. The synchronous contour plot yields information similar to that obtained from conventional 1D FTIR analysis, whereas the asynchronous contour plot provides details on the sequence of events following the applied perturbation (*71*).

1.4.2 Spin Trapping Coupled with Liquid Chromatography/Electrospray Mass Spectrometry

Protein-based radicals (such as $X^{\bullet}$ generated in eqn 1.9) are often difficult to detect because they are short-lived and highly reactive. As a result, the technique of

spin trapping has been frequently used in EPR investigations (*72*). Spin traps are diamagnetic compounds that react with $X^{\bullet}$ to form more stable paramagnetic adducts ($XST^{\bullet}$). EPR analyses have been successfully used to provide information on the radical centers of $XST^{\bullet}$ species and their environments (*72, 73*). However, one shortcoming of this technique is that the *specific sites* of radical formation in proteins are often difficult to identify. For example, since horse cyt c contains four tyrosine residues (Tyr48, 67, 74 and 97) (*1*), EPR analysis will not unambiguously identify on which tyrosine $XST^{\bullet}$ is formed. Given that the formation of $XST^{\bullet}$ results in an increased mass of the compound of interest, high-performance liquid chromatography (HPLC) and mass spectrometry (MS) has been successfully combined to identify spin adducts of various small molecules (*74-76*). Our research group has extended this use of LC/MS to proteins, to overcome the inherent limitations of EPR. We have found that reduction of $XST^{\bullet}$ gives rise to a more stable diamagnetic mass adduct (XMA) and permits the assignment of $X^{\bullet}$ to a *specific amino acid* when spin trapping and on-line peptide mass mapping (ST/LC/MS) are coupled (*55, 56, 77-79*). In addition to increased specificity, ST/LC/MS offers enhanced sensitivity over EPR, since considerably smaller quantities (picomole vs nanomole) of sample can be analyzed (*45*).

As with any technique, ST/LC/MS possesses certain limitations. For example, accessibility of spin traps to buried radicals will be limited. For studies on proteins, it is important to use spin traps that are water soluble, stable at room temperature and in light (*72, 80*). Also, the reduction potential of the trap must be out of reach of any oxidant generated in the system of interest to prevent inverted spin trapping. This occurs when an oxidized form of the spin trap is formed that can oxidize an amino acid

residue and produce the same spin adduct results as "normal" spin trapping of a protein radical [reviewed in (*73*)]. To avoid inverted spin trapping in the reactions of interest here, traps with $E° < 1.5$ V were not used since oxyferryl hemes exhibit $E°$ ($Fe^{IV}=O/Fe^{III}$) values of ~ 1 V (*81*). Spin trapping artifacts have also been observed through nonradical reactions, such as the ene reaction between the nitroso group in DBNBS and a double bond in tryptophan (*82*), which gives rise to a spin adduct. Finally, when using the ST/LC/MS technique it is imperative to distinguish between noncovalent and covalent mass-adducts formation. This is discussed in detail in Chapter 6 of this thesis (*55*) for reactions involving the negatively charged DBNBS trap and the highly positively charged cyt c molecule.

1.5 Hypotheses, Scope and Organization of Thesis

The alkaline isomer(s) of cyt c have been proposed to be the form(s) cyts c adopt when bound to the phospholipid-rich inner mitochondrial membrane (*21*) and upon binding to some of its biological partners (*20*), hence, playing a role in electron transfer. The alkaline form(s) of cyt c were also identified as necessary factors for activation of cell-death proteases during apoptosis (*23*).

In examining the alkaline isomer(s) of cyt c, it was postulated that differences in local stability between cyts c were correlated with the flexibility of the Met80 loop. Hence, in Chapter 2, the heme absorption band vs temperature was monitored to detect changes in ligation associated with the alkaline isomers. The intensity of the 695-nm absorption band was also monitored to establish the heme-crevice stabilities of the three cyts c. Furthermore, tryptic digestion was used to determine whether the Met80 loop

controls the local stability in all three cyts c. In Chapter 3, insight into differences in conformational stability between cyts was obtained from an examination of the temperature dependence of their FTIR spectra. Thermal titration of FTIR amide II spectra was performed to identify stable tertiary intermediates formed in the denaturation of the three cyts c. Curve-fitting of the FTIR amide I' bands was also performed to probe differences between the cyts c in order to provide a structural basis for the different alkaline isomerization mechanism. Finally, to determine the sequential events involved in the thermal unfolding of the three cyts c, generalized resolution enhanced 2D IR correlation analysis was used in Chapter 4.

The reaction of H_2O_2 with heme proteins forms highly reactive Fe^{IV}=O and $X^{\bullet}$ species (eqn 5.1) that are considered important in cardiolipin peroxidation, which is proposed to be a primary event that triggers cyt c release from mitochondria in the apoptotic process (*140, 141*), and in myocardial reperfusion injuries, which are believed to be caused by Mb after a period of ischemia (*53, 54*). Hence, a detailed study was performed to identify reactive intermediates generated on cyt c and Mb upon their reaction with H_2O_2. The Soret band of the three cyts c was used to calculate the rate of heme degradation in the presence of excess H_2O_2 and to investigate the pH dependence of cyt c heme degradation by H_2O_2. ST/LC/MS was performed to locate $X^{\bullet}$ species formed during the cyt c/H_2O_2 reaction (Chapter 5).

Noncovalent DBNBS-cyt c mass adducts were observed while performing the experiments in Chapter 5 and we theorized that they were due to ion pair formation between the negatively charged sulfonate group on DBNBS and positively charged surface residues on cyt c, revealing a pitfall inherent in using ST/LC/MS. Thus,

substitution of cyt c with Mb and α-lactalbumin in the cyt c/H_2O_2/DBNBS reaction was performed to establish whether or not DBNBS-protein adduct formation exhibits specificity. To elucidate the mechanism by which the $(DBNBS)_n$-cyt c mass adducts are formed, acid-unfolded horse cyt c was titrated with DBNBS at pH 2.0, and changes in the Soret and MS spectra were monitored. Optical difference spectra of the reaction products obtained for horse cyt c in the absence and presence of H_2O_2 were recorded to probe the nature of the DBNBS adducts detected by MS (Chapter 6).

In Chapter 6, we observed increased trapping efficiency of DBNBS vs MNP in the Mb/H_2O_2 reaction. Hence, we believed that DBNBS was a more efficient trap and would be an ideal trap to use to characterize the Mb/H_2O_2 reaction products. Furthermore, ST/LC/MS was used to establish whether the radical sites identified in the Mb/H_2O_2/DBNBS reaction were independent of the spin trap used. The yield of $(DBNBS)_n$-Mb mass adducts was carried out as a function of H_2O_2 concentration and pH. Optical difference spectra of the reaction products obtained for Mb in the absence and presence of H_2O_2 were recorded to characterize the $(DBNBS)_n$-Mb mass adducts. Finally, the electron-transfer pathways were examined using the Hamiltonian for Response Properties of Large Molecules (HARLEM) to identify oxidizable residues that have large electronic couplings with the heme redox center in Mb (Chapter 7).

1.6 Contributions of Colleagues

Chapters 2, 3, 4 and 6 are published manuscripts or in press, while Chapters 5 and 7 are currently being prepared for publication. All abbreviation, citation, figure and

table numbering systems in the published works were changed to the format of this thesis.

Chapter 2 was published in the *Journal of Biological Inorganic Chemistry* [Filosa, A. and English, A. M. (2000) *J. Biol. Inorg. Chem. 5*, 448] and is reproduced with the permission of the journal. I carried out all the work reported in this publication and prepared the manuscript. A.M. English provided intellectual support, supervision and edited the manuscript.

Chapter 3 was published in the *Journal of Biological Inorganic Chemistry* [Filosa, A., Ismail, A. A. and English, A. M. (1999) *J. Biol. Inorg. Chem. 4*, 717] and is reproduced with the permission of the journal. I carried out all the work reported in this publication and prepared the manuscript. Both A. A. Ismail and A. M. English provided intellectual contributions, supervision and edited the manuscript. As well, A. A. Ismail provided instruction on the use of FTIR instrumentation and on data analysis.

Chapter 4 is "Reproduced with permission from [*Biochemistry*], in press. This paper is based on the results reported in Chapter 3. The initial idea to plot the data from Chapter 3 using 2D IR correlation analysis arose from discussions with A. A. Ismail. Y. Wang wrote the 2D analysis programs and assisted in interpretation of the 2D IR data. A. A. Ismail and A. M. English provided intellectual contributions and supervision, and all three co-authors edited the manuscript, which I prepared.

Chapter 6 is in press in the *Journal of Biological Chemistry* [Filosa, A. and English, A. M. (2001) *J. Biol. Chem., Papers in Press*]. I carried out all the work reported in this publication and prepared the manuscript. A. M. English provided intellectual contribution, supervision and edited the manuscript.

2.0 Probing Local Thermal Stabilities of Bovine, Horse and Tuna Ferricytochromes c at pH 7

2.1 Abstract

Correlation between the flexibility of the Met80 loop (residues 75-86) and the local stabilities of native cyts c from horse, cow, and tuna was examined. By monitoring the heme bands vs temperature, absorption changes associated with altered ligation in the alkaline isomers was observed. In addition, the intensity of the 695-nm absorption band, which is associated with the heme-crevice stability, decreased with increasing temperature and exhibited biphasic temperature dependence, with transition temperatures (T_c) at 35°C in tuna cyt c, 55°C in horse and 58°C in cow cyts c. Since, the heme-crevice plays a key role in the thermal stabilities of cyts c, their susceptibility to proteolytic attack was examined as a function of temperature. Proteolytic digestion, which requires local conformational instability, revealed that the local stabilities of the cyts follow the order: cow > horse >> tuna, and increased digestion occurred at temperatures close to the 695-nm T_c for each protein. This is consistent with the actual substitution of the Met80 ligand above the 695-nm T_c, which is reflected in the thermodynamic parameters for the two phases. Also, tuna cyt c, unlike horse and bovine cyts c, exhibits different 695-nm (35°C) and Soret (~ 46°C) T_cs, but its local stability is controlled by the transition detected at 695 nm. The combined spectroscopic and proteolysis results clearly indicate that the flexibility of the Met80 loop determines the local stability of cyts c.

2.2 Introduction

In eukaryotic cyt c, the fifth and sixth axial positions of the ferric iron are occupied by a relatively weak bond between the metal and the sulfur of Met80 and a stronger bond between the iron and N3 from His18 (*1-3, 5*). Further weakening of the Fe^{III}-S(Met80) bond by raising the pH at room temperature or by increasing the temperature at neutral pH is associated with the well documented alkaline isomerization (*1*). The alkaline isomers are reported to possess six-coordinate low-spin heme iron that retains His18 ligation but substitute Met80 ligation by one or more unknown strong-field ligand(s) (*1*). NMR experiments have established the interdependence between the pH- and temperature-induced local conformational changes occurring during the conversion of native horse cyt c to its alkaline isomers (*13*).

A large body of evidence shows that the weak absorption band at 695 nm, which purportedly results from a porphyrin $\rightarrow Fe^{III}$ transition (*83*), is associated with the integrity of the Fe^{III}-S(Met80) bond (*1, 4, 7*). Conversion of horse cyt c to its alkaline isomers was first detected by the loss of 695-nm absorption with increasing pH (*6*). The 695-nm band of horse cyt c has been reported to exhibit biphasic temperature dependence with a transition at ~ 50°C (*4, 8, 84*). Changes in orientation of the Met80 side chain with respect to the heme are associated with the slow loss of 695-nm intensity below the transition temperature, while the actual substitution of Met80 with a strong-field ligand occurs above the transition temperature (*7*).

Despite the similar overall structural elements and global stabilities found between various cyts c, differences in local stabilities do exist (*9*). Electrochemical (*85*) data suggest

that tuna cyt c possesses a less stable heme crevice compared to horse and cow cyts c. Also, a high susceptibility to proteolytic digestion at 37°C (*9*) reveals the considerably lower local stability of tuna cyt c. Since proteases cleave only at locally unfolded regions of a polypeptide, protease susceptibility implies local conformational instability (*86, 87*). Metalloderivatives of horse cyt c were prepared by Hu and coworkers (*10*) to examine the effects of metal substitution on the stability of the protein. It was observed that the local stability, as determined by tryptic digestion, decreased with decreasing strength of the metal-S(Met80) bond. Bai and coworkers (*88*) examined the H/D exchange behavior of native horse cyt c by NMR, and concluded that the fastest H/D exchange rates occur in the segment 70-85, which encompasses the region we called the Met80 loop (residues 75-86) (*10*). Thus, in horse cyt c and its metalloderivatives, the conformational flexibility of the Met80 loop, which is dependent on the strength of Met80 ligation, controls the susceptibility of the protein to proteolytic attack by trypsin.

To determine whether the Met80 loop also controls the local stability of other cyts c, the susceptibility to tryptic digestion of horse, cow and tuna cyts c is compared in the present study to changes in their 695-nm absorption bands vs temperature. While the 695-nm absorption as a function of temperature has been studied extensively for horse cyt c, this is the first investigation of the temperature dependence of this absorption in tuna and cow cyts c (*4, 8, 83*). The results reveal that cleavage or weakening of the Fe^{III}-S(Met80) bond, with the resultant opening of the heme crevice, controls the local stability of all three cyts c. Considering the suggested importance of closed-open heme-crevice conformational equilibria to the biological function of cyt c (*20*), it is notable that the Met80 loop represents the site of greatest local instability in the homologous cyts c examined here. The heme

absorption bands were also investigated to probe changes in Fe^{III} ligation vs temperature.

2.3 Experimental

Cyts c from horse heart (Type VI), cow heart and tuna heart (Type XI) were obtained from Sigma and purified by cation-exchange fast-protein liquid chromatography (FPLC, Pharmacia) as described previously (*89*). All buffers were prepared using nanopure water (Barnstead, 18 MΩ-cm).

The temperature dependence of the 695-nm and heme absorption visible bands was recorded on a Beckman DU 650 spectrophotometer equipped with a temperature-controlled cell. Lyophilized cyt c was dissolved in 50 mM sodium phosphate/0.2 M KCl buffer (pH 7.0) at 26°C and the concentrations determined spectrophotometrically assuming $\varepsilon_{410} = 106.1$ mM^{-1} cm^{-1} (*90*). The temperature of the cuvette was monitored between 2 and 80°C using an Omega HH-25KC type k thermocouple and the spectrum of cyt c was scanned between 250 to 800 nm at a scan rate of 1200 nm/min after the solution had reached thermal equilibrium (~ 10 min). Since the 695-nm absorption is a weak shoulder on the α visible band of cyt c, its intensity is corrected for changes in background absorption by extrapolation of the lower wavelength absorbance and the result expressed as ΔA, as outlined previously (*7*).

The limited proteolysis studies were carried out as described in detail previously (*9, 10*) and the procedure is outlined here. Two mg/ml lyophilized cyt c was dissolved in 50 mM sodium phosphate/0.2 M KCl buffer (pH 7.0). TPCK-treated cow trypsin was obtained from Pierce, purified according to the procedure provided, and its concentration determined

spectrophotometrically, assuming $\varepsilon_{280} = 0.7\ mM^{-1}cm^{-1}$. The cyt c and trypsin solutions were mixed to give a 50/1 (w/w) ratio and incubated at the appropriate temperature for 0-4 h. Digestion was terminated by lowering the pH to 2 with 5 M HCl (10 μl) and the tryptic digests were analyzed by HPLC (HP1090 series II). Aliquots (20 μl) of the digestion mixture were injected onto a reversed-phase C_{18} column (HP-ODS Hypersil, 5 μm, 100 x 2.1 mm) equilibrated with 20% acetonitrile (HPLC grade, BDH) and 0.1% TFA (HPLC grade, Aldrich), and eluted with a 20-80%-acetonitrile gradient in 0.1% TFA over 15 min at a flow rate of 0.5 ml/min under a pressure of 160 bar. The eluted samples were detected at 210 nm (peptide backbone) and 410 nm (heme), and absorbance vs elution time was recorded using an HP 79994A HPLC Chemstation (Agilent Technologies). The column was re-equilibrated with starting solvent for 5 min after each 15-min run.

2.4 Results and Discussion

2.4.1 Temperature Dependence of the Soret Maxima

Figure 2.1 reveals that the Soret maxima of the three cyts c blue shift at high temperature, indicating alterations in the heme-crevice pocket. In horse and cow cyts c, a blue shift from 408 to 406-407 nm occurs between 55 and 60°C, which is associated with the thermally-induced conversion of the mammalian cyts c to their alkaline isomers. Alkaline isomerization of horse cyt c reportedly involves formation of 6-coordinate heme iron, which retains His18 ligation but Met80 is replaced by unknown strong-field ligands (*1*). NMR (*17*) and EPR (*91*) studies on horse cyt c indicate that the alkaline form is a mixture of two lysine-ligated conformers, and Lys72 and Lys79 have been implicated as possible sixth ligands (*19*).

Above 65°C, the Soret maxima blue shift to 405 nm, and this is correlated with unfolding of the polypeptide backbone of horse and cow cyts c (*11, 92*). The Soret absorption of tuna cyt c (Figure 2.1) exhibits a blue shift from 407 to 406 nm above ~ 46°C, which likely corresponds to the second conformational transition detected in the amide II region of FTIR (*93*). Above 60°C, a Soret blue shift from 406 to 403 nm is observed (Figure 2.1), which is correlated with unfolding of the polypeptide backbone in tuna c. The ligation states of the heme corresponding to the observed Soret shifts are discussed below.

2.4.2 Temperature Dependence of the 695-nm Absorbance

The low- and high-temperature absorbance changes at 695 nm in horse cyt c have been attributed to two separate, two-state processes (*5, 8, 94*), with the spectroscopic changes representing equilibria between denatured (open-crevice) and native (closed-crevice) forms of the protein. The equilibrium constants between the denatured and native forms of the protein are estimated from the ratio $[(\Delta A_{cc} - \Delta A_T)/(\Delta A_T - \Delta A_{oc})]$ where ΔA_{cc} is the absorbance at 695 nm of the closed-crevice conformation, ΔA_{oc} that of the open-crevice conformation, and ΔA_T the observed 695-nm absorbance at temperature T (*4, 5, 8, 95*). Similar to previous reports (*4, 8*), we find that the thermal denaturation of horse cyt c as probed by the 695-nm absorbance occurs via a two-step process with T_c at 55°C in the van't Hoff plot (Figure 2.2b), indicating that weakening of the Fe^{III}-S(Met80) bond proceeds via different mechanisms at low and high temperature. Biphasic van't Hoff plots were also obtained for cow and tuna cyts c, with T_c's at 58 and 35°C, respectively (Figure 2.2a, c).

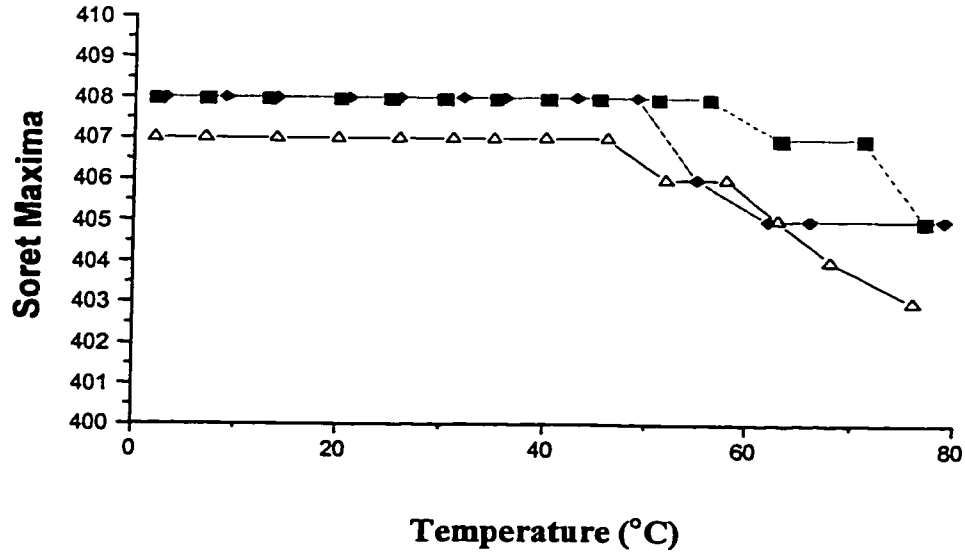

Figure 2.1. Soret absorption maxima vs temperature of 19-22 μM (■) cow, (◆) horse, and (Δ) tuna ferricytochromes c. All solutions contained 50 mM sodium phosphate/0.2 M KCl buffer, pH 7.0 and were allowed to equilibrate for 10 min at each temperature. Spectra were recorded at a scan rate of 1200 nm/min.

Using the van't Hoff equation ($\Delta G° = -RT \ln K_{eq}$) and analyzing each process as two separate two-state equilibria leads to the thermodynamic parameters listed in Table 2.1. These parameters reflect changes mainly occurring around the heme crevice since our recent FTIR results (*93*) reveal that no major conformational changes are associated with the alkaline isomerization. The thermodynamic parameters obtained for the two processes for horse cyt c differ from those reported previously (*8, 95, 96*). This can be attributed to the known perturbing effects of KCl on cyt c conformation (*93, 97*), which was added to the samples in the present study to mimic the limited-proteolysis studies performed in 0.2 M KCl (*9, 89*). Nonetheless, both processes in the thermally-induced conversion of the cyts c to their alkaline isomers are accompanied by unfavorable enthalpy changes and favorable entropy changes. The significantly higher $\Delta H°$ values for the high temperature phase are consistent with actual cleavage of the Fe^{III}-S(Met80) bond above the T_c. The $\Delta H°$ values for the high temperature phase also reflect the variation in 695-nm molar absorptivity since at 20°C the $\Delta\varepsilon_{695}$ values ($\mu M^{-1}cm^{-1}$) increase in the order tuna (161) < horse (202) < cow (207), which suggests a correlation between the heme-crevice stability and 695-nm absorptivity (*5, 9, 89*) . Also, the variation in the $\Delta G°$ values is consistent with the lower kinetic barrier to heme-crevice isomerization reported for tuna cyt c in pH jump experiments (*98*).

2.4.3 Analysis of the Local Stability of Cytochromes c by Limited Tryptic Proteolysis

Proteolytic digestion is used to probe the local stability of proteins since only locally unfolded regions of a protein are cleaved by proteases (*86, 87*). A decrease in heme-crevice

stability, associated with cleavage or weakening of Met80 axial ligation, resulted in increased flexibility of the Met80 loop in horse cyt c and its metalloderivatives, which in turn increased the rate of proteolytic digestion (*9, 10*). Thus, correlation of thermal stability of the heme crevice, as reflected in the $\Delta G°$ values in Table 2.1, with susceptibility for proteolytic attack (*9*) predicts that tuna cyt c would be more susceptible to proteolytic digestion than horse or cow cyt c at any temperature. Also, from the $\Delta G°$ values for the low-temperature phase (Table 2.1), tuna cyt c is expected to possess greater local stability below 37°C, the temperature at which tryptic digestion is normally carried out.

The time evolution of proteolytic digestion of the cyts c was determined by HPLC analysis of their tryptic digests (*10*). Relative peak areas of the HPLC bands containing undigested protein vs time were measured, with the areas under the bands at 0 h taken as 100%. The time course of cyt c digestion at 37°C is plotted in Figure 2.3a, and the trend in local stability over 4 h (cow > horse >> tuna (*9*) follows the trend expected from the 695-nm T_c values (Figure 2.2a-c). It is of note that the accelerated digestion of tuna cyt c compared to horse and cow cyts c cannot be explained simply by the number of trypsin-susceptible sites (Lys and Arg), since cow and horse cyts c both have 21 sites and tuna cyt c has only 17 sites. Hence, the variation in local stability is ascribed to differences in heme-crevice stability of the proteins.

The time course of cow, tuna and horse cyt c digestion at 25°C is plotted in Figure 2.3b. As expected, tuna cyt c is much less susceptible to proteolytic attack at 25°C, and hence possesses greater local stability below its 695-nm T_c at 35°C. This is consistent with substitution of the Fe^{III}-(S)Met80 bond and conversion to the alkaline isomer above 35°C.

The open-crevice structure of the alkaline isomers renders it more susceptible to proteolytic attack as was observed for the CN^- adduct of horse cyt c (*10*), where CN^- displaces the Met80 ligand.

The time course of tryptic digestion was also monitored at 50 and 56°C (data not shown), since the 695-nm T_c for cow and horse cyts c were found to be 58 and 55°C, respectively (Figure 2.2a, b). Increased digestion of the proteins was observed, consistent with the more open heme crevice predicted at elevated temperatures from the thermodynamic data (Table 2.1). Figure 2.3c, which compares the percent undigested of the three cyts c after 3 h at different temperatures, confirms that increased digestion of the horse and cow proteins does occur as the digestion temperature approaches the 695-nm T_c. Thus, the flexibility of the Met80 loop clearly plays an important role in determining the local stability of these homologous cyts c.

2.4.4 Properties of the Low and High Temperature Conformers

Cow and horse cyts c possess low-spin hemes over the temperature range investigated since no 630-nm absorption, which is diagnostic of high-spin ferriheme proteins (*1, 99*), is present in Figure 2.4a or 2.4b. The broadening and blue-shifting of α and β bands, as well as blue-shifting and intensification of the Soret as the temperature is increased (Figure 2.4a, b) is indicative of increased solvent exposure of the heme crevice (*100*). Absorption at 630 nm becomes apparent around 60°C in the spectra of tuna cyt c (Figure 2.4c), indicating the formation of some 6-coordinate, high-spin heme in this cyt c (*19, 92*). Interestingly, Hu (*89*) reported that tuna and horse cyts c exhibit high- and low-spin heme, respectively, in high

urea and guanidine-HCl concentrations.

The blue-shift in the Soret absorption maxima of horse and cow cyts c (Figure 2.1) is observed close to their respective 695-nm T_cs. This supports the mechanism proposed for the alkaline isomerization of horse cyt c where the slow loss of 695-nm absorbance below the 695-nm T_c is due to changes in orientation of the Met80 side chain with respect to the heme, followed by the actual substitution of the Met80 ligand by another strong-field ligand above the 695-nm T_c (*4, 14*). Nonetheless, it is evident that the Soret T_c at ~ 46°C (Figure 2.1) does not correspond to the 695-nm T_c at 35°C (Figure 2.2c) for tuna cyt c, indicating that this cyt undergoes two separate heme-linked transitions. However, the Soret T_c (~ 46°C) is close to the second amide-II T_c (50°C) detected by FTIR (*93*), indicating that replacement of the Met80 ligand in tuna cyt c [presumably by Lys (*96*)] is spectroscopically silent in the Soret region.

The T_c values associated with alkaline isomerization as determined by a variety of physical techniques are summarized in Table 2.2. From these data, it is evident that tuna cyt c converts to its alkaline form at a significantly lower temperature than cow and horse cyt c. Recently, we proposed that the T_cs at 35 (tuna), 54 (horse), and 57°C (cow) observed in the FTIR amide II-monitored thermal titrations (*93*) correspond to tertiary-structure transitions that accompany alkaline isomerziation, and this hypothesis is supported by the fact that identical T_c values are obtained from the van't Hoff plots (Figure 2.2, Table 2.2) and the FTIR amide II plots (*92*). The extra amide II transition with a T_c of 50°C, and the Soret T_c at ~ 46°C reveal that following its alkaline isomerization, tuna cyt c undergoes a second transition (*93*) that increases the solvent exposure of its heme.

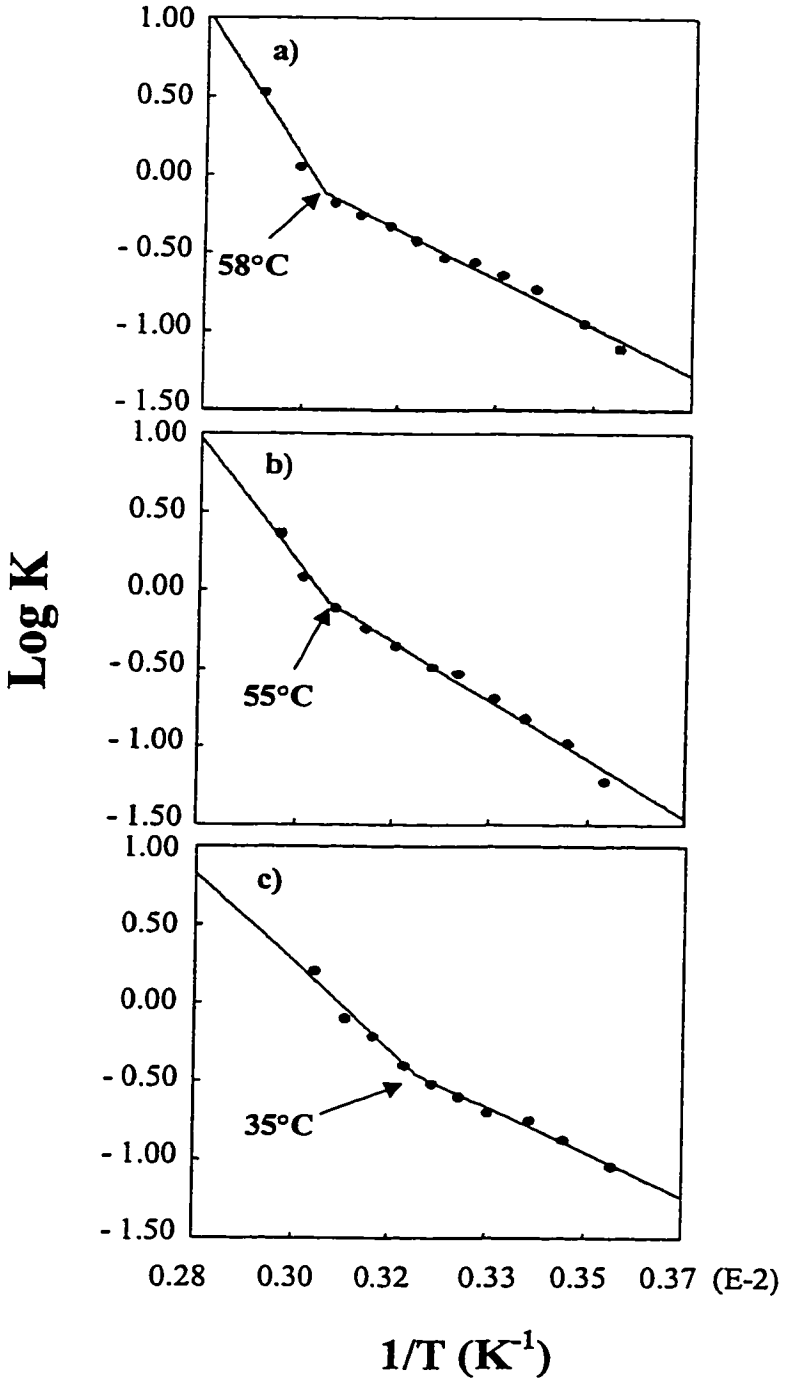

Figure 2.2. van't Hoff plots for (a) cow, (b) horse, and (c) tuna ferricytochromes c. The experimental conditions are given in the legend to Fig. 2.1.

Table 2.1. Thermodynamic parameters[a] for the heme-crevice transitions of cow, horse and tuna ferricytochromes c as determined from the temperature dependence of their 695-nm absorption band

Cytochrome c	ΔH° (kJ mol^{-1})	ΔS° (J $mol^{-1}K^{-1}$)	ΔG° (kJ mol^{-1})		
			25°C	37°C	55°C
Cow (low)[b]	32.7	96.5	3.93	2.97	1.04
Cow (high)[c]	102	304	10.8	7.80	1.70
Horse (low)[b]	40.0	120	4.22	3.02	0.630
	82.8[d]	280[d]	9.2[d]		
Horse (high)[c]	84.8	256	8.46	5.90	0.770
	189[d]	557[d]	17.9[d]		
Tuna (low)[b]	36.6	113	2.98	1.84	-0.400
Tuna (high)[c]	71.7	226	4.34	2.10	-2.43

[a]Standard deviations of ~ 10% were calculated for the thermodynamic parameters

[b,c]Low and high refer to the low- and high-temperature processes in Figure 2.2, which were recorded in 50 mM sodium phosphate/0.2 M KCl, pH 7.0.

[c]Data from (*8*) recorded in 50 mM sodium phosphate, pH 7.0.

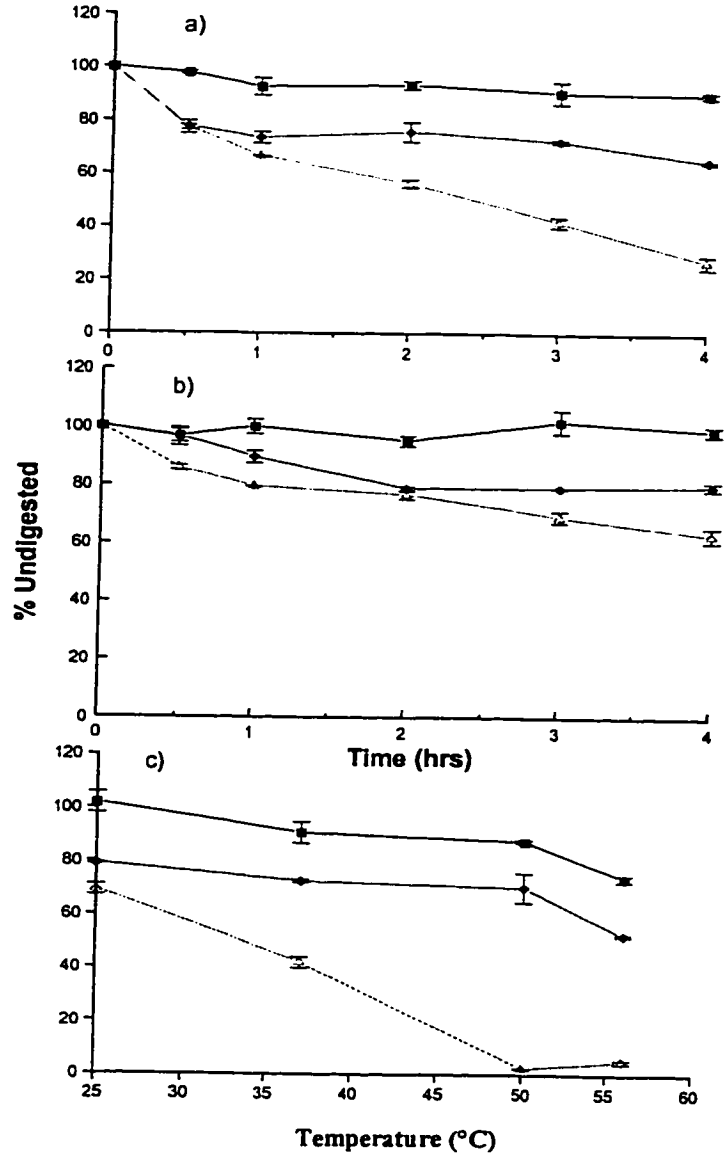

Figure 2.3. Time course of tryptic digestion at (a) 37°C and (b) 25°C of (■) cow, (◆) horse and (Δ) tuna ferricytochromes c, and (c) the extent of tryptic digestion over 3 h of each cytochrome at different temperatures in 50 mM sodium phosphate/0.2 M KCl buffer, pH 7.0. The cytochrome-to-trypsin ratio used was 50:1 (w/w) and the samples were incubated at the specified temperatures for 4 h. Digestion was terminated by adding 10 μl of 5 N HCl.

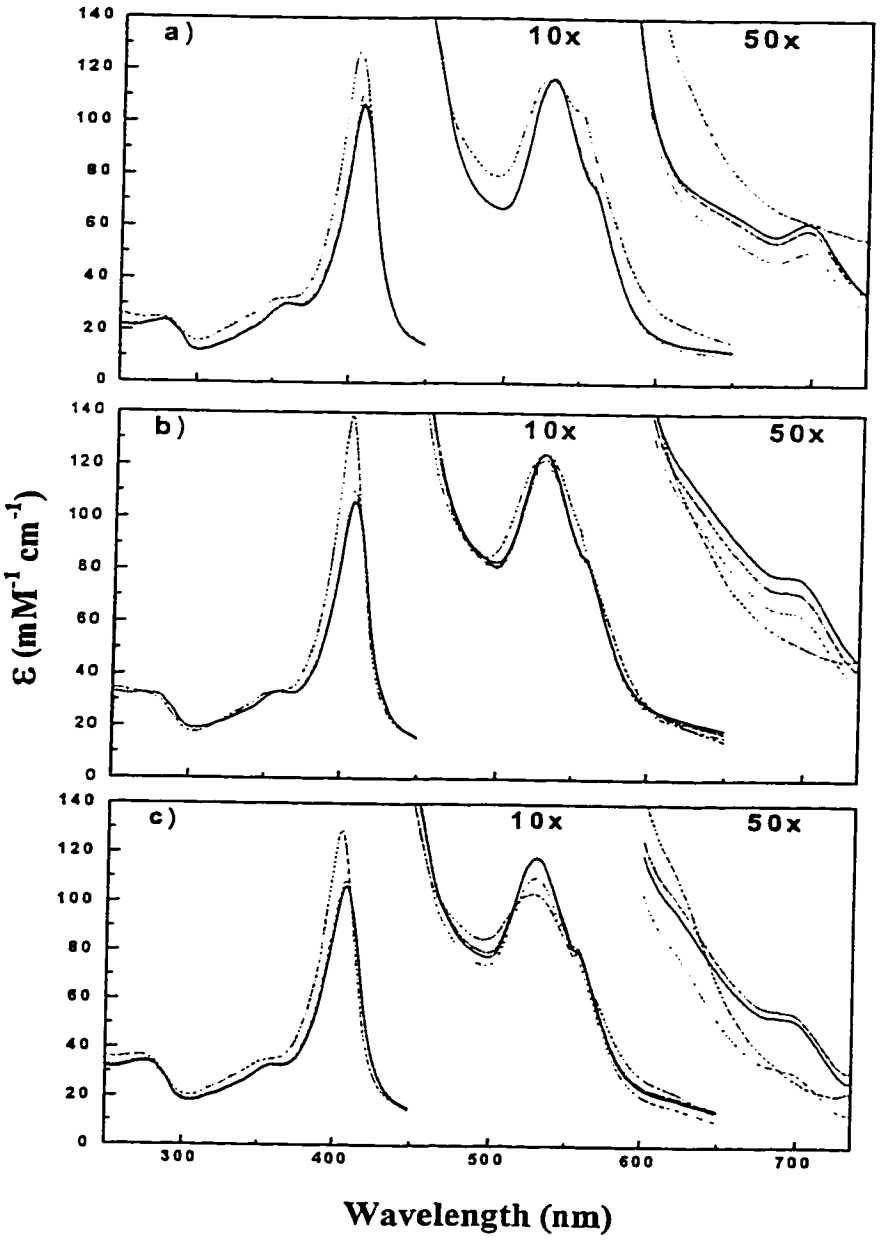

Figure 2.4. Electronic absorption spectra of 19-22 μM (a) cow and (b) horse ferricytochromes c at 25°C (——), 50°C (– – –), 65°C (·····) and 78°C (– ·· –), and (c) tuna ferricytochrome c at 25°C (——), 45°C (– – –), 60°C (·····) and 78°C (– ·· –). The experimental conditions are given in the legend to Figure 2.1.

Table 2.2. Transition temperatures for the alkaline isomerization of ferricytochromes c

Technique	Conditions	T_c (°C)	Ref
	Horse cytochrome c		
695-nm absorption	50 mM NaPi/0.2 M KCl (pH 7.0)	55	this work
Soret absorption	50 mM NaPi/0.2 M KCl (pH 7.0)	48	this work
695-nm absorption	10 mM cacodylate/10 mM NaCl (pH 7.0)	49	(*107*)
FTIR amide II	50 mM NaPi/0.2 M KCl (pH 7.0)	54	(*93*)
magnetic susceptibility	10 mM phosphate (pH 5.3)	57	(*7*)
electrochemistry	0.2 M Tris/cacodylic acid (pH 7.0)	53	(*85*)
^{1}H NMR	0.1 M KPi (pH 7.5)	59	(*13*)
	Cow cytochrome c		
695-nm absorption	50 mM NaPi/0.2 M KCl (pH 7.0)	58	this work
Soret absorption	50 mM NaPi/0.2 M KCl (pH 7.0)	56	this work
FTIR amide II	50 mM NaPi/0.2 M KCl (pH 7.0)	57	(*93*)
electrochemistry	0.1 M NaCl (pH 7.5)	50	(*108*)
	Tuna cytochrome c		
695-nm absorption	50 mM NaPi/0.2 M KCl (pH 7.0)	35	this work
Soret absorption	50 mM NaPi/0.2 M KCl (pH 7.0)	46[a]	this work
FTIR amide II	50 mM NaPi/0.2 M KCl (pH 7.0)	35	(*93*)
		50[a]	(*93*)
electrochemistry	0.2 M Tris/cacodylic acid (pH 7.0)	32	(*85*)

[a]The 695-nm, Soret and amide II T_cs overlap for horse and cow cyts c (prior to loss of secondary structure). There are clearly two separate transitions for tuna cyt c as reflected in different 695-nm and Soret T_c values, as well as the observation of two amide II transitions with T_cs corresponding to 695-nm T_c and the Soret T_c, respectively (see text).

2.4.5 Structural Basis for Differences in Thermodynamic and Local Stabilities of the Cytochromes c

Horse and cow cyts c contain highly hydrophobic residues in the segment Ala43 to Phe46, while two (Pro44, Phe46) of the four residues in this 43-46 segment are replaced by more hydrophilic residues (Glu44, Tyr46) in tuna cyt c. Elimination of hydrophobic residues in contact with the heme is expected to result in decreased stability of the heme crevice (*102*). The thermal stability of the cyts c in the region that include residues 58-62 (TWGEE in bovine; TWKEE in horse and VWNND in tuna cyts c) was followed by monitoring the temperature dependence of the chemical shifts of the δCH_3 resonance of Ile57 (*103, 104*). The NMR results suggest that tuna cyt c is more sensitive to thermal effects in this region, which may weaken the Fe^{III}-S(Met80) bond and reduce the thermal stability of the tuna cyt c heme crevice. NMR studies (*104, 105*) also show that horse and tuna cyts c possess small differences in their N- and C-terminal helices that affect the highly conserved helix-helix interaction observed in cyt c (*106*). It was reported that weakening of this interaction in yeast cyt c renders the polypeptide more susceptible to tryptic attack (*106*); hence reduced interaction at the helix-helix interface may contribute to the weakened Fe^{III}-S(Met80) bond in tuna cyt c as reflected in its relatively low 695-nm molar absorptivity (Figure 2.4).

Despite the high sequence identity (97%) between cow and horse cyts c, the cow protein possesses higher 695-nm absorbance ($\Delta\varepsilon_{695}$ = 247 for bovine vs 202 $\mu M^{-1}cm^{-1}$ for horse cyt c). This suggests that the heme-crevice stability is greater in cow cyt c, making it less susceptible to proteolytic attack compared to horse cyt c. The latter can be predicted

from the ΔG° values in Table 2.1, assuming that heme-crevice stability governs local stability. Endo and coworkers (*9*) observed by CD that cow cyt c thermally denatures at a higher temperature than horse cyt c, and suggested that protease susceptibility correlates fairly well with global thermal stability. However, the 20°C lower 695-nm T_c of tuna cyt c compared to cow and horse cyts c would not be predicted from the small variation in their global thermal stabilities as observed by CD (*9*) and FTIR (*93*). Thus, we believe that the heme-crevice stability of cyt c from different species varies with the physiological temperature of the species. Such a correlation has been suggested before for tuna and mammals (*85*).

2.5 Conclusions

The work outlined here shows that the local stability as monitored by tryptic digestion of cyt c reflects that of the Met80-loop region. In view of the evidence (*20*) that cyt c undergoes conformational changes related to its alkaline isomerization upon binding to some of its biological partners, it is important to establish whether the locally unfolded forms detected *in vitro* are physiologically relevant. We found that horse and cow cyts c, which exhibit 695-nm T_cs at 50 and 58°C, respectively, are resistant to proteolytic digestion at 37°C, yet tuna cyt c, which has its 695-nm T_c at 35°C, is not. Hence, amino acid substitutions that alter the flexibility about the Met80 loop (as reflected in the 695-nm T_c) also affect the *local* stability of cyt c (as reflected in the ease of proteolysis). Thus, for the three cyts c examined here, there seems to be a correlation between functional temperature *in vivo* (tuna is a cold-body species unlike the warm-body mammals) and heme-crevice

conformational stability observed *in vitro*.

3.0 FTIR-monitored Thermal Titration Reveals Different Mechanisms for the Alkaline Isomerization of Tuna Compared to Horse and Bovine Cytochromes c

3.1 Abstract

FTIR spectroscopy is used to compare the thermally induced conformational changes in horse, cow and tuna cyts c in 50 mM phosphate/0.2 M KCl. Thermal titration in D_2O at pD 7.0 of the amide II intensity of the *buried* peptide NH protons reveals tertiary structural transitions at 54°C in horse and at 57°C in cow cyts c. These transitions, which occur well before loss of secondary structure, are associated with the alkaline isomerization involving Met80 heme-ligand exchange. In tuna cyt c, the amide-II-monitored alkaline isomerization occurs at 35°C, followed by a second amide II transition at 50°C revealing a hitherto unreported conformational change in this cyt c. Amide II transitions at 50°C (tuna) and 54°C (horse) are also observed during the thermal titration of the CN^--ligated cyts c (where CN^- displaces the Met80 ligand), but a well-defined 35°C amide II transition is absent from the titration curve of the CN^--adduct of tuna cyt c. The different mechanisms suggested by the FTIR data for the alkaline isomerization of tuna and the mammalian cyts c are discussed. After the alkaline isomerization, loss of secondary structure and protein aggregation occur within a 10°C range with T_ms at 74°C (cow), 70°C (horse) and 65°C (tuna), as monitored by changes in the amide I' bands. The FTIR spectra were also used to compare the secondary structures of the cyts c at 25°C. Curve-fitting of the amide I (H_2O) and amide I' (D_2O) bands

reveals essentially identical secondary structure in horse and bovine cyts c, whereas splitting of the α-helical absorption of tuna cyt c indicates the presence of less stable helical structures. CN^--adduct formation results in no FTIR-detectable changes in the secondary structures of either tuna or horse cyt c, indicating that Met80 ligation does not influence the secondary structural elements in these cyts c. The data provided here demonstrate for the first time that the *selective* thermal titration of the amide II intensity of *buried* peptide NH protons in D_2O is a powerful tool in protein conformational analysis.

3.2 Introduction

Cyt c is a small (MW ~ 12 400 Da), water-soluble protein that exists in the cytosol between the inner and outer mitochondrial membranes. Its function is to mediate the transfer of electrons from cytochrome c reductase to cytochrome c oxidase, the terminal enzyme in the electron transport chain of eukaryotes (*1-3*). The protein consists of a single polypeptide chain organized into five α-helical segments that account for ~ 45% of its amino acid residues. The six-coordinate, low-spin iron present in the heme is coordinated to the four nitrogens of the porphyrin ring and the fifth and sixth axial positions are occupied by a relatively weak bond between the iron and the sulfur of Met80, and a stronger bond between the iron and N_3 from His18 (*4, 12*).

Crystal structures for horse (*2*) and tuna cyts c (*109*) reveal that both cyts c possess very similar secondary and tertiary structures. Cow cyt c is assumed to be essentially identical in structure to horse cyt c since the two proteins share high sequence identity (> 97%). Despite remarkably similar main-chain structures (*2, 109*), cyts c from

different species exhibit different local stabilities as probed by tryptic digestion (*9-11*) and 695-nm absorption (*4, 8, 11,12*). The latter measures the integrity of the Fe^{III}-S(Met80) bond since disruption or weakening of this bond results in quenching of the 695-nm absorption and opening of the heme crevice (*5*).

The well-documented alkaline isomerization of cyt c (*1*) is associated with the loss of 695-mm absorption that occurs on raising the pH to alkaline values at room temperature or raising the temperature at neutral pH (*13*). The thermally induced conversion of cyt c to its alkaline isomer as monitored at 695-nm is biphasic (*4, 11*), with phase-transition temperatures at 35°C in tuna cyt c and above 50°C in horse and cow cyts c (*11*). Consistent with its lower phase-transition temperature, tuna cyt c exhibits increased susceptibility to tryptic digestion compared to horse and cow cyts c at 37°C (*11*). Related studies on the protease susceptibility of metalloderivatives of horse cyt c indicated that the strength of Met80 ligation is the main determinant of *local* conformational stability since weakening or removal of this bond greatly increases the local flexibility of the protein (*10*).

The lower thermal stability of the heme crevice of tuna cyt c relative to the horse and cow cyts c is somewhat curious given that the three proteins possess similar global thermal stabilities as monitored by CD (*9*) and calorimetry (*85*). Hence, in the present study, FTIR spectroscopy is used to compare the conformational changes occurring during the thermal titration of tuna cyt c with those in the horse and cow cyts c. FTIR spectroscopy is a highly sensitive probe of protein conformation under a variety of experimental conditions (*63, 64*), as has been clearly demonstrated in its ability to distinguish structural differences between the oxidized and reduced forms of cyt c (*65*).

Information at the level of secondary structure is obtained from the amide I bands (which downshift by ~ 5 cm^{-1} in D_2O and are labelled amide I' bands). The amide I region is composed primarily of peptide carbonyl stretching vibrations, which are sensitive to backbone conformation and the degree of H-bonding of the carbonyls (*63, 110*). Information on tertiary folding states is obtained by monitoring H/D exchange of the peptide protons (*63, 64*) since the amide II bands, composed primarily of NH bending of peptide groups, decrease in intensity following H/D exchange (*21, 67, 68*). Enhanced peptide H/D exchange is generally observed in proteins at temperatures well below those required for secondary structure unfolding, allowing the identification of tertiary folding intermediates with increased solvent accessibility (*111*).

FTIR spectra of the CN^--adducts of horse and tuna cyts c were additionally investigated to dissect any conformational changes associated with the alkaline isomerization from other thermally-induced, non-heme-linked, conformational changes. The CN^- ion, which serves as a high affinity ligand for the ferric state of many hemoproteins (*112, 113*), binds to cyt c by displacing the axial Met80 ligand (*114-116*), resulting in loss of 695-nm absorption (*115*). As demonstrated in the present study, thermal titration of the FTIR amide II bands provides new insight into the alkaline isomerization of the cyts c by identifying a number of conformational intermediates that occur above room temperature prior to loss of secondary structure. The combined results on the native and ligated forms shed light on the role of axial ligation in controlling the conformational states of cyt c. The FTIR-detectable folding intermediates described here, with essentially intact secondary structure but altered tertiary structure, may represent biologically relevant conformations of the proteins since the heme crevice of cyt c

reportedly undergoes open-closed transitions on interaction with some of its biological partners (*20*). This latter observation has renewed interest in the alkaline isomerization of cyt c (*16, 18*).

Finally, the difference in the 25°C FTIR spectra of tuna cyt c from those of the mammalian cyts c in the amide I and I' regions motivated the assignment of the peaks in these regions. With the aid of curve fitting, the observed amide I and I' intensities can be satisfactorily assigned to the secondary structural elements observed in the X-ray and NMR structures of the unligated proteins. Surprisingly, the curve fitting reveals that displacement of the Met80 ligand by CN^- causes almost no FTIR-detectable changes in *secondary* structure at 25°C.

3.3 Experimental Procedures

3.3.1 Materials

Cyts c from horse heart (Type VI), cow heart and tuna heart (Type XI) were obtained from Sigma and purified by cation-exchange FPLC (Pharmacia) as described (*10*). Potassium cyanide was purchased from BDH Chemicals. Nanopure water (specific resistance 18 MΩ-cm) obtained from a Barnstead nanopure system was used for all H_2O work.

Phosphate buffers (pH 7.0 or pD 7.0) were prepared by dissolving 50 mM sodium phosphate salts (Fisher Scientific) in nanopure H_2O or 99.9% D_2O (Aldrich). Spectra were recorded on a Nicolet Magna IR 550 Series II FTIR spectrometer equipped with a deuterated triglycine sulfate KBr detector and purged with dry air from a Whatman FTIR

Purge Gas Generator (Model 75-52). The IR cell consisted of a temperature-controlled cell mount (Harrick) and CaF_2 windows (13 x 2 mm) separated by 6-μm (for samples in H_2O) or 56-μm (for samples in D_2O) Teflon spacers (Wilmad). The IR cell temperature was controlled using an Omega CN8500 temperature controller and monitored with a thermocouple placed in close proximity to the CaF_2 windows.

3.3.2 Methods

Typically 2 mg of lyophilized cyt c was dissolved in 40 μl (5% w/v or 4 mM) of 50 mM sodium phosphate/0.2 M KCl buffer in D_2O (pD 7.0) or H_2O (pH 7.0). Approximately 8 μl of cyt c solution was pipetted onto a CaF_2 window, the cell immediately assembled and placed in the IR instrument. The cell temperature controller was programmed to increase the temperature by 2°C every 10 min between 25 and 95°C, and the FTIR spectrum was collected after the sample had thermally equilibrated at each temperature setting (~ 10 min). To *selectively* titrate the *buried* NH protons, prior to recording spectra in D_2O, the protein solutions were heated to 40°C and cooled to 25°C for three cycles to accelerate H/D exchange. This was chosen as the method of exchange-out since no further shifts in the amide I' bands were observed at room temperature following cycling to 40°C, and samples stored in D_2O for 6 days at 4°C exhibited identical amide I' maxima to those reported here.

All reported spectra are an average of 256 scans recorded at a resolution of 2 cm^{-1} using a Happ-Genzel apodization with a velocity and aperture of 0.9494 cm/s and 67, respectively. Fourier transform self-deconvolution of the amide I bands was carried out employing a half width at half height (HWHH) of 15 cm^{-1} and an enhancement (K factor)

of 1.2. Subtraction of water absorption from the spectra recorded in H_2O was performed by the method of Dong and coworkers (*65, 117*). Gaussian curves were used for quantitative analysis (Galactic PeakSolve) of the deconvolved FTIR spectra. Peak maxima in the deconvolved spectra were identified from the peak minima observed in the second-derivative spectra. Following iterative fitting of Gaussian curves to the deconvolved spectra, the relative amounts of secondary structure were determined from the curve-fitted areas under bands assigned to a particular structure (*21, 111, 118*). The tyrosine absorption band (1516-1515 cm^{-1}) was used to normalize all the intensity data presented here since, as previously reported (*119*), tyrosine absorption was unaffected by temperature and H/D exchange.

3.4 Results and Discussion

3.4.1 Thermal Titration of the FTIR Spectra of the Cytochromes at pD 7.0

Insight into differences in conformational stability between the cyts c is obtained from an examination of the temperature dependence of their FTIR spectra. At elevated temperatures, intermolecular β-sheets are formed in many proteins that result in the appearance of bands characteristic of aggregation (*111*). Such bands are clearly visible in the 69°C spectrum of horse cyt c at 1615 and 1683 cm^{-1} (Figure 3.1) and reach maximum intensity at ~ 73°C. The onset of aggregation occurs between 73 and 77°C in bovine cyt c (data not shown), and between 65 and 70°C in tuna c (data not shown). It is of note that the aggregation bands appear above 80°C in the horse cyt c FTIR spectra in the absence of 0.2 M KCl (*21*).

Loss of secondary structure is coincident with aggregation. The temperature at the midpoint (T_m) of the backbone unfolding transitions for the three cyts c can be obtained from plots of the total integrated intensity of the amide I' envelope (1700-1600 cm^{-1}) vs temperature. Such plots are compared in Figure 3.2 for the cyts c in D_2O, and the T_m values follow the order: cow (74°C) > horse (70°C) > tuna (65°C). Similarly, plots of the 1615-cm^{-1} aggregation-band or α-helical amide I' (1640-1660 cm^{-1}) intensities vs temperature (data not shown) yielded the same T_ms, confirming that aggregation accompanies loss of secondary structure as reported for other proteins (*111*). The order of the T_ms observed here for the three cyts c agrees well with those reported by calorimetry (*85*) and CD (*9*), but the values are over 10°C lower than those obtained in the absence of 0.2 M KCl (*21, 85*), which was added to the samples in the present study because the limited-proteolysis studies were performed in 0.2 M KCl (*9, 10*). The perturbing effects of KCl and other salts on cyt c conformation (*97*) would explain the >10°C reduction in our T_ms, which cannot be ascribed to the high protein concentrations (4 mM) used in the FTIR studies since a T_m of 82°C was previously reported for the FTIR-monitored thermal denaturation of 5 mM horse cyt c in the absence of KCl (*21*). A significant increase in amide I' intensity is observed for all the cyts c prior to loss of secondary structure and aggregation (Figure 3.2). The amide I' increase below T_m is due to broadening of the amide I' bands, while the 60% increased intensity in the unfolded forms is due to the presence of the aggregation bands (Figure 3.1).

Stability of protein tertiary structure can be determined by FTIR by monitoring H/D exchange of peptide NH protons (*21, 67, 68, 111*). Protons on the surface of a protein or present in highly mobile regions exchange rapidly whereas buried NH protons

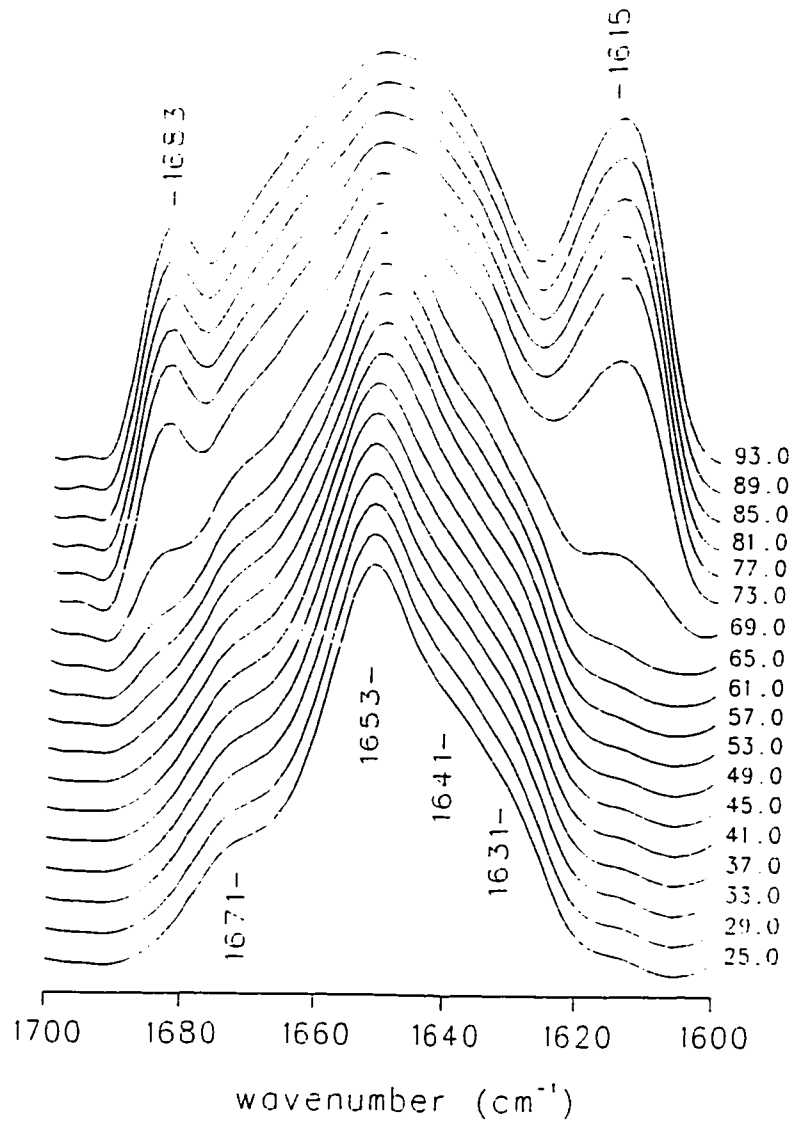

Figure 3.1. Deconvolved spectra in the amide I' (D_2O) region of 4 mM horse cytochrome c in 50 mM sodium phosphate/0.2 M KCl buffer (pD 7.0) vs temperature. The cell was allowed to equilibrate for 10 min at each temperature before a new spectrum was recorded. Each spectrum is the average of 256 scans recorded at 2-cm^{-1} resolution in cells with 56-μm path-lengths. Parameters used in deconvolution were a HWHH of 15 cm^{-1} and K factor of 1.2.

exchange more slowly because the exchange rates are decreased by solvent inaccessibility and strong H-bonding in secondary structures (*21, 67, 68, 111*). Incorporation of deuterium into the cyts c at room temperature is ~ 90% complete as estimated from the ratio of the integrated intensity of the amide II bands in D_2O and H_2O (data not shown). The regions that account for the ~ 10% residual amide II intensity in D_2O at room temperature are likely the center of the C-terminal α-helix and the solvent inaccessible bulky hydrophobic residues in contact with the heme. Bai and coworkers (*88*) reported that residues 94-99 of the C-terminal α-helix (residues 90-100) of horse cyt c exhibit no H/D exchange during local unfolding but exchange through the major unfolding pathway and, using mass spectrometry to monitor H/D exchange, Zhang and Smith (*120*) observed that residues 29-33 adjacent to the heme are shielded from the solvent. Thermal titrations of the ~ 10% residual integrated (1600-1525 cm^{-1}) amide II intensity of the cyts c are shown in Figure 3.2, in addition to the amide I' profiles. The amide II transitions above 60°C are assigned to the H/D exchange from the unfolded state that occurs as the backbone unfolds since the T_ms (65, 70 and 74°C for tuna, horse and cow cyts c, respectively) are identical to those observed for the amide I'-monitored loss of secondary structure (Figure 3.2). Transition temperatures are also seen in the amide II profile of tuna cyt c at 35 and 50°C, and in horse and cow cyts c at 54 and 57°C, respectively. Since pre- and post-transition baselines are not well defined for all these transitions below 60°C, *transition temperatures* are quoted rather than *transition midpoints* for consistency. The amide II transition temperature at 35°C is identical to the transition temperature observed in the biphasic conversion of tuna cyt c to its alkaline isomer as monitored by 695-nm absorption (35°C) (*11*) and close to that estimated from

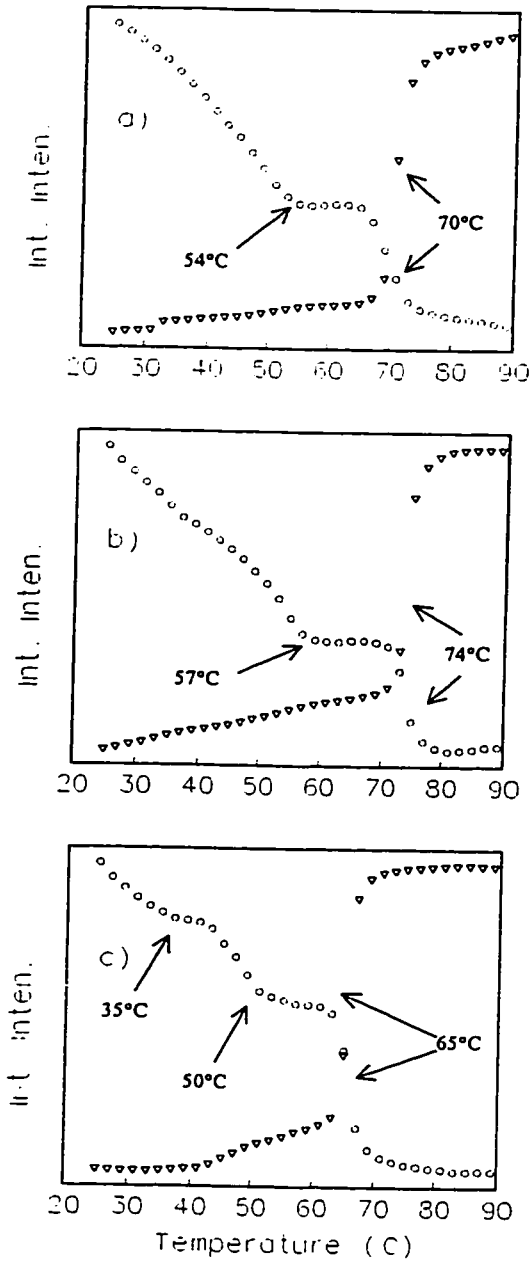

Figure 3.2. Plot of the integrated intensities of the (Δ) amide I' (1700-1600 cm^{-1}) and (o) residual amide II (1600-1525 cm^{-1}) bands of (a) horse, (b) cow and (c) tuna cytochromes c at pD 7.0 vs temperature. H/D exchange was ~ 90% complete in D_2O at 25°C (see text) prior to recording the FTIR spectra vs temperature using the experimental conditions given in Figure 3.1. The arrows indicate the transition temperatures for the amide II transitions below 60°C, and the T_ms for both the amide I' and II transitions corresponding to global unfolding above 60°C. Note that the amide I' intensity increased by ~ 60% between 25 and 90°C.

changes in the formal heterogeneous electron-transfer rate constants (32°C) (*85*), reported from 695-nm intensity measurements for horse (53°C) and cow (58°C) cyts c. Likewise, 54 and 57°C correspond to the alkaline isomerization transition temperatures respectively (*11*). From the amide II data in Figure 3.2, it can be seen that tertiary folding intermediates appear above the alkaline-isomerization transition temperatures, with the tuna cyt c intermediate appearing about 20°C lower (~ 35-45°C) than those for the mammalian cyts c (~ 55-70°C). An additional stable tertiary intermediate is observed for tuna cyt c following its second thermally induced transition at 50°C.

Since CN^- binds to cyt c by displacing the Met80 ligand (114-116), the CN^--adducts are purported to resemble the alkaline isomers (12). In this context, it is of interest that the well-defined 35°C-amide II transition observed in Figure 3.2c is absent from the titration curve of CN^--ligated tuna cyt c in Figure 3.3b. In contrast, the CN^--adducts of both tuna (Figure 3.3b) and horse cyts c (Figure 3.3a) exhibit defined transition temperatures at 50 and 54°C, respectively, like their free forms (Figure 3.2a,c). Thus, CN^--ligated horse cyt c also undergoes tertiary structural transitions at the temperature corresponding to the alkaline isomerization of the native protein, indicating that ligand exchange is not central to this conformational change. It is of interest that the CN^--adducts appear to possess less stable tertiary intermediates but more stable secondary structure below 60°C (Figure 3.2 vs 3.3) than in the native proteins, which may explain why CN^--ligation exerts little effect on the global stability of horse cyt c to acid and guanidine hydrochloride denaturation (*121*). The identical T_ms from the amide I' vs temperature profiles for native (Figure 3.2a,c) and CN^--ligated horse (70°C) and tuna

cyts c (65°C) (Figure 3.3a,b) also reveal that CN^--ligation does not alter the global stability of the cyts c to thermal denaturation.

3.4.2 Implications of the FTIR Results for the Mechanism of Alkaline Isomerization of Tuna vs Horse and Cow Cytochromes c

The alkaline isomerization of horse cyt c is reportedly a complex process involving ionization with a pK_a of 11, followed by conformational change and ligand replacement with a pK_c of -2 at room temperature (*14*):

$$H^+N_{H/M} \overset{K_a}{\rightleftharpoons} N_{H/M} + H^+ \qquad (3.1)$$

$$N_{H/M} \overset{K_c}{\rightleftharpoons} A_{H/X} + A_{H/Y} \qquad (3.2)$$

where $N_{H/M}$, refers to the native (His18 and Met80 ligation) protein, and $A_{H/X}$ and $A_{H/Y}$ to alkaline (His18 and X or Y ligation) conformations with different axial ligands but with very similar properties (*13, 15-19*). The identity of the group that ionizes in step 3.1 is unknown but is speculated to be a Lys residue (*16, 18*). The X and Y ligands in step 3.2 are proposed to be Lys72 and Lys79 in horse cyt c (*19*), and Lys73 and Lys79 in yeast cyt c (*18*), where Lys72 is trimethylated. Since the CN^- adduct of horse cyt c also undergoes conformational change at the same transition temperature (54°C) as the native protein (Figures 3.2a and 3.3a), substitution by a lysine of the Met80 ligand is not the driving force for this transition.

It has been established for horse cyt c that the high-temperature conformation at neutral pH is identical to the alkaline conformation at 25°C (*13*). The temperature

dependence of the *apparent* pK_a ($pK_{app} = pK_a + pK_c$), which is ~ 9 at 25°C, arises mainly from that of K_c in step 2 (*12, 14*). Although tuna and horse cyts c reportedly possess identical pK_{app}s at 25°C (*66*), their temperature dependence clearly must differ given that tuna cyt c undergoes alkaline isomerization 20°C lower than horse cyt c at pH 7.0 (Figure 3.2a vs 3.2c) (*11, 85*). It has been proposed that the ionization of Tyr46, which is replaced by Phe in horse and cow cyts c (*98*), triggers the alkaline isomerization of tuna cyt c. Since both free and CN^--ligated tuna cyt c exhibit an amide II transition at 50°C similar to that in horse cyt c at 54°C (Figures 3.2 and 3.3), comparable conformational change probably occurs between 50 and 57°C in the free and ligated forms of *all three* cyts c examined here. It is speculated that ionization of the same residue triggers this change in each protein, which would require ionization of two residues in tuna cyt c between 25 and 65°C. In fact, this is consistent with the pH-rate profiles for the alkaline isomerizations of tuna vs horse cyt c, which can be fit by two and one ionizations, respectively (*98*). The following scheme summarizes the proposed thermally induced transitions in tuna cyt c based on its amide II thermal titration profile:

$$H_2^{2+}N_{H/M} \overset{K_{a1}}{\rightleftharpoons} H^+N_{H/M} + H^+ \qquad (3.3)$$

$$H^+N_{H/M} \overset{K_{c1}}{\rightleftharpoons} H^+A_{H/X} \qquad (3.4)$$

$$H^+A_{H/X} \overset{K_{a2}}{\rightleftharpoons} A_{H/X} + H^+ \qquad (3.5)$$

$$A_{H/X} \overset{K_{c2}}{\rightleftharpoons} A^{\bullet}_{H/X} + A^{\bullet}_{H/Y} \qquad (3.6)$$

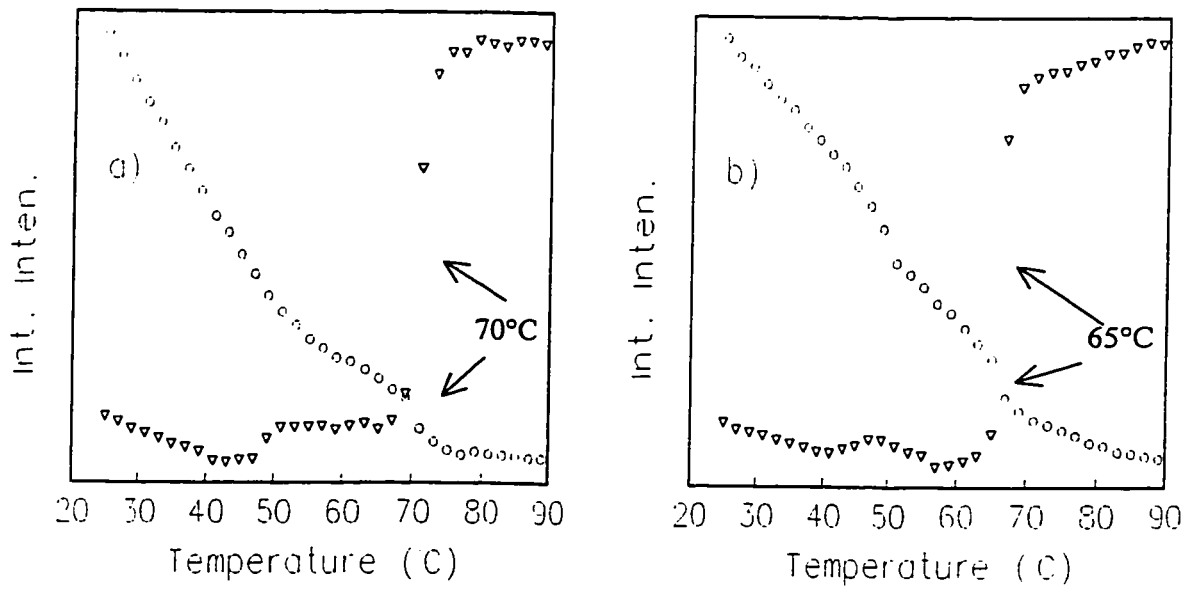

Figure 3.3. Plot of the integrated intensities of the (Δ) amide I' (1700-1600 cm-1) and (o) amide II (1560-1525 cm^{-1}) bands at pD 7.0 vs temperature for the CN^--adducts of (a) horse and (b) tuna cytochromes c. The arrows indicate the T_ms for both the amide I' and II transitions corresponding to global unfolding above 60°C. Experimental conditions are given in Fig. 3.1.

In this scheme, $pK_{a1} + pK_{c1}$ corresponds to the pK_{app} reported for tuna cyt c at 25°C (*98*). We speculate that X = Lys79 in step 3.4 since substitution of Met80 by Lys79 would involve mainly local conformational change in the heme pocket, which would be strongly influenced by CN^--ligation as observed in the amide II titrations (Figure 3.2c vs 3.3b). In step 3.6, $A^*_{H/X}$ and $A^*_{H/Y}$ represent the high-temperature isomers of tuna cyt c, where X is assumed to be Lys79, and Y is Lys72 and/or Lys73, based on their proposed identities in horse (*19*) and yeast (*18*) cyts c.

3.4.3 Curve Fitting of the Amide I/I' Regions of the 25 °C FTIR Spectra

The deconvolved spectra of horse, cow and tuna cyts c in the amide I (1700-1600 cm^{-1}) region (Figures 3.4a-c) were compared to further probe differences between the cyts c that might provide a structural basis for the different mechanism of alkaline isomerization in tuna cyt c. Clearly, the amide I envelope for the tuna cyt c differs from those of the mammalian cyts c, although the X-ray (*2, 109*) and NMR solution structures (*104, 105*) reveal that tuna and horse cyts c, which are variant at 18 out of 103 residues, possess virtually identical main-chain folds, and a closely conserved H-bonding network. To understand the significance of the differences in peptide-backbone IR absorption, curve fitting of the amide I envelopes, which are highly sensitive to secondary structure (*63*), was carried out. The intensities were assigned based on the known secondary structures of the proteins from X-ray and NMR data. In estimating the relative amounts of different secondary structures by curve fitting the composite amide I bandshapes, it is important that the components have comparable band widths (*21*) and that a minimum number of bands are used to prevent overfitting of the data (*111*). Furthermore, it is

assumed that the FTIR amide I absorptivities of the secondary structural elements are the same, so that the areas under the fitted bands correspond to the number of residues found in a given secondary structure (*65, 66*).

The deconvolved spectrum of horse cyt c (Figure 3.4a and Table 3.1) in the amide I (1700-1600 cm^{-1}) region at pH 7.0 can be curve-fitted by six components with similar bandwidths (~ 13 cm^{-1}). These are assigned to different secondary structural elements (Table 3.2) based on consensus literature assignments (*63-65, 110, 111, 117, 122*). The peaks at 1670 and 1680 cm^{-1}, which account for 23% of the amide I intensity in horse cyt c (Table 3.1), are assigned to the amide I absorption of turns (Table 3.2). This correlates well with the high-resolution crystallographic (*2*) and NMR (*123*) structures which show that there are six 3_{10}-turns, involving 23% of the residues (24 out of 104) in the protein (Table 3.3). The peak found at 1636 cm^{-1} with 21% relative intensity is attributed to extended-chain structure (*21*), and extended-chain absorption has also been assigned to the 1646-cm^{-1} band with 7% relative intensity (Tables 3.1 and 3.2) (*117*). The X-ray (*2*) and NMR (*105*) studies reveal 30 and 34%, respectively, extended-chain structure in the protein, consistent with 28% total extended-chain FTIR absorption (Table 3.3). The most prominent band at 1657 cm^{-1} (47% intensity) is assigned to α-helical structure based on literature assignments (*64, 66*). This is in excellent agreement with the X-ray (47%) and NMR (43%) data (Table 3.3). The weak band at 1617 cm^{-1} with 2% relative intensity is assigned to the side-chain absorption of the Lys and Arg residues in horse cyt c (*124*).

The curve-fitting results show that the secondary structure of cow cyt c (Figure 3.4b and Table 3.3) consists of 21% turns, 47% α-helix and 30% extended chain, similar to horse cyt c (Tables 3.1 and 3.3). Although no X-ray data are available for cow cyt c,

its structure is expected to be very similar to that of horse cyt c since the two cyts c are variant at only 3 out of 104 residues (*1*). At first glance the quantitative FTIR analysis suggests that tuna cyt c contains only 27% α-helix (1659-cm^{-1} band; Figure 3.4c and Table 3.1), which is low based on the 45% helical structure revealed in the X-ray data (Table 3.3). Typically, α-helical absorption is assigned in the range 1650-1658 cm^{-1} (*63, 68, 122*), but it has also been assigned to absorption below 1650 cm^{-1} (*125, 126*). Hence, 18% relative intensity at 1649-cm^{-1} is assigned to α-helical absorption to yield the total of 45% relative helical intensity predicted from the X-ray data (Table 3.3). This assignment also results in 27% *total* extended-chain absorption (9% centered at 1649 cm^{-1} and 18% at 1635 cm^{-1}), in good agreement with the X-ray data (32%; Table 3.3). Consistent with contributions from both helical and extended-chain absorption, the 1649-cm^{-1} band is blue-shifted and broadened (HWHH = 13 cm^{-1}) in tuna cyt c relative to the corresponding band (1646 cm^{-1}) in horse and cow cyts c (HWHH = 10 cm^{-1}; Table 3.1). Finally, the assignment of the 26% intensity at 1682 and 1671 cm^{-1} to turns (Table 3.2), agrees well with the structural data since the 3_{10}-turns in tuna cyt c make up 23% of the residues in the protein (*109*) (Table 3.3).

Curve-fitting of the D_2O spectra yields amide I' components similar to those in H_2O with the expected ~ 4-5-cm^{-1} red shifts due to small contributions from peptide NH in-plane-bending vibrations (Table 3.1) (*63, 64*). However, the bands at ~ 1670 and 1641 cm^{-1} in D_2O have gained intensity at the expense of the 1680-cm^{-1} band in H_2O, which is assigned to 3_{10}-turn absorption (Table 3.2). A 3_{10}-turn resembles one turn of a 3_{10}-helix, and Dwividi and coworkers (*127*) calculated that 3_{10}-helical structure should have amide I absorptions at 1686 and 1646 cm^{-1} in H_2O, while Kennedy and coworkers (*128*)

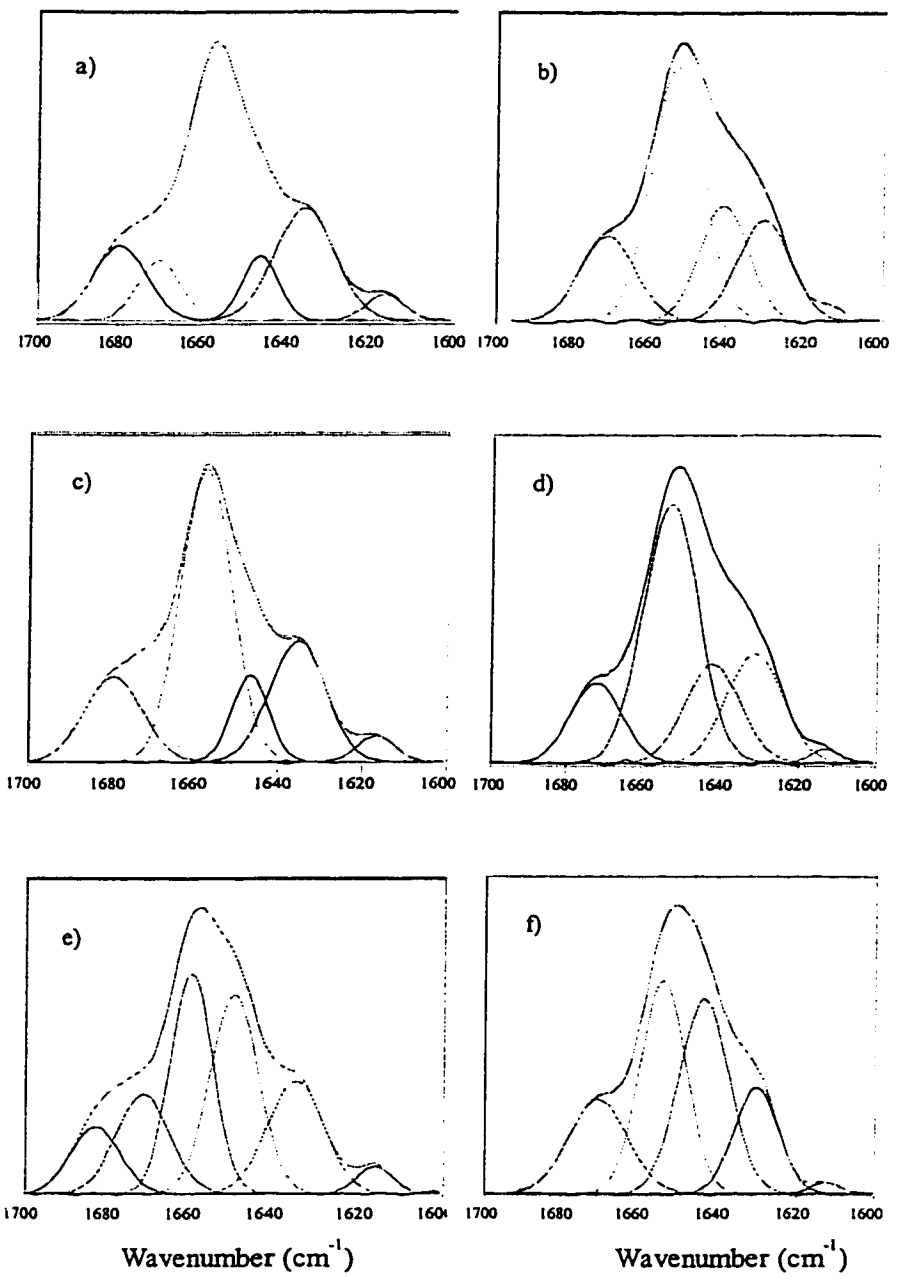

Figure 3.4. Deconvolved and curve-fitted FTIR spectra in the amide I (H_2O) and I' (D_2O) regions of (a, b) horse, (c, d) cow and (e, f) tuna cytochromes c. The proteins (4 mM) were in 50 mM sodium phosphate/0.2 M KCl buffer (pH/pD 7.0) at 25°C. Spectra were recorded using 6-μm (H_2O) or 56-μm (D_2O) path-lengths under the experimental conditions given in Figure 3.1 and details of the curve-fitting procedure are given in the text.

Table 3.1. Curve-fitting Parameters [Frequency (ν, cm^{-1}), % Area, and HWHH (cm^{-1})] for FTIR Amide I and I' Bands of Native Horse, Cow, and Tuna Cytochromes c and the CN^--Adducts of the Horse and Tuna Proteins[a]

Cytochrome c	H_2O			D_2O (Native)			D_2O (CN^--adduct)		
	ν	% Area	HWHH	ν	% Area	HWHH	ν	% Area	HWHH
Horse	1680	14	15	-	-	-	-	-	-
	1670	9	12	1671	17	17	1671	16	17
	1657	47	15	1653	45	15	1652	49	15
	1646	7	10	1641	19	15	1639	17	13
	1636	21	17	1631	18	16	1630	17	15
	1617	2	10	1613	1	8	1614	1	7
Cow	1679	15	17	-	-	-	-	-	-
	1670	6	10	1672	14	16	-		-
	1657	47	14	1653	47	17	-	-	-
	1646	9	10	1642	18	17	-	-	-
	1635	21	15	1631	20	17	-	-	-
	1617	2	10	1613	1	9	-	-	-
Tuna	1682	10	14	-	-	-	-	-	-
	1671	16	15	1670	19	18	1670	18	17
	1659	27	12	1654	30	14	1654	29	13
	1649	27	13	1645	35	15	1645	32	14
	1635	18	16	1631	15	13	1631	19	15
	1616	2	10	1612	1	9	1612	2	9

[a]Data from Figures 3.4 and 3.5

Table 3.2. Assignment of Secondary Structural Elements to FTIR Amide I and I' Absorption Bands for Native Horse, Cow, and Tuna Cytochromes c and the CN^--Adducts of the Horse and Tuna Proteins[a]

Cytochrome c	Secondary Structure Element	H_2O		D_2O (Native)		D_2O (CN^--adduct)	
		ν (cm^{-1})	% Area	ν (cm^{-1})	% Area	ν (cm^{-1})	% Area
Horse	turns	1680	14	1671	17	1671	16
	turns	1670	9	1641	6	1639	12
	α-helix	1657	47	1653	45	1652	49
	extended chain	1646	7	1641	12	1639	5
	extended chain	1636	21	1631	18	1630	17
Cow	turns	1679	15	1672	14	-	-
	turns	1670	6	1642	9	-	-
	α-helix	1657	47	1653	47	-	-
	extended chain	1646	9	1642	9	-	-
	extended chain	1635	21	1631	20	-	-
Tuna	turns	1682	10	1670	19	1670	18
	turns	1671	16	1644	5	1645	9
	α-helix	1659	27	1654	30	1654	29
	α-helix	1649	19	1644	19	1645	20
	extended chain	1649	8	1644	11	1645	3
	extended chain	1635	18	1630	15	1631	19

[a]Data from Figures 3.4 and 3.5

Table 3.3. Comparison of Amide I and I' Assignment for Horse, Cow, and Tuna Cytochromes c with Literature FTIR, X-ray and NMR Data

Cytochrome c	Secondary Structral Element	FTIR				X-ray[d]	NMR[e]
		H_2O[a]	D_2O[a]	H_2O[b]	D_2O[c]		
Horse	turns	23	23	25	27	23	23
	α-helix	47	45	42	36	47	43
	extended-chain	28	30	33	35	30	34
Cow	turns	21	23	-	-	-	-
	α-helix	47	47	-	-	-	-
	extended-chain	30	29	-	-	-	-
Tuna	turns	26	24	-	-	23	23
	α-helix	46	49	-	-	45	43
	extended-chain	26	26	-	-	32	34

[a]Data from Figure 3.4

[b]Data from (*65*)

[c]Data from (*21*)

[d]Horse data from (*2*) and tuna from (*109*)

[e]Data from (*105*)

reported that peptides known to contain 3_{10}-helical structure exhibit strong amide I absorption at 1666-1662 cm^{-1} with weak components near 1679 and 1646 cm^{-1}. If 6% of the increased absorption at 1641-cm^{-1} in D_2O is assigned to the low-frequency absorption of 3_{10}-turns (Table 3.2), the total turn intensity in the amide I' region of horse cyt c would agree with the X-ray data (23%; Table 3.3). Likewise, adjustment of the total turn intensity to 23% in cow cyt c requires the assignment of 9% turn intensity to the 1642-cm^{-1} amide I' band (Table 3.2).

A 1:1 ratio is observed for the areas of the 1659- and 1649-cm^{-1} amide I bands in tuna cyt c, which is attributed to splitting of the α-helical absorption (Table 3.2). However, in D_2O the 1644-cm^{-1} band area is greater than that of the 1654-cm^{-1} band, and the 5% increased area is assigned to 3_{10}-turn absorption in D_2O (Table 3.2). Although no 3_{10}-turn intensity is assigned below 1670 cm^{-1} in the H_2O spectra (Table 3.2), it is possible that turns do contribute intensity to the lower frequency amide I bands. Nonetheless, it seems that in H_2O high-frequency turn absorption is dominant, while in D_2O the low-frequency component gains intensity at the expense of the high-frequency components. H/D isotope red shifts on the order of 30-40 cm^{-1} cannot be ascribed to simple mass effects, and specific mechanisms by which D_2O perturbs the 3_{10}-turn modes are not obvious. Mantsch and coworkers (*129*) assign β-turn intensity above 1660 cm^{-1} to non-H-bonded carbonyls, whereas carbonyls involved in intramolecular H-bonding give rise to intensity at or below ~ 1640 cm^{-1}. Thus, increased intramolecular H-bonding in turn structures in D_2O compared to H_2O would be consistent with our assignment (Table 3.2), and with the greater stability of deuterium bonds compared to hydrogen bonds (*130*). We wish to emphasize, however, that since H-bonding within turns is less

well defined than in α-helices or β-sheets, we rely on the detailed structural information available for the cyts c for the assignments given in Table 3.2. Clearly, the main difference detectable by FTIR in the room-temperature secondary structure of tuna compared to horse and cow cyts c is the splitting of the α-helical structures in the tuna protein into two populations, and some minor variations in the 3_{10}-turns. On the other hand, the observation of very similar amide I and I' components for the horse and cow cyts c strongly supports the assumption that the two proteins possess almost identical structures.

Interestingly, a comparison of Figures 3.4d and 3.5a for horse cyt c, and Figures 3.4f and 3.5b for tuna cyt c reveals that the native and CN^--ligated forms possess essentially identical secondary structure at 25°C. Thus, the variation in α-helical absorption cannot be attributed to differences in Met80 ligation, but to the differences in primary structure discussed next.

3.4.4 Structural Basis for Splitting of α-Helical Absorption in Tuna Cytochrome c

It has been suggested (*125*) that amide I vibrations at the ends of α-helices are different from those in the center, which introduces the concept of ordered (strongly H-bonded) and disordered (weakly H-bonded) α-helices. Stability of α-helices can be decreased by removal of salt bridges within the helix and by destabilization of helical dipoles (*131*). Both of these factors probably serve to destabilize the N-terminal helix (residues 3-12) of tuna relative to horse cyt c since the substitution Glu4 (horse) by Ala (tuna) results in loss of the salt bridge between Glu4 and Lys8, as well as the loss of the

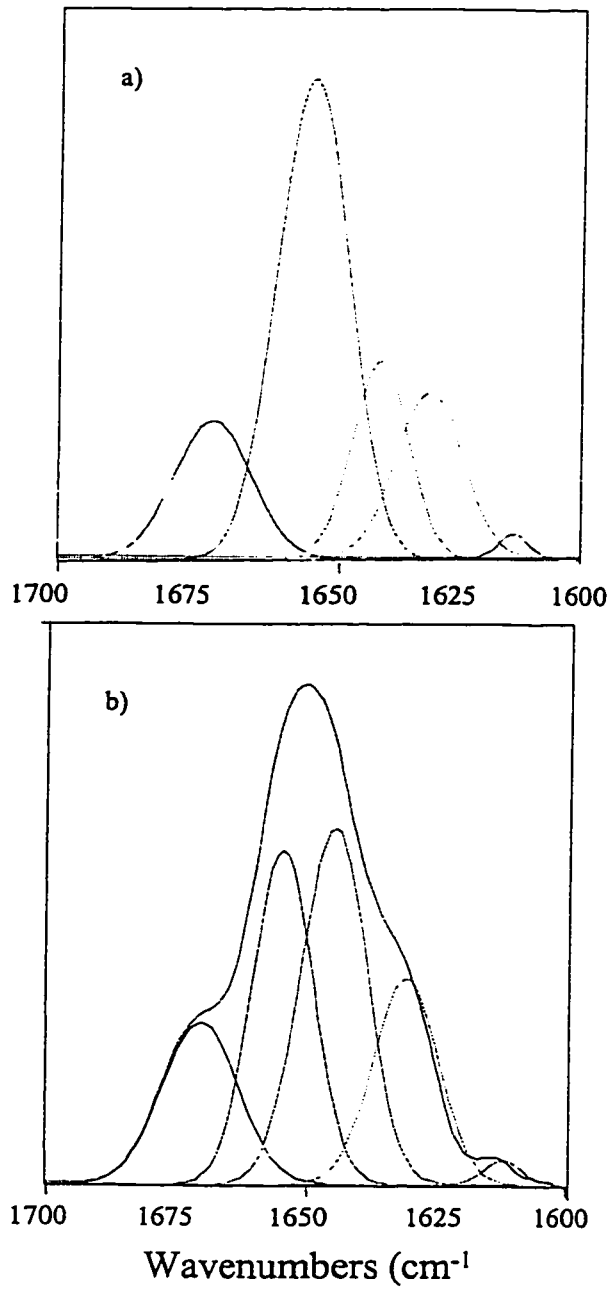

Figure 3.5. Deconvolved and curve-fitted FTIR spectra in the amide I' (D_2O) region of the CN^--adducts of (a) horse and (b) tuna cytochromes c. Protein (4 mM) was added to 50 mM sodium phosphate/0.2 M KCl buffer (pD 7.0) containing 6 mM KCN. Experimental conditions are given in Fig. 3.1 and details of the curve-fitting procedure in the text.

dipole-compensating effect of Glu4. However, the largest backbone-proton NMR shifts between horse and tuna cyts c involve residues 58-62 at the beginning of the 60s helix (residues 58-69), indicating subtle structural differences between horse and tuna cyt c in this region, while the helical stability from residues 64 to 69 is hardly affected (*104, 105*). The substitution of Lys60 and Glu61 in horse cyt c by the neutral residues Asn60 and Asn61 in tuna cyt c results in a difference in solvation of this region which likely decreases the stability of the heme crevice of tuna c. Moreover, rules proposed by Chou & Fasman (*132*) to predict secondary structure suggest that Asn residues favour turns, while Lys and Glu are strong helix formers.

Additionally, large chemical shifts in the backbone protons (residues 90, 91, 94, 97 and 99) of the C-terminal helix (residues 90-100) between horse and tuna cyts c were observed by NMR. These are due to substitutions that result in decreased residue size [Ile95 (horse) by Val (tuna)] or charge removal [Glu92 (horse) by Gln (tuna); Lys100 (horse) by Ser (tuna)], which could weaken H-bonding in the C-terminal α-helix of tuna cyt c compared to that in horse cyt c (*105*). Only minor chemical shifts were reported for the two other α-helical stretches, the 50s helix (residues 49-55) and the 70s helix (residues 70-75) (*104, 105*). Thus, the NMR-monitored variation in stability of regions of the N-terminal, C-terminal and 60s α-helices between horse and tuna cyts c offers a structural basis for splitting of α-helical FTIR absorption in the latter. Conservation of their heme and axial-ligand NMR signals (*133*), as well as the similarity of their amide I and I' bands, suggest that the structural differences observed between horse and tuna cyts c do not apply to horse and cow cyts c, which share 97% sequence identity.

3.5 Conclusions

Heating at neutral pH results in the formation of low- and high-temperature conformational isomers of tuna cyt c. Formation of the low-temperature isomer corresponds to the 695-nm-monitored alkaline isomerization of tuna cyt c at 33-35°C. This isomerization, which is speculated to result in the substitution of the Met80 ligand by Lys79, does *not* involve the same ionization trigger nor the same conformational change as the alkaline isomerization above 50°C of horse and cow cyts c, since the trigger and conformational change associated with the latter are probably the same as those involved in the high-temperature (50°C) isomerization of tuna cyt c. Lys79, Lys73 and Lys72 are likely axial ligands in the conformational isomers of all three cyts c above 50°C. CN^--ligation essentially abolishes the well-defined amide-II-monitored low-temperature isomerization of tuna cyt c, but the high-temperature isomerization is observed for both the tuna and horse cyt c CN^--adducts as in the free proteins. The evolution of a separate "low-temperature" alkaline isomerization with its own trigger in a cyt c from a cold-blooded species such as tuna strongly supports the hypothesis that open-closed heme-crevice transitions are important in the physiological function of cyt c (*20*). As pointed out previously (*85, 98*), the thermal conformational lability of the heme pocket of tuna cyt c may be a necessary consequence of the lower physiological temperature of tuna compared to the mammalian species. However, the strength of Met80 ligation, which controls the flexibility of the heme pocket (*10, 11*), does not play a role in stabilizing the secondary structure of cyt c since the amide I' regions of the FTIR spectra of the free and CN^--ligated cyts c from horse and tuna are found to be identical, as are the T_ms obtained by following loss of secondary structure.

The present study highlights the power of FTIR spectroscopy in probing protein conformational changes. Specifically, to our knowledge, we show here for the first time that selective thermal titration of amide II intensity of the buried peptide NH groups in D_2O can provide detailed information on tertiary folding intermediates. The sensitivity of this approach stems from the high intensity of the amide II absorption and the fact that NH/ND exchange results in ~ 100 cm^{-1} red shift in the amide II envelope.

4.0 Two-dimensional Infrared Correlation Spectroscopy as a Probe of Sequential Events in the Thermal Unfolding of Cytochromes c

4.1 Abstract

The sequential unfolding events of horse, cow and tuna cyt c as a function of increasing temperature over the range 25-81°C were investigated by resolution-enhanced 2D IR correlation spectroscopy. The 2D IR analysis revealed that in the thermal denaturation of the two mammalian cyts, the overall sequence of unfolding is similar, with denaturation of extended-chain and turn structures occurring prior to unfolding of α-helices, followed by denaturation of residual stable extended-chain structures. In tuna cyt c, denaturation of all extended-chain structures precedes the unfolding of α-helices. Moreover, in cow cyt c unfolding of all helical components occurs as one cooperative unit, but in horse and tuna cyts c, the helical components behave as subdomains that unfold separately, as proposed recently by Englander and coworkers for horse cyt c (*88, 139*). At higher temperatures, following the loss of secondary structure, protein aggregation occurs in the three cyts c. The data presented here establish that variations in the thermal unfolding of cyts c can be associated with specific sites in the protein that influence local flexibility yet have little affect on global stability. This study demonstrates the power of resolution-enhanced 2D IR correlation spectroscopy in probing unfolding events in homologous proteins.

4.2 Introduction

Cyt c mediates the transfer of electrons from cyt c reductase to cyt c oxidase in the electron transport chain of eukaryotes (*1-3*). X-ray analysis of horse cyt c (Figure 4.1) reveals a single polypeptide chain organized into five α-helical segments (yellow) interconnected by six β-turns (green) and extended-chain structures (blue), which account for ~ 45, 25 and 30% of its amino acid residues, respectively. X-ray and NMR data for horse and tuna cyts c reveal that both proteins possess remarkably similar main-chain structures (*2, 104, 105, 109*). Cow cyt c is assumed to be essentially identical in structure to horse cyt c since the two proteins share high sequence identity (> 97%). Notwithstanding the overall similar structural elements, the proteins exhibit significant differences in local stabilities as probed by tryptic digestion (*9-11*), FTIR spectroscopy (*93*) and 695-nm absorption (*4, 8, 11, 12*). However, global conformational stabilities, as monitored by CD (*9*), calorimetry (*85*) and FTIR (*93*), are remarkably similar for cyts c.

To probe the different local stabilities observed for cyts c, FTIR spectroscopy was used to obtain information at the level of secondary structure from curve-fitting of the amide I (H_2O) and amide I' (D_2O) bands (*93*). Essentially identical secondary structural elements were observed in horse and cow cyt c, whereas splitting of the α-helical absorption in tuna cyt c indicated the presence of less stable helical structures. Monitoring the FTIR amide I' bands of the cyts c as a function of temperature revealed that loss of secondary structure and protein aggregation occurred within a narrow range (< 10°C). To determine whether sequential events are involved in thermal unfolding of the cyts c, we have re-examined our FTIR data (*93*) using generalized 2D IR correlation analysis (*71*), which is capable of detecting minor structural changes in response to

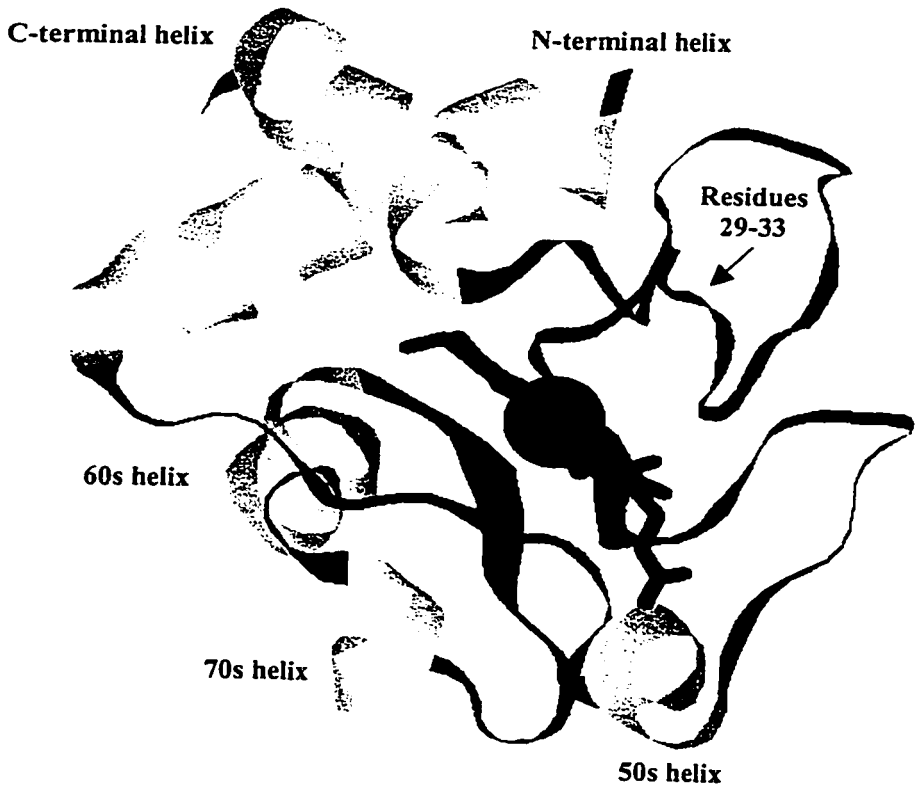

Figure 4.1. Horse heart cyt c C_α backbone with its heme (red), helical ( ), turns (green) and extended-chain (blue) structures. The model was generated using Rasmol and the crystal structure coordinates from Protein Data Bank entry 1HRC (*2*).

external perturbations such as temperature (*69, 134*). For example, 2D IR analysis revealed that the Cro repressor protein forms stable intermediates only after specific secondary structures are unfolded first, which was not observed from simple FSD analysis (*69*). Likewise, Wang and coworkers (*70*) observed ovalbumin protein peaks by 2D IR that were detected in neither the raw nor second-derivative spectra. The present 2D IR analysis of the thermal denaturation of cyts c, reveals that the sequence of events in the unfolding of structurally homologous proteins can vary significantly.

4.3 Experimental Procedures

4.3.1 IR Spectroscopy

FTIR spectra were recorded previously for cyts c from horse (Type VI), cow and tuna (Type XI) (Sigma) (*93*). Typically, after H/D exchange was complete, 8 μl of a 4-mM cyt c solution in 50 mM sodium phosphate buffer (pD 7.0) containing 0.2 M KCl was sandwiched between two CaF_2 windows (Wilmad) separated by a 56-μm Teflon spacer (Harrick Scientific). Spectra were recorded on a Nicolet Magna IR 550 Series II FTIR spectrometer equipped with a deuterated triglycine sulfate KBr detector. The cell temperature was increased by 2°C between 25 and 95°C, and the FTIR spectrum was collected after the cell was thermally equilibrated for 10 min. Spectra represent an average of 256 scans recorded at a resolution of 2 cm^{-1} using a Happ-Genzel apodization with a velocity and aperture of 0.9494 cm/s and 67, respectively. To improve band resolution, FSD of the amide I' bands was carried out using Omnic 3.1 software (Nicolet), employing a HWHH of 13 cm^{-1} with a K factor of 2.

4.3.2 2D IR Analysis

Generalized 2D IR correlation analysis of the FSD amide I' (1600-1700 cm^{-1}) spectra taken every 4°C between 25 and 81°C was carried out as described previously (*134*) using KG2D software written by Wang (*70*). A 5% correlation-intensity cut off was used to generate both low- and high-resolution 2D IR plots for all three cyts c, and 2D analysis performed on duplicate sets of FTIR thermal denaturation spectra resulted in reproducible 2D correlation plots. The KG2D software can process any spectral data (e.g., Raman scattering, infrared or ultraviolet/visible absorption) that can be imported by Grams/32 4.01 software (Galactic). Moreover, the change in the spectroscopic signal can be due to any physical variable, such as temperature (used here), time, pressure or denaturant concentration. The advantage of using the KG2D software is that it allows 3D representations of the 2D contour maps to be examined using Grams/3D 3.02 software (Galactic). Rotating and zooming the 3D image aids in the identification of weak peaks in the 2D maps. However, caution must be exercised when generating 2D synchronous and asynchronous contour maps from spectra subjected to resolution enhancement algorithms such as FSD. In particular, overdeconvolution can give rise to artifacts in the deconvolved spectra that can be easily misinterpreted as amide I' band components (*135*). In the present work, a signal-to-noise ratio in the amide I' absorption region of >25,000:1 and residual water vapour absorption of <0.1 milliabsorbance units were established as criteria for FSD. As suggested by Jackson and Mantsch (*136*), the absence of artifacts in the deconvolved spectra was verified by confirming that the number of bands and their positions in the deconvolved spectra matched those in second-derivative spectra generated from the same raw spectral data.

4.3.3 Interpretation of 2D IR Correlation Plots

Two types of 2D correlation plots are generated, synchronous and asynchronous, which represent the in-phase and out-of-phase variation, respectively, between spectral components to an applied perturbation. The asynchronous contour plot combined with the synchronous plot provide details on the sequence of events following an applied perturbation. As a result of the symmetric and antisymmetric properties of the cross-correlation peaks with respect to the diagonal line in the 2D plots, only peaks above the diagonal are discussed. Peaks are identified as X vs Y cm^{-1}, where X and Y represent the frequencies marked on the X and Y-axes, respectively. Throughout this paper, solid and dashed lines in the 2D plots denote positive and negative correlation peaks, respectively. According to the rules proposed by Noda (*71*), the sign of a cross peak (positive or negative) in the asynchronous plots determines the sequential relationship between two bands. When the system is perturbed by increasing the temperature, as in the present study, a positive region in the asynchronous map indicates that the spectral intensity change at X occurs at lower temperature than that at Y if the corresponding synchronous peak at X vs Y is also positive. On the other hand, if the synchronous peak at X vs Y is negative, the spectral intensity change at X occurs at higher temperature than that at Y. A negative peak in the asynchronous map is interpreted in a similar manner; i.e., X changes at higher (lower) temperature if the synchronous X vs Y peak is positive (negative).

4.4 Results and Discussion

4.4.1 Thermal Unfolding of Horse, Cow and Tuna Cyts c

Prior to reporting the 2D IR analysis of the thermal denaturation of cyts c, the

previous 1D analysis will be summarized (*93*). Curve-fitting of the FSD amide I' spectra of horse and cow cyts c, which consisted of four bands (1671, 1653, 1641 and 1631 cm^{-1}), revealed similar secondary structural elements. Bands attributed to α-helices, at 1653 cm^{-1} in horse and cow cyts c, and at 1654 and 1645 cm^{-1} in tuna cyt c, decrease in intensity with increasing temperature (Figures 4.2a-c). Splitting of the α-helical absorption into two populations (1654 and 1645 cm^{-1}) in tuna cyt c reveals the presence of less stable helical structures (*93*), that likely include the 60s helix (residues 61-70) based on NMR data (*104, 105*). Loss of absorption in horse and cow by turns at 1671 and 1641 cm^{-1} (1670 and 1644 cm^{-1} in tuna cyt c), and extended-chain structures at 1641 and 1631 cm^{-1} (1644 and 1630 cm^{-1} in tuna cyt c) accompanies the loss of helical absorption in the three cyts c. New bands at ~ 1616 and 1684 cm^{-1}, due to intermolecular antiparallel β-sheets resulting from irreversible aggregation of the unfolded protein (*135, 137, 138)*, grow in between 65-74°C. The intensities of the bands at 1684 and 1616 cm^{-1} remained constant above 75°C as seen in Figure 4.2. Upon cooling from 95 to 25°C, the aggregation bands remained unchanged, demonstrating that the denaturation of the protein was irreversible (data not shown). The T_m for aggregation and loss of secondary structure, as monitored by intensity changes in the amide I' bands, overlap at 74°C (bovine), 70°C (horse) and 65°C (tuna) in the 1D plots (*93*).

Only a limited amount of information on the sequence of unfolding events can be obtained from the 1D spectra. A more sensitive approach, such as resolution-enhanced 2D IR analysis is required to detect minor out-of-phase variations due to non-cooperative events during the thermal unfolding process (*69*). The assignments of the peaks in the 2D IR plots are summarized in Tables 4.1-4.3 and are discussed next.

4.4.2 2D IR Correlation Plots of Horse Cyt c

In the synchronous 2D IR plot of horse cyt c (Figure 4.3a), three auto-correlation peaks (along the diagonal) centered at 1684, 1652 and 1616 cm^{-1} are observed, indicating that the relative intensities of these bands change with increasing temperature. The elongated autopeak centered at 1652 cm^{-1} in the synchronous plot (Figure 4.3a) is broad with low resolution, suggesting that additional peaks are buried underneath. Hence, a 3D representation of the 2D map was generated (data not shown) and, as expected, autopeaks at 1637 and 1630 cm^{-1} were detected. The positive cross-correlation peak at 1684 vs 1616 cm^{-1} indicates that the peak intensities assigned to aggregation are changing in the same direction. Likewise, positive intensity at 1652 vs 1637 cm^{-1} and 1652 vs 1630 cm^{-1} indicates that the absorptions assigned to α-helices (1652 cm^{-1}), turns/extended-chains (1637 cm^{-1}) and extended-chains (1630 cm^{-1}) are changing in the same direction. Two negative cross-correlation peaks are observed at 1684 vs 1652 cm^{-1} and 1652 vs 1616 cm^{-1}, revealing that the unfolding of α-helices (1652 cm^{-1}) is accompanied by protein aggregation (1684 and 1616 cm^{-1}).

Cross-correlation peaks in the asynchronous plot for horse cyt c (Figure 4.3b) indicate that peak intensities of some secondary structure components vary out-of-phase (i.e., are accelerated or delayed) with respect to each other as the temperature is increased. Thus, the thermal unfolding of horse cyt c involves sequential events that can be interpreted from the 2D IR correlation maps. Since the cross-correlation peaks at 1684 vs 1652 cm^{-1} and 1684 vs 1637 cm^{-1} are positive in the asynchronous map but negative in the synchronous map, denaturation of α-helical (1652 cm^{-1}) and turns/extended-chains (1637 cm^{-1}) precedes protein aggregation (1684 cm^{-1}). The

negative cross-correlation peaks in the asynchronous maps (1652, 1637 and 1630 vs 1616 cm^{-1}) can be interpreted in a similar manner, with the secondary structure elements denaturing at lower temperature than protein aggregation. Thus, despite the apparent overlap of their T_m values in the 1D integrated intensity vs temperature plots (*93*), loss of secondary structure and protein aggregation are not synchronous events in horse cyt c.

To examine the sequential thermal unfolding of secondary structures in horse cyt c (Figure 4.1) in greater detail, a set of synchronous and asynchronous plots with higher resolution were generated over the range 1660-1625 cm^{-1} (Figures 4.3c, d). In the asynchronous map, the positive cross peak (1652 vs 1630 cm^{-1}) reveals that the α-helices (1652 cm^{-1}) unfold before denaturation of the extended-chains (1630 cm^{-1}), whereas the negative cross peak (1652 vs 1637 cm^{-1}) indicates that disruption of turns/extended-chains (1637 cm^{-1}) occurs before loss of α-helical structures (1652 cm^{-1}). Moreover, a positive peak at 1637 vs 1630 cm^{-1} reveals denaturation of turns/extended-chain structures (1637 cm^{-1}) prior to extended-chains (1630 cm^{-1}). A positive cross-correlation peak (1652 vs 1647 cm^{-1}) exposes the existence of a 1647-cm^{-1} band, which we assign to low-frequency α-helices, based on previous curve-fitting of the 1D spectra (*93*). Hence, unfolding of α-helical components in horse cyt c does not occur simultaneously but sequentially, with the helices that absorb at higher frequency denaturing at lower temperature.

The sequence of intensity changes of peaks assigned to the secondary structural elements (Figure 4.1) in the thermal denaturation of horse cyt c is summarized in Table 4.1. Recently, NMR H/D-exchange experiments performed on native horse cyt c implicated a sequential unfolding pathway, where unfolding of cooperative structural

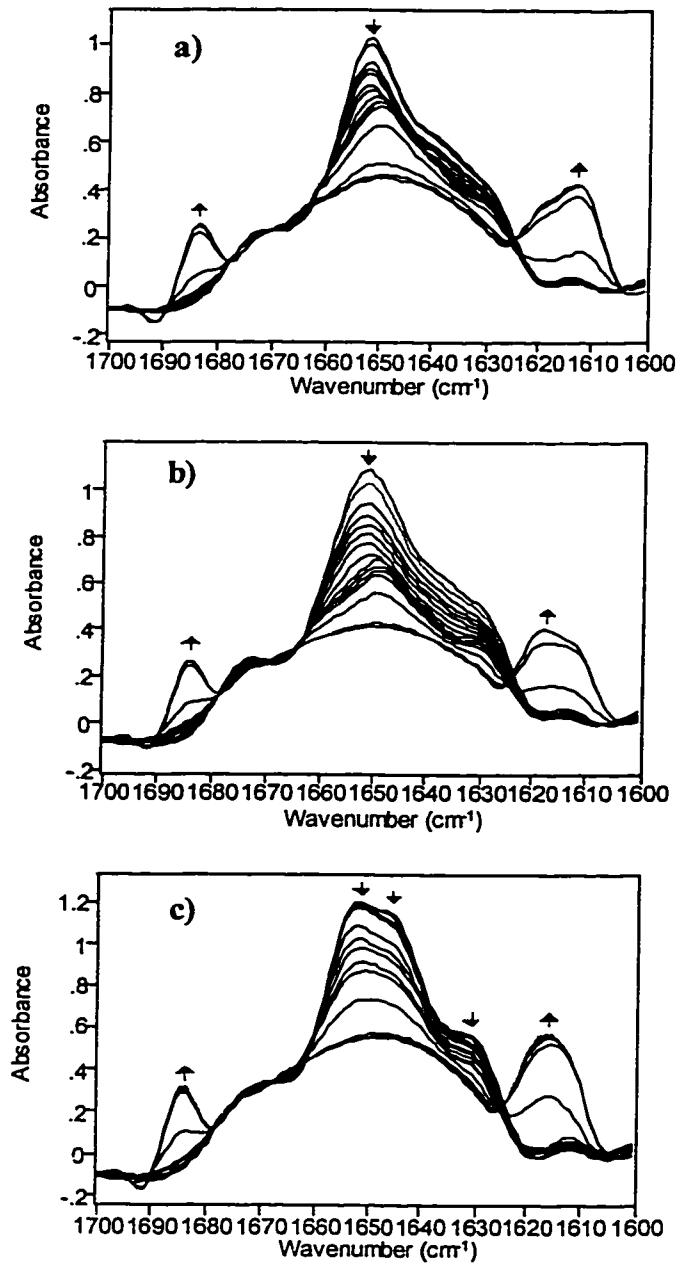

Figure 4.2. Stacked absorbance vs temperature (25-81°C) plots of the deconvolved amide I' (D_2O) bands of 4 mM (a) horse, (b) cow and (c) tuna cyts c in 50 mM sodium phosphate buffer containing 0.2 M KCl (pD 7.0). Experimental details are given in the text. Vertical arrows represent an increase (↑) or decrease (↓) in the band intensity as the temperature is raised. The temperature interval per trace is 4°C and the data were plotted using Omnic 3.1 software (Nicolet). The aggregation bands (1616 and 1684 cm^{-1}) reach ~ 1/3 their final intensities at 69, 73 and 65°C in (a), (b) and (c), respectively.

Table 4.1. Correlation table for the deconvolved FTIR spectra of horse cyt c over the temperature range 25-81°C[a-e]

cm^{-1}	1684↑	1652↓	1647↓	1637↓
1630↓	−+⇒	++⇐	+ ⇔	++⇐
1637↓	−+⇒	+−⇒	+−⇒	
1647↓	−+⇒	++⇐		
1652↓	−+⇒			
Sequence of events for individual components				
⇓	turns / extended chains (1637 cm^{-1})↓ less stable α-helices (1652 cm^{-1})↓ extended chains (1630 cm^{-1})↓ and α-helices (1647 cm^{-1})↓ intermolecular antiparallel β-sheet (1684 cm^{-1})↑			

[a] Spectral data from Figure 4.2a.

[b] Row and column headings represent the Y and X frequencies, respectively from the 2D maps in Figure 4.3.

[c] Vertical arrows represent an increase (↑) or decrease (↓) in the band intensity as the temperature is raised.

[d] The signs (+ −) of the X, Y peaks above the diagonal in the 2D synchronous maps (left-hand sign) and asynchronous (right-hand sign) are indicated.

[e] Horizontal arrows indicate the sequence of intensity changes: Y ⇒ X and Y ⇐ X denote that the intensity change at Y occurs at lower (⇒) or higher (⇐) temperature than that at X; Y ⇔ X denotes that the intensity changes at Y and X are synchronous.

Table 4.2. Correlation table for the deconvolved FTIR spectra of cow cyt c over the temperature range 25-81°C[a-e]

cm^{-1}	1684↑	1652↓	1637↓
1630↓	− + ⇒	+ + ⇐	+ + ⇐
1637↓	− + ⇒	+ − ⇒	
1652↓	− + ⇒		
Sequence of events for individual components			
⇓	turns / extended chains (1637 cm^{-1})↓ α-helices (1652 cm^{-1})↓ extended chains (1630 cm^{-1})↓ intermolecular antiparallel β-sheet (1684 cm^{-1})↑		

[a] Spectral data from Figure 4.2b.

[b] Row and column headings represent the Y and X frequencies, respectively from the 2D maps in Figure 4.4.

[c-e] See footnotes to Table 4.1.

Table 4.3. Correlation table for the deconvolved FTIR spectra of tuna cyt c over the temperature range 25-81°C[a-e]

cm^{-1}	1684↑	1652↓	1646↓
1630↓	−+⇒	+−⇒	+−⇒
1646↓	−+⇒	+−⇒	
1652↓	−+⇒		

Sequence of events for individual components

⇓

extended chains (1630 cm^{-1})↓

turns / extended chains (1646 cm^{-1})↓ and less stable α-helices (1646 cm^{-1})↓

α-helices (1652 cm^{-1})↓

intermolecular antiparallel β-sheet (1684 cm^{-1})↑

[a] Spectral data from Figure 4.2c.

[b] Row and column headings represent the Y and X frequencies, respectively from the 2D maps in Figure 4.5.

[c-e] See footnotes to Table 4.1.

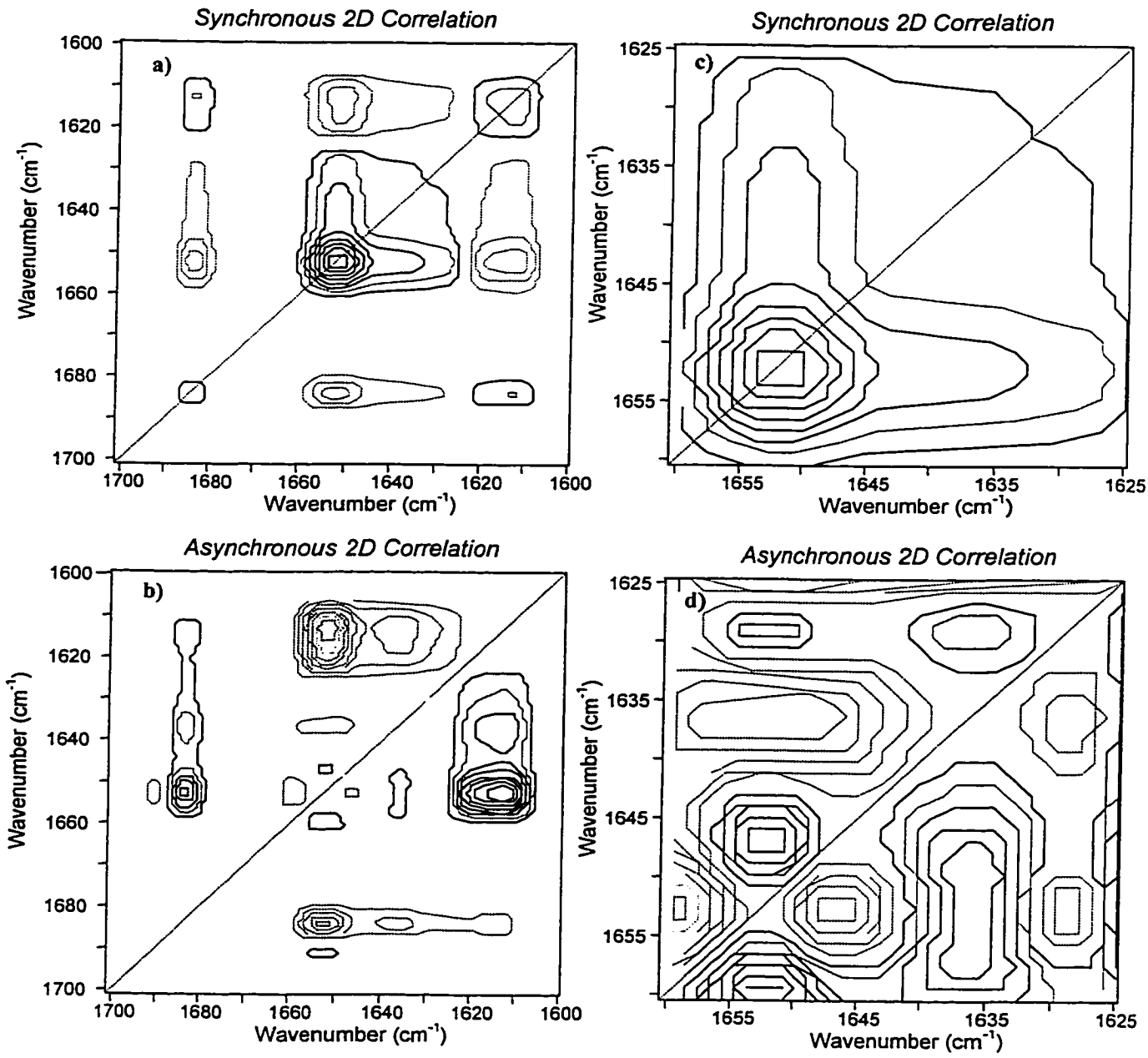

Figure 4.3. 2D IR (a, c) synchronous and (b, d) asynchronous maps of the amide I' absorption of horse cyt c constructed from the spectral data in Figure 4.2a. 2D correlation plots were generated using KG2D software (*70, 134*) over the full amide I' region (1600-1700 cm^{-1}) and the expanded helical region (1660-1625 cm^{-1}) to increase resolution. Solid and dashed lines represent positive and negative correlation peaks, respectively.

units occurs as a function of temperature (*88, 139*). It was proposed that global unfolding is initiated by unfolding of the cooperative unit containing residues 71-85, followed by a loop between residues 36-61; these changes are consistent with the initial loss in intensity we observe at 1637 cm^{-1} (turns/extended chain). Next, the 60s helix (residues 61-70) and a region between residues 20-35 denature as a cooperative unit, which can be associated with the 1652 and 1630 cm^{-1} absorption bands, respectively. The final transition to the globally unfolded state is marked by the simultaneous unfolding of the N-terminal (residues 3-12) and C-terminal (residues 90-100) helices (*88, 139*), consistent with the unfolding of low-frequency α-helices (1647 cm^{-1}) transpiring before the onset of aggregation at 1684 and 1616 cm^{-1} (Table 4.1).

4.4.3 2D IR Correlation Plots of Cow Cyt c

Due to their high sequence identity and similar local and global stabilities (*9, 11, 8, 93, 121*), one would expect the sequence of unfolding events to be very similar for horse and cow cyts c. The synchronous map of cow cyt c (Figure 4.4a) reveals essentially the same broad autopeak centered at 1652 cm^{-1} detected for horse cyt c (Figure 4.3a). Autopeaks at 1637 and 1630 cm^{-1} are detected when a 3D representation of the 2D map is plotted (data not shown) and the improved resolution afforded by the 3D representation revealed additional autopeaks (1684 and 1616 cm^{-1}), as seen in the horse cyt c 2D map (Figure 4.3a). Negative cross-correlation peaks at 1684 vs 1652 cm^{-1} and 1652 vs 1616 cm^{-1} indicate that α-helical intensity (1652 cm^{-1}) changes in the opposite direction to aggregation (1684 and 1616 cm^{-1}). Positive intensity at 1652 vs 1637 and 1630 cm^{-1} reveals that the absorption at 1652 cm^{-1} (α-helices) changes in the same

direction as that centered at 1637 (turn/extended-chain) and 1630 cm^{-1} (extended-chain). In summary, from the 2D synchronous plot of cow cyt c it can be concluded that as the temperature is increased, denaturation of turn/extended-chain (1637 cm^{-1}), α-helical (1652 cm^{-1}) and extended-chain (1630 cm^{-1}) structures is accompanied by protein aggregation (1684 and 1616 cm^{-1}) as was observed for horse cyt c.

An elongated positive cross-correlation peak (1684 vs 1652, 1637 and 1630 cm^{-1}) and a broader elongated negative cross-correlation peak (1652, 1637 and 1630 vs 1616 cm^{-1}) are detected in the asynchronous plot of cow cyt c (Figure 4.4b). Hence, aggregation (1684 and 1616 cm^{-1}) of cow cyt c also occurs at higher temperature following denaturation of its α-helices (1652 cm^{-1}), turn/extended-chain (1637 cm^{-1}) and extended-chain structures (1630 cm^{-1}). However, the absence of an α-helical cross peak (1652 vs 1647 cm^{-1}) in the high-resolution asynchronous map of cow cyt c (Figure 4.4d) reveals cooperative unfolding of *all* its α-helical structures. This must be due to the three amino acid substitutions in cow cyt c, two of which actually occur in helical segments: Lys60 (horse) → Gly60 (cow) and Thr89 (horse) → Gly89 (cow). The third substitution is in a loop region, Thr47 (horse) → Ser47 (cow).

Table 4.2 summarizes the correlation peaks observed in the synchronous and asynchronous maps of cow cyt c, and the sequence of the thermally induced intensity changes that reveal the sequential events in unfolding. Initially there is disruption of extended-chain and/or turn structures (1637 cm^{-1}) followed by the cooperative unfolding of the helical components (1652 cm^{-1}), then denaturation of extended-chain structures (1630 cm^{-1}). The appearance of aggregation bands (1684 and 1616 cm^{-1}) at higher temperature establishes that the protein is denatured. Thus, using the 2D IR approach,

global-stability variations between horse and cow cyts c (*9, 11, 93, 121*) can be pinpointed to differences in the unfolding sequence of their helical structures (Table 4.1 vs 4.2), which renders the cow protein more thermally stable than the horse protein.

4.4.4 2D IR Correlation Plots of Tuna Cyt c

The 1D stacked (Figure 4.2c) and 2D synchronous (Figure 4.5a) plots reveal that helices (1652 and 1646 cm^{-1}), turns (1646 cm^{-1}), extended-chain structures (1646 and 1630 cm^{-1}) and aggregation bands (1616 and 1684 cm^{-1}) change in intensity with increasing temperature as seen for horse and cow cyts c. The presence of cross-correlation peaks in the asynchronous plot (Figure 4.5b) indicates that the various structural components of tuna cyt c respond differently to increasing temperature as summarized in Table 4.3. Elongated positive asynchronous cross peaks (1685 vs 1652, 1646 and 1630 cm^{-1}) and corresponding negative synchronous peaks (Figure 4.5a) imply that helical (1652 and 1646 cm^{-1}), turn (1646 cm^{-1}) and extended-chain (1646 and 1630 cm^{-1}) structures denature prior to aggregation (1684 cm^{-1}) as in horse and cow cyts c.

Several weak cross-correlation peaks are observed in the high-resolution 2D correlation maps (1625-1660 cm^{-1}) of tuna cyt c (Figure 4.5c, d). For instance, negative correlation peaks at 1652 vs 1630 cm^{-1} and 1646 vs 1630 cm^{-1} in the asynchronous plot (Figure 4.5d) reveal that low-frequency extended-chain structures (1630 cm^{-1}) lose intensity before the α-helices, contrary to what was found for horse and cow cyts c. Furthermore, the negative correlation peak at 1652 vs 1646 cm^{-1} indicates that the low-frequency helices (1646 cm^{-1}) unfold before the high-frequency helices (1652 cm^{-1}), which is opposite to that observed for horse cyt c (Table 4.1 vs 4.3). Curve fitting of the 1D spectra (*10*) revealed splitting of the helical absorption in tuna cyt c with ~20%

intensity at the lower frequency. In contrast, splitting of the helical absorption of horse cyt c was only detected using the more sensitive 2D analysis (Figure 4.3d) but even this approach failed to detected helical splitting in cow cyt c (Figure 4.4d). Since H-bonding of the peptide carbonyl red-shifts the amide I' absorption (*63*), low-frequency helices are more strongly H-bonded and/or more solvent exposed than those at higher frequencies. Red-shifting of the helical absorption in tuna cyt c has been attributed to increased solvent exposure, yielding helices that are less stable and unfold at lower temperature than the more buried helices with 1652-cm^{-1} absorption (*93*). Following loss of secondary structure, protein aggregation occurs, giving rise to bands at 1684 and 1616 cm^{-1}.

The difference in the sequence of unfolding events in tuna compared to horse and cow cyts c can ultimately be linked to the less stable heme-crevice of the tuna protein (*11, 93*). Using mass spectrometry to monitor H/D exchange in horse cyt c, Zhang and Smith (*120*) observed that residues 29-33 (Figure 4.1), which form an extended-chain structure adjacent to the heme, are shielded from the solvent. Assuming that residues 29-33 contribute to the low-frequency extended-chain absorption (1630 cm^{-1}) of tuna cyt c, their denaturation before α-helices (Table 4.3) would be consistent with the significantly decreased stability of the heme crevice in tuna vs horse or cow cyts c (*11, 93*).

In summary, subtle but significant differences in the sequence of thermal unfolding events are detected by 2D correlation analysis of the FTIR spectra of horse, cow and tuna cyts c shown in Figure 4.2. Despite their high sequence identity (> 97%), horse and cow cyts c exhibit non-identical thermal unfolding pathways, with helical structures denaturing sequentially in horse cyt c, but cooperatively in cow cyt c (Table

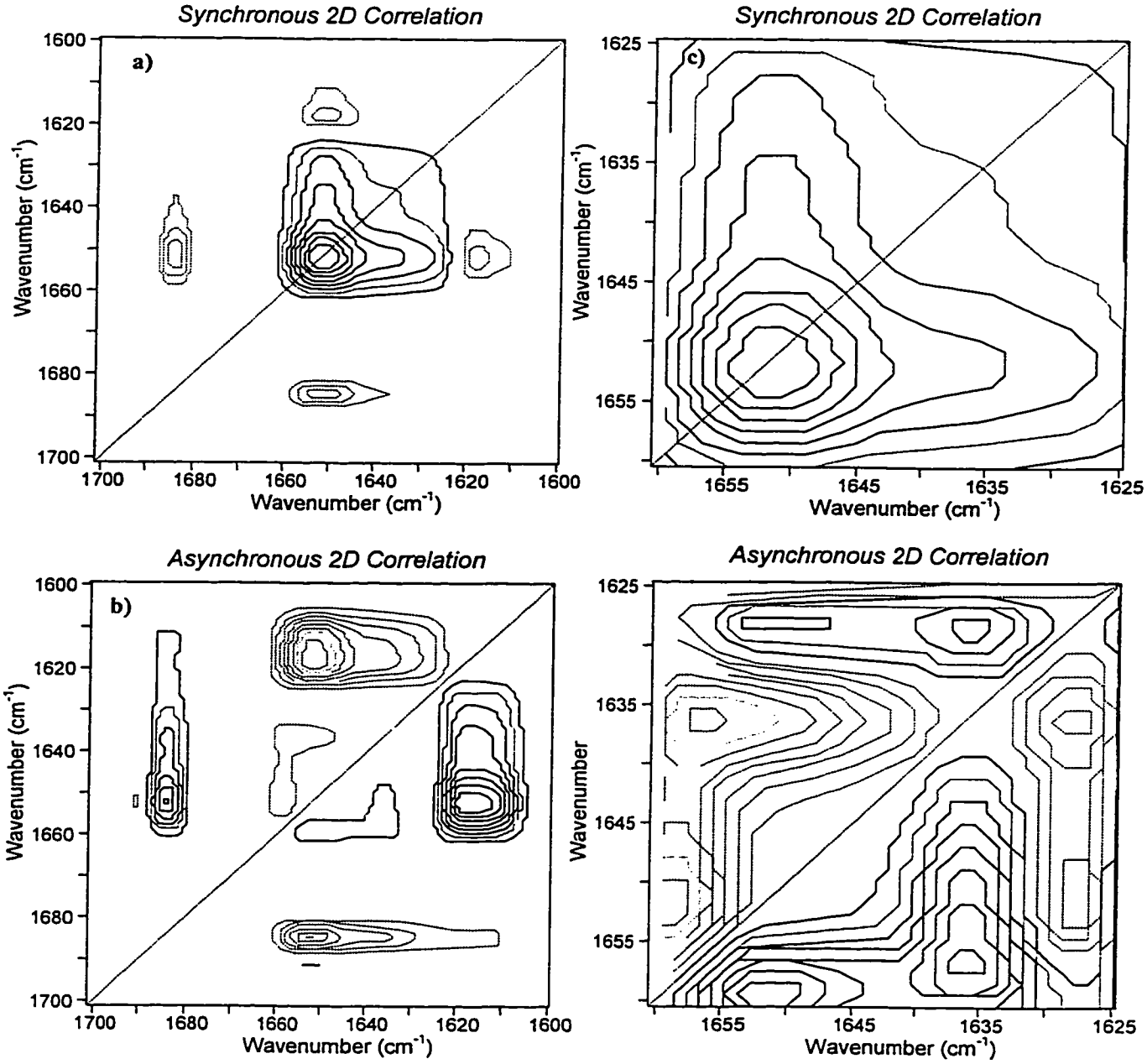

Figure 4.4. 2D IR (a, c) synchronous and (b, d) asynchronous maps of the amide I' absorption of cow cyt c constructed from the spectral data in Figure 4.2b. See caption to Figure 4.3.

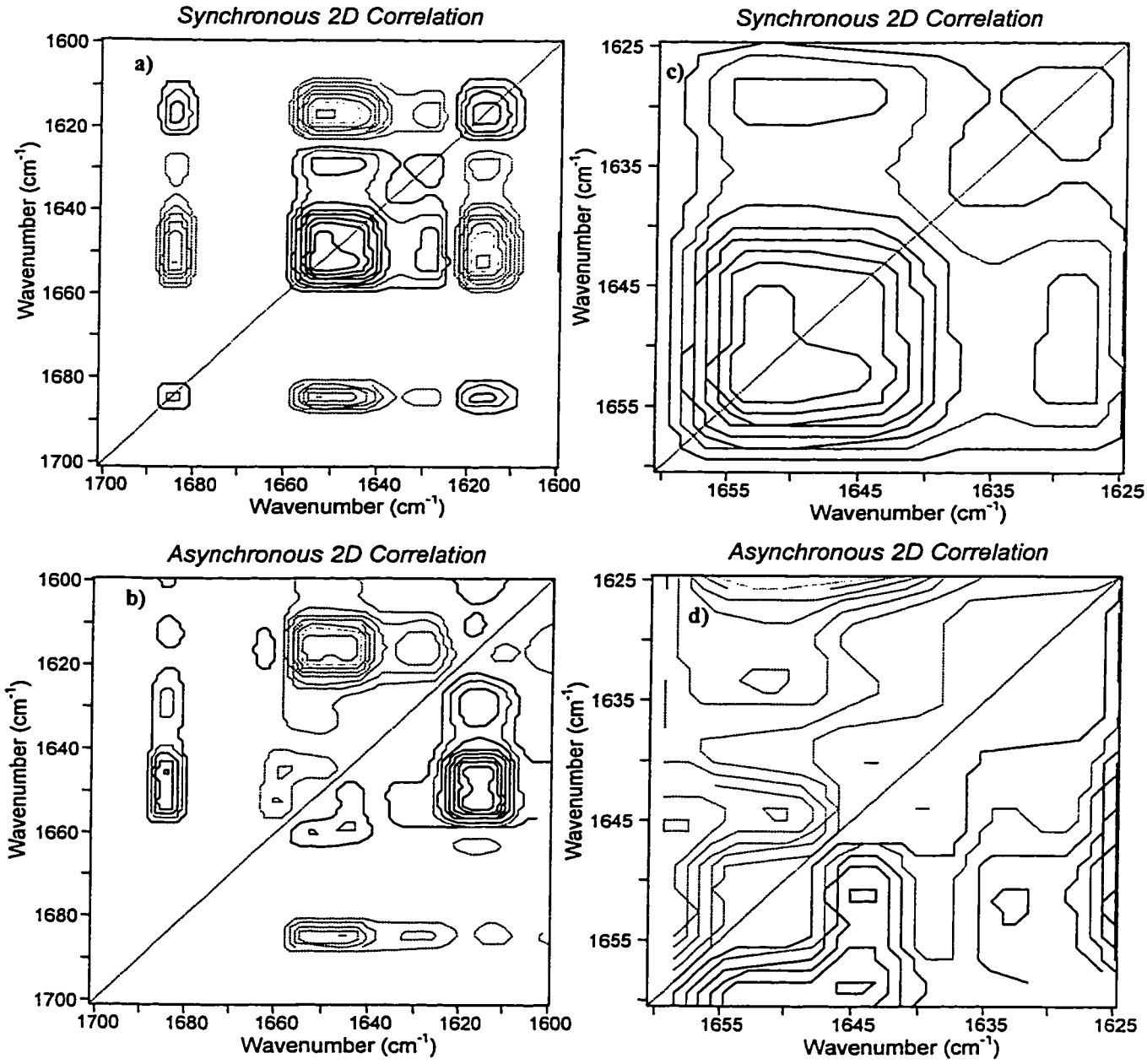

Figure 4.5. 2D IR (a, c) synchronous and (b, d) asynchronous maps of the amide I' absorption of tuna cyt c constructed from the spectral data in Figure 4.2c. See caption to Figure 4.3.

4.1 vs 4.2). The first step in tuna cyt c thermal denaturation involves alteration of low-frequency extended-chain structures (Table 4.3), which include residues 29-33 in the heme-crevice region (Figure 4.1); in contrast, this is the most stable region in horse cyt c (*120*) and very likely in cow cyt c also (Table 4.2). Hence, decreased stability of the heme crevice in tuna cyt c (*9, 11, 93*) determines the sequence of unfolding events as the temperature is increased. Nevertheless, variations in local stability and unfolding do not have a dramatic affect on overall stability, since the global unfolding of all three cyts c occurs within a narrow 10°C range (65-75°C) (*9, 93*). It is also of note that the overlapping T_m values for the global stability obtained from the 1D FTIR analyses (*93*) suggested that loss of secondary structure and aggregation occur in parallel, but the 2D analyses clearly show that these are sequential events; the denatured proteins aggregate, rather than aggregation promoting denaturation.

4.5 Conclusions

Using a highly homologous set of proteins, horse, cow and tuna cyts c, with solved X-ray (*2, 109*) and NMR (*104, 105*) structures, we have demonstrated the power of resolution-enhanced 2D IR correlation analysis in identifying the relative stabilities of secondary structures. The results are consistent with those from NMR H/D exchange experiments performed on horse cyt c, which reveal that specific structural units unfold cooperatively (*88, 139*). The present study also illustrates the usefulness of resolution-enhanced 2D IR correlation analysis in detecting subtle changes in structural components and in uncovering sequential events in unfolding following thermal perturbation. Clearly, a powerful feature of this approach is the ability to distinguish between structural

elements with overlapping absorption (*69, 134*) such as α-helices of varying stabilities. In future studies one can envision modifying key structural residues to relate differences found by 2D IR correlation analysis in unfolding/refolding pathways to specific sites. Furthermore, since the acquisition of FTIR spectra is rapid, requires little sample, and FTIR equipment is relatively inexpensive, 2D IR screening should provide an invaluable tool for identifying candidate proteins for structure determination by NMR or X-ray crystallography in whole-proteome studies.

5.0 Heme-mediated Oxidation of Ferricytochrome c by H_2O_2: An Apoptotic Trigger?

5.1 Abstract

UV/Vis spectroscopy was employed to monitor the reaction of cyt c with excess H_2O_2. Following manual and stopped-flow mixing, no spectroscopic evidence was obtained for the formation of an oxyferryl heme intermediate in cyt c, suggesting that it is very short-lived ($t_{½}$ < 1 ms). Addition of > 100-molar excess H_2O_2 resulted in rapid bleaching of the Soret and visible bands, typical of heme degradation. However, H_2O_2-induced damage of cyt c was inhibited in the presence of CN^-, confirming that the cyt c/H_2O_2 reaction is ferric heme-mediated. The pH-rate profile of heme degradation by H_2O_2 revealed decreased heme bleaching at alkaline pH, indicating that alkaline form(s) of cyt c are more resistant to degradation, allowing them to continuously produce radical species via H_2O_2 turnover. Using ST/LC/MS with POBN as a spin trap, we were able to identify POBN-labeled tryptic peptides 73-79 and 74-79 in horse and cow cyts c and 28-39 in tuna cyt c from the cyt c/H_2O_2 reaction at pH 7.4, suggesting Tyr74 and Trp33 as likely sites of radical formation. Both proposed sites are surface exposed and could initiate intermolecular oxidation of nearby lipids and biomolecules. The biological significance of our findings remains to be defined but the rapid and specific reaction of cyt c with excess mitochondrial H_2O_2 to form exposed radicals may be a mechanism by which apoptosis is triggered.

5.2 Introduction

Apoptosis is a mechanism used by cells to control their numbers. It can be induced by changes in cellular redox potentials due to enhanced generation of reactive oxygen species, such as H_2O_2 (*32, 35*). Cyt c, which shuttles electrons from complex III to complex IV in mitochondrial electron transport, has been implicated in apoptosis (*23, 27*) and in oxidation of lipids and peptides (*30, 37*). For example, loss of molecular interaction between cyt c and cardiolipin, a mitochondrial-specific phospholipid, on peroxidation of the liposome has been observed and is proposed to be a primary event that triggers cyt c release from mitochondria in the apoptotic process (*140, 141*). Hence, the reaction of H_2O_2 with cyt c is of interest since the highly reactive Fe^{IV}=O and $X^{\bullet}$ species formed (eqn 5.1) could modulate cardiolipin peroxidation.

$$PFe^{III} + H_2O_2 \rightarrow X^{\bullet}Fe^{IV}=O + H_2O \qquad (5.1)$$

There is no direct spectroscopic evidence for the formation of Fe^{IV}=O in cyt c but there is evidence for $X^{\bullet}$ formation (*45, 77*). Reaction with excess H_2O_2 is accompanied by bleaching of the cyt c Soret band, as monitored by UV/Vis spectroscopy (*41, 42, 46, 142*). CN^- binds tightly to the Fe^{III} atom in cyt c by displacing the axial Met80 ligand and can be detected via the loss of an absorption band at 695 nm (*113*), which is associated with the Fe^{III}-S(Met80) bond (*1*). The addition of CN^- to the cyt c/cumene hydroperoxide reaction has been shown to prevent heme bleaching, suggesting that the hydroperoxide reacts with the heme Fe^{III} (*46*). Hence, a comparison of the reactivity of native and cyanocyts c from horse and tuna cyts c with H_2O_2 was carried out, and the

results presented here reveal that H_2O_2–mediated heme damage is also Fe-mediated. Furthermore, with the recent observation that changes in intracellular pH play a role in apoptosis (*25*), the pH dependence of the cyt c/H_2O_2 reaction was examined.

Detection of protein-bound $X^{\bullet}$ species is often difficult because they are short-lived and highly reactive; thus, spin traps are used to convert primary radicals to their more stable radical adducts. Spin-trapping of a tyrosyl radical generated in horse cyt c on reaction with H_2O_2 by MNP was detected by EPR by Barr and coworkers (*45*), indicating a tyrosine residue as a possible site for radical formation. Furthermore, using the spin trap DBNBS, peaks corresponding to $(DBNBS)_n$-cyt c adducts with n = 1-4 were observed in the MALDI-TOF mass spectrum by the same group (*45*), suggesting that as many as four $X^{\bullet}$ species were trapped by DBNBS during the reaction of horse cyt c with 5 molar equivalents of H_2O_2 (*37, 45*). However, the specific location(s) of $X^{\bullet}$ trapped by MNP and DBNBS on the cyt c polypeptide were not identified. We have previously used ST/LC/MS to identify radical sites formed in the reactions of H_2O_2 with Mb (*55, 56, 78*) and cytochrome c peroxidase (*79*). We reexamined the products of the horse cyt c/H_2O_2/spin trap reactions by ST/LC/MS using the four spin traps in Figure 5.1 to determine the extent and location(s) of protein-radical formation upon ferric heme-mediated peroxidation of the cyt c polypeptide. In addition, since horse and tuna cyts have similar NMR and crystal structures but differ by ~20% in sequence (*2, 104, 105, 109*), spin-trapping of $X^{\bullet}$ generated in the tuna cyt c/H_2O_2 reaction were also investigated to determine the effect of sequence on radical translocation. Our combined results suggest a possible mechanism for the triggering of apoptosis by cyt c.

a)

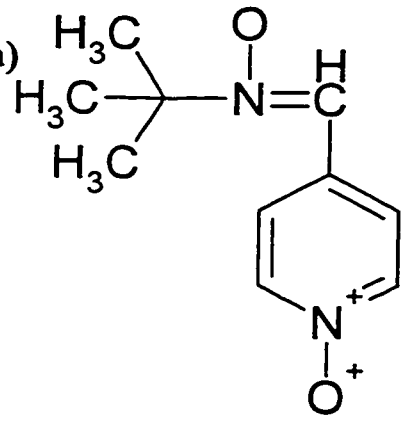

POBN (MW 194.24 Da)

b)

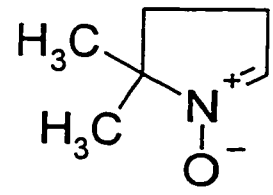

DMPO (MW 113.16 Da)

c)

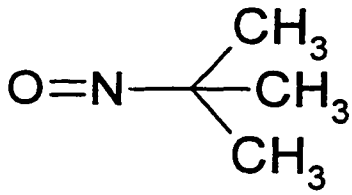

MNP (MW 87.12 Da)

d)

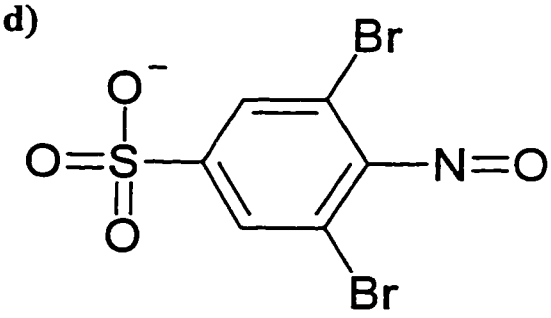

DBNBS (MW 343.96 Da)

Figure 5.1. Structures of (a) α-(4-Pyridyl-1-oxide)-N-t-butylnitrone (POBN), (b) 5,5-dimethylpyrroline-N-oxide (DMPO), (c) 2-methyl-2-nitroso propane (MNP) and (d) 3,5-dibromo-4-nitrosobenzenesulfonate (DBNBS) spin traps.

5.3 Experimental Procedures

5.3.1 Materials

Horse (Type VI), cow and tuna (Type XI) heart cytochromes c, TFA, DBNBS, MNP, DMPO and POBN were purchased from Sigma, and used without further purification. H_2O_2 was purchased from Fisher, while KCN was obtained from BDH Chemicals. Sequencing grade trypsin (Roche Molecular Biochemicals) was used for digestion and ammonium acetate and NaPi (Sigma) solutions containing 200 μM DTPA (ICN) were prepared using 18-MΩ-cm water obtained from a Barnstead Nanopure system.

5.3.2 UV/Vis Studies

Cyt c or cyanocyt c (10 μM) was reacted with 1-1000 molar equivalents of H_2O_2 in 50 mM NaPi buffer (pH 7.5) containing 200 μM DTPA. Spectra were acquired on a Beckman DU 650 spectrophotometer at a scan rate of 1200 nm/min replotted using Origin 3.0 software (MicroCal). For pH dependence studies, 10 μM cyt c was reacted with 1250 molar equivalents of H_2O_2 in 50 mM NaPi (pH 5.0 to 10.1) containing 200 μM DTPA. Stopped-flow experiments were carried out on an Applied Photophysics SX-18MV stopped-flow apparatus by rapidly mixing (1 ms) 2 μM cyt c with 22 μM H_2O_2 in 50 mM NaPi (pH 5.0 to 10.1) containing 200 μM DTPA. The pH of all solutions was measured before and after the reactions with H_2O_2.

5.3.3 Mass Spectrometry

Reactions of 500 μM cyt c with 10-50 mM spin trap and 5 molar equivalents of

H_2O_2 in 50 mM NaPi buffer (pH 7.5) containing 200 μM DTPA were terminated after 5 min by injecting the reactants onto a Vydac C_{18} column (4.6 x 300-mm). The protein was separated from buffer salts and low-molecular-weight reactants by HPLC (HP1090, Agilent Technologies) using a 10-55% ACN gradient in 0.05% TFA at 1 ml/min over 20 min. The protein peak was collected, lyophilized, suspended in 1:1 methanol/water with 0.5% acetic acid and infused at a flow rate of 5 μl/min using a syringe pump (Harvard Apparatus) into the ESI source of a Finnigan SSQ7000 mass spectrometer (ThermoFinnigan) for molecular weight determination. The mass-modified protein was digested with 1:50 (w/w) trypsin at 50°C for 4 h and the tryptic peptides were separated on a Vydac microbore C_{18} column (1 x 300 mm) using a 10-55% ACN gradient in 0.05% TFA at 40 μl/min over 100 min. For peptide mass mapping, the spray voltage and the heated capillary temperature of the ESI source were set at 4.5 kV and 210°C, respectively, while the sheath and auxiliary gas pressures were 40 and 15 psi, respectively. Full-scan acquisition was performed in centroid mode using scan rates of 320-380 amu/s.

5.4 Results and Discussion

5.4.1 UV/Vis Monitoring of the Ferricytochrome c/H_2O_2 Reaction

It has been postulated that a compound I-type species (eqn. 5.1) is formed in the reaction of H_2O_2 with horse cyt c (*30, 31, 37, 38*) and the species is linked to the oxidization of peptides (*37*), organic substrates (*38*) and lipid peroxidation (*30, 31*). Moreover, based on its ability to catalyze peroxidase-like reactions, cyt c has been used as a biocatalyst in the oxidation of thiophenes, organosulfides and aromatic compounds

(*143, 144*). However, no changes were reported in the Soret absorption following manual mixing (~ 2 s) of horse cyt c and H_2O_2 (*41, 42, 142*). Likewise, in the present work, addition of 1- to 1000-fold excess H_2O_2 to horse, cow and tuna cyts c did not result in the characteristic red-shift of the Soret band (Figure 5.2a-d) associated with Fe^{IV}=O heme formation (*47*). In fact, no Soret red-shift was observed following rapid mixing (1 ms) of 2 μM horse or tuna cyt c and 22 μM H_2O_2 in a stopped-flow apparatus at pH 5, 5.5, 8 and 10 (data not shown), revealing that any oxyferryl heme intermediates formed are very short-lived ($t_{½} < 1$ ms).

Addition of 1000-fold excess H_2O_2 to horse cyt c at pH 7.5 rapidly bleaches the Soret and visble absorption bands (Figure 5.2d), typical of heme degradation. The rate of cyt c heme degradation by H_2O_2 under pseudo-first-order conditions ($[H_2O_2] >> [\text{cyt c}]$), k_{obs} is given by:

$$k_{obs} = k_{app}[H_2O_2] \qquad (5.2)$$

where k_{obs} is the observed pseudo-first-order rate constant, k_{app} the apparent second-order rate constant. After ~ 20 min at pH 7.5, the Soret band of horse cyt c lost ~ 70% intensity (Figure 5.2d) with $k_{app} = 13.0\ min^{-1}$, which is in good agreement with the reported value of $7.6\ min^{-1}$ (*41*). Both tuna and cow cyts c were degraded to approximately the same extent by H_2O_2 (Figure 5.2e, f), with k_{app} values of 14.5 and 11.4 min^{-1}, respectively. Furthermore, like horse cyt c, there was no spectral evidence for Fe^{IV}=O heme formation in cow and tuna cyts c during their H_2O_2 reactions (Figure 5.2e, f). Consistent with the absence of an oxo ligand, 695-nm absorption, which is associated with an intact Fe^{III}-S(Met80) bond (Chapter

2), is observed during the ferric heme-mediated peroxidation of the three cyts c and is quenched only after ~ 40% heme destruction. Activation of H_2O_2 by cyt c likely involves binding to the Fe^{III} by displacing the Met80 ligand. Therefore, intramolecular transfer of two electrons from the polypeptide to the heme to form $X^{\bullet}$ species and regeneration of the Fe^{III}-S(Met80) bond must occur on the stopped-flow time scale. In contrast, autoreduction of the Fe^{IV}=O heme to an Fe^{III} heme in both horse Mb and cytochrome c peroxidase was found to occur at a considerably slower rate, with rate constants of 2.5 and 5 x 10^{-5} s^{-1}, respectively (*48*).

One could argue that an oxidized heme species does not occur in cyt c. For example, oxidation of the polypeptide could occur via hydrogen abstraction by $OH^{\bullet}$ formed in a Fenton-like reaction between H_2O_2 and free iron released during heme destruction (*40*). In fact, it was found that heme degradation in the cyt c/H_2O_2 reaction is directly proportional to the loss of iron from the protein (*42, 142*). However, Radi and coworkers (*30*) demonstrated that cyt c-catalyzed peroxidation of phosphatidylcholine liposomes by H_2O_2 was not inhibited by $OH^{\bullet}$ scavengers (benzoate and dimethylsulfoxide) nor by a metal chelator (DTPA), but was inhibited by CN^{-}. Furthermore, formation of horse cyanocyt c also prevented Soret bleaching (*46*) and radical production on cyt c (*45*) upon its reaction with organic hydroperoxides and H_2O_2, respectively. Likewise, we found that CN^{-} ligation inhibits H_2O_2-mediated heme damage since the addition of 1000-fold excess H_2O_2 to horse cyanocyt c resulted in no loss of Soret absorption (Figure 5.3a). Similarly, formation of cow and tuna cyanocyts c yields proteins resistant to H_2O_2-mediated heme damage (Figure 5.3b, c). Note, the absence of the 695-nm band in Figure 5.3 which confirms that the Fe^{III}-S(Met80) bond is broken in each of the cyts c.

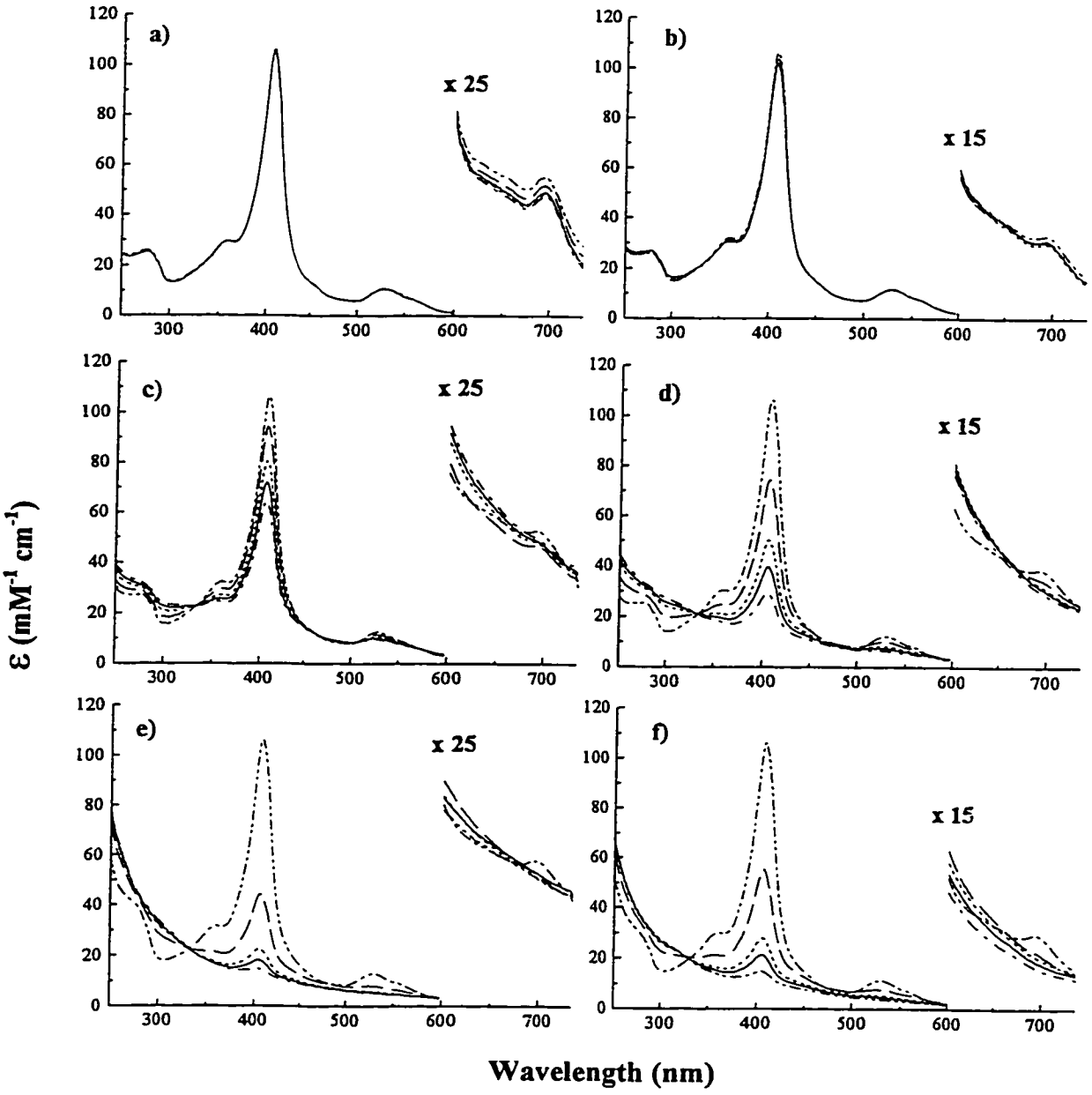

Figure 5.2. Absorption spectra of 10 μM horse cyt c plus (a) 10 μM, (b) 100 μM, (c) 1 mM and (d) 10 mM H_2O_2; and of (e) tuna and (f) cow cyts c plus 10 mM H_2O_2. The 0 (-··-), 3 (- -), 6 (···), 8 (—) and 10 (-·-·-) min spectra are shown. All spectra were recorded in 50 mM NaPi buffer (pH 7.5) containing 200 μM DTPA. Spectra were acquired on a Beckman DU 650 spectrophotometer at a scan rate of 1200 nm/min.

The membrane-bound form of cyt c, which resembles its alkaline isomer(s), was found to activate caspases in T hybridoma cells (*24*). Furthermore, Matsuyama and coworkers (*25*) observed that induction of apoptosis resulted in rapid mitochondrial alkalinization (from pH 7.8 to 8.5) and cytosolic acidification (from pH 7.4 to 7.0), followed by cyt c release, caspase activation, mitochondrial swelling and depolarization. These results indicate that changes in intracellular pH may be an early event that regulates caspase activation by cyt c during apoptosis. Thus, given the likely significance of the alkaline form(s) of cyt c in apoptosis (*23-25, 27, 32, 35, 140, 145*), the pH dependence of cyt c heme degradation by H_2O_2 was investigated. A plot of k_{obs} vs pH (Figure 5.4) reveals that the rate of heme degradation exhibits a maximum at pH 6.9 and 7.1 for horse and tuna cyts c, respectively. At the pKa (~ 9) of the alkaline isomerization of cyt c (*14*), the rate of cyt c heme degradation by H_2O_2 is ~ 25% that of the maximum, indicating that the alkaline isomer(s) are resistant to heme destruction compared to native cyt c (Figure 5.4). Interestingly, Nantes and coworkers (*146*) observed that incubating horse cyt c with mitochondrial mimetic phospatidylcholine/phosphatidylethanolamine/ cardiolipin liposomes, which convert cyt c to its membrane-bound form that resembles the alkaline isomer(s), slowed down heme bleaching by H_2O_2, indicating an improved stability. Of note, the generation of $X^{\bullet}$ species on cyt c was found to be necessary for heme destruction (*42*).

5.4.2 Trapping Protein-based Radicals Formed in the Cytochrome c/H_2O_2 Reaction.

Following the reaction of horse cyt c with 5 molar equivalents of H_2O_2 in the presence of MNP and DMPO, the deconvolved ESI mass spectra revealed ions with

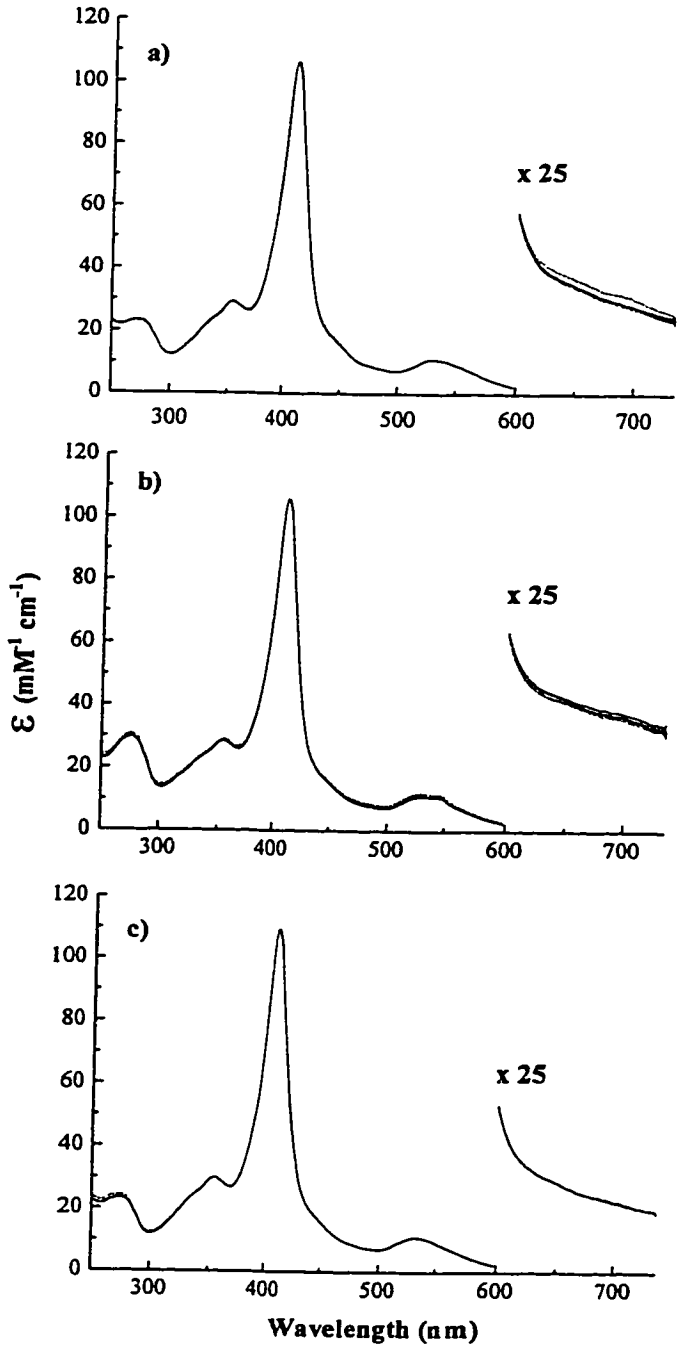

Figure 5.3. Absorption spectra of 10 μM (a) horse, (b) tuna and (c) cow cyts c plus 3 mM KCN recorded 20 min after the addition of 10 mM H_2O_2. Note the absence of 695-nm absorption in 25x spectra compared to those in Figure 5.2. Experimental conditions are given in Figure 5.2.

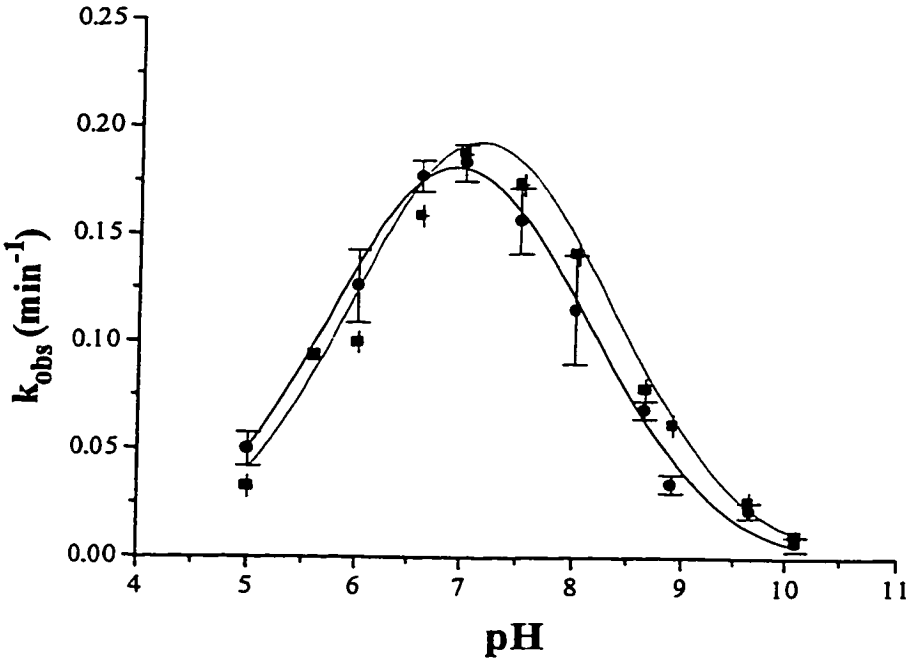

Figure 5.4. Observed pseudo-first-order rate constants (k_{obs}) vs pH for heme degradation in 10 μM horse (• —) and tuna (■ ---) cyts c by 12 mM H_2O_2. All spectra were recorded in 50 mM NaPi (pH 5.0 to 10.1) containing 200 μM DTPA. Spectra were acquired on a Beckman DU 650 spectrophotometer at a scan rate of 1200 nm/min.

increased masses of 102 and 113 Da over untreated cyt c (Figure 5.5), corresponding to the addition of one oxidized MNP and one DMPO molecule, respectively (*44*). Only native horse cyt c ions (*m/z* 12 360) were detected in the absence of either H_2O_2 or the spin trap (data not shown). The yield of both MNP- and DMPO-labeled cyt c was ~ 15% based on the relative intensities of the cyt c peaks in the deconvolved mass spectra (Figure 5.5). A similar yield (10-20%) was found for DBNBS-labeling by optical difference spectroscopy (*77*) and EPR (*45*) measurements, which should be sufficient to detect labeled peptides that are stable to peptide mass mapping. However, peptide mass maps of the cyt c/H_2O_2/MNP (1:5:40) or cyt c/H_2O_2/DMPO (1:5:100) reaction products resulted in exclusively native horse cyt c tryptic peptides (data not shown), indicating that the adducts are unstable under the peptide mass mapping conditions. Previously (*78*), it was found necessary to reduce MNP spin adducts with ascorbate to form diamagnetic mass adducts, which in turn were stable to the peptide mass mapping conditions. However, following addition of 5 mM ascorbate to the 5-min reaction of cyt c/H_2O_2/spin trap, even the undigested MNP- or DMPO-cyt c adducts were no longer detected by MS (data not shown).

Peaks corresponding to $(DBNBS)_n$-cyt c adducts with n = 1-4 were observed by MALDI-TOF, suggesting that as many as four $X^{\bullet}$ species were trapped by DBNBS during the reaction of cyt c with 5 molar equivalents of H_2O_2 (*37, 45*). We repeated these experiments, hoping that the reported increased trapping efficiency of DBNBS would yield adducts stable to peptide mass mapping, but again the peptide mass maps revealed exclusively native horse cyt c tryptic peptides (*44, 77,*). Further investigations revealed

that noncovalent adduct formation, and not increased trapping efficiency, gives rise to the high yield of DBNBS mass adducts as discussed in detail in Chapter 6.

Recently, Anni and Israel (*147*) observed that POBN inhibited ^{14}C incorporation into cyt c by 20% in the cyt c/H_2O_2/[1-^{14}C]ethanol reaction. Furthermore, $(POBN)_2$-cyt c spin adducts were detected by EPR in the absence of ethanol (*147*), and were assigned to adducts of the previously reported tyrosine and tryptophan radicals (*45*). Based on these positive spin-trapping results, POBN was next selected as a spin-trapping agent. The deconvolved ESI mass spectra of cow (Figure 5.6a), tuna (Figure 5.6b) and horse (data not shown) cyts c from cyt c/H_2O_2/POBN (1:5:100) reactions revealed an increased mass of 136 Da over untreated cyt c (*44*), which was not observed in the absence of H_2O_2 (data not shown). This Δm corresponds to the mass of one POBN molecule (194 Da) minus 58 Da, which is likely due to loss of the *t*-butyl group (57 Da) from POBN, as reported previously for MNP in the lignin peroxidase/H_2O_2/MNP reaction (*148*). The trapping efficiency of POBN was ~ 10% as estimated from the relative intensities of the molecular-ion peaks in the deconvolved mass spectra (Figure 5.6). Despite the poor trapping efficiency, peptide mass mapping of the horse cyt c/H_2O_2/POBN reaction products yielded modified peptides (Figure 5.7a), that were not observed in the extracted-ion chromatograms (XIC) of the tryptic digest of native horse cyt c (Figure 5.7b). Peptide 73-79 (∅, KYIPGTK) and peptide 74-79 (⊗, YIPGTK) were found to have an increased mass of 136 Da based on the doubly charged ions observed at *m/z* 406.2 and 470 in the XIC in Figure 5.7a. These results suggest POBN-labeling of Tyr74, and the same modified peptides were observed for cow cyt c, which differs in sequence from horse cyt c by only three amino acids. Following our proposal that Tyr74 is a site of spin

trapping in horse and cow cyts c (*44*). Deterding and coworkers (*50*) reported DBNBS-labeling of peptide 74-79 in the horse cyt c/H_2O_2/DBNBS reaction based on their MALDI-TOF mass spectral data, and also proposed that Tyr74 was the most likely site of radical formation.

Peptide mass mapping of the tuna cyt c/H_2O_2/POBN reaction products (Figure 5.7c) did not yield POBN-modified tryptic peptides 73-79 and 74-79. Instead, a doubly charged ion at *m/z* 749 corresponding to peptide 28-39 (⊕, VGPNLWGLFGRK) plus 152 Da, was observed for tuna cyt c. The increase in mass observed for the trapped tuna cyt c peptide compared to the trapped horse or cow cyt c peptides (152 vs 136 Da) indicates oxidation of the spin adduct (*72, 73*) or one of the peptide residues during peptide mass mapping. The former is more likely since peptide 28-39 was unlabeled and unoxidized in the peptide mass map of native tuna cyt c, as can be deduced from the XIC (Figure 5.7d).

Trp33 is proposed as the POBN-modification site in peptide 28-39 based on its favorable reduction potential (E° $Trp^{\bullet}$/TrpH = 1.05 V) compared to other residues present in the peptide [e.g., glycine (E° $Gly^{\bullet}$/GlyH = 1.22 V) or phenylalanine (E° $Phe^{\bullet}$/PheH = 1.6 – 1.9 V] (*57, 149*). The POBN-modification sites in the cyts c need to be confirmed by tandem MS sequencing of the POBN-modified peptides. Nonetheless, detection of different POBN-modified peptides between horse (or cow) and tuna cyts c, which share ~ 80% sequence identity (*16*), suggests that amino acid sequence dictates the sites of radical formation.

5.5 Conclusions

Heme intermediates generated in the reaction between cyt c and H_2O_2 are not

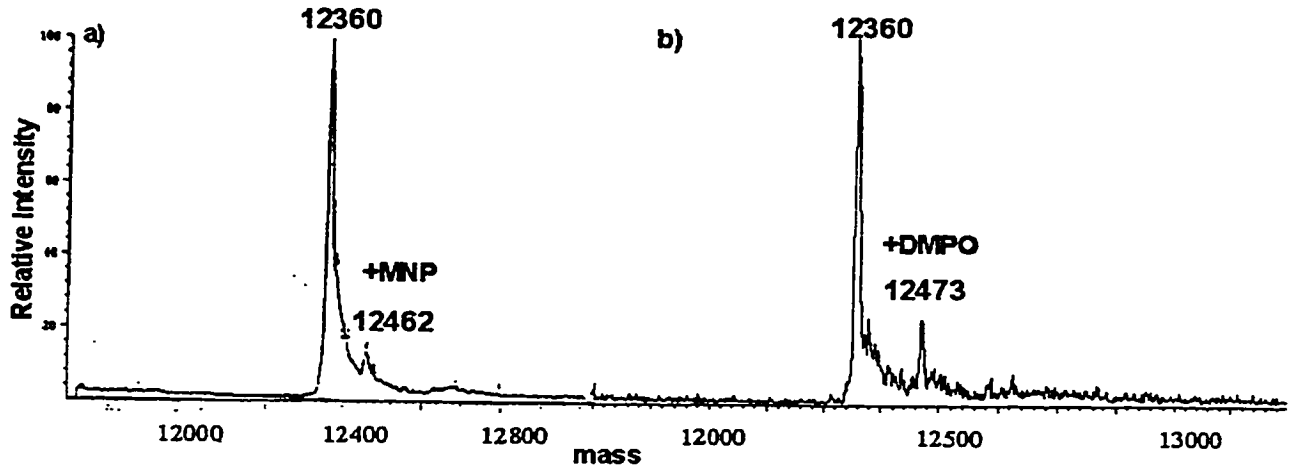

Figure 5.5. Deconvolved ESI mass spectra of the products of a 10-min reaction of 500 μM horse cyt c with 2.5 mM H_2O_2 in the presence of (a) 20 mM MNP and (b) 50 mM DMPO. Reactions were carried out in 50 mM ammonium acetate buffer (pH 7.5) containing 200 μM DTPA. The HPLC purified reaction products (See Experimental Procedures) were collected, lyophilized and suspended in 1:1 methanol/water with 0.5% acetic acid. Samples (~ 1 mg/ml) were directly infused into the ESI source of the mass spectrometer at 5 μl/min for molecular weight determination. The spray voltage and the heated capillary temperature of the ESI source were set at 4.5 kV and 210°C, respectively, while the sheath and auxiliary gas pressures were 40 and 15 psi, respectively. Full-scan acquisition was performed in centroid mode using scan rates of 320-380 amu/s.

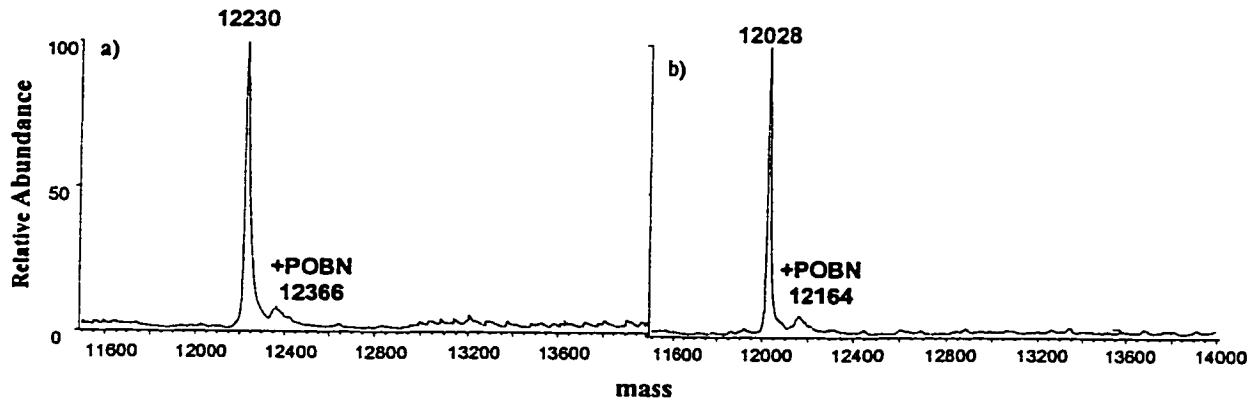

Figure 5.6. Deconvolved ESI mass spectra of the products of a 10-min reaction of 500 μM (a) cow and (b) tuna cyts c with 2.5 mM H_2O_2 in the presence of 50 mM POBN. Experimental conditions are given in Figure 5.5.

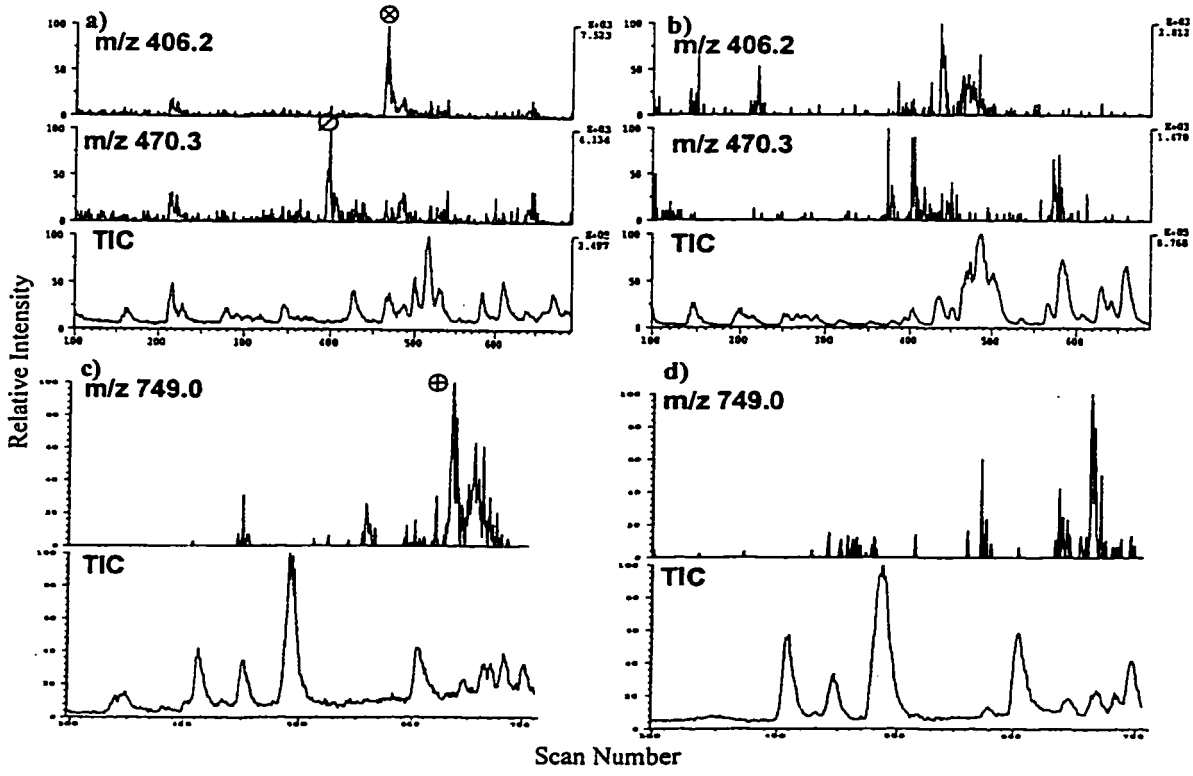

Figure 5.7. Peptide mass maps and extracted-ion chromatograms of (a) POBN-modified horse, (b) native horse, (c) POBN-modified tuna and (d) native tuna cyts c. The trapping reaction was carried as indicated in Figure 5.6. The derivatized cyt c was digested with 1:50 (w/w) trypsin at 50°C for 4 h, and the digests were separated for peptide mass mapping by LC/MS on a microbore C_{18} column (1-x 300 mm) with a 10-55% CH_3CN gradient in 0.05% TFA at 40 µl/min over 100 min. ESI conditions are given in Figure 5.5.

detectable on the stopped-flow time scale. Nonetheless, CN^- inhibition of heme bleaching is consistent with ferric heme-mediated activation of H_2O_2. Spin trapping of protein-based radicals by POBN in the cyt c/H_2O_2 reaction suggests that residues act as endogenous donors to the Fe^V=O heme intermediate formed on H_2O_2 turnover. No derivatized peptides were found in the mass maps of digests containing 10-20% cyt c-labeled with MNP, DBNBS or DMPO but were found following POBN-labeling (~ 10%) of cyt c. This suggests that the MNP-, DBNBS- and DMPO-trapped species in cyt c are unstable to peptide mass mapping, which is somewhat surprising given that stable mass adducts using MNP and DBNBS were observed in peptide mass maps of Mb (see Chapter 7). To confirm that the cyt c adducts are indeed unstable to peptide mass mapping, labeled cyt c should be isolated from the large amount of unlabeled protein and digested separately. This would prevent any labeled peptides from going undetected in a large excess of peptides from the unlabeled protein.

It is of interest to note the poor trapping efficiencies at pH 7.5 of cyt c radicals (~ 10-20%) relative to those generated in Mb (~ 25-80%; Chapter 7). Tyr67, which is adjacent to the heme (3.27 Å) and is in fact believed to be involved in the electron-transfer pathway between cyt c and its biological partners (*1*), is likely an effective endogenous donor to the heme in cyt c analogous to Tyr103 in Mb. However, unlike Tyr103, which is highly solvent-exposed, Tyr67 is buried underneath Tyr74 and is unlikely accessible to the bulky spin traps in the neutral form of cyt c. It has been observed that Tyr67 is selectively nitrated by peroxynitrite (*150*), which is significantly less bulky than the spin traps. Nonetheless, radical translocation to Tyr74 in the mammalian cyts c and Trp33 in tuna cyt c was inferred, and given that these residues are

highly solvent exposed, their radical forms are likely the cause of the protein and membrane damage (*30, 31, 37*) observed in cyt c-catalyzed peroxidation. Consequently, radical generation on these exposed residues may also play a role in triggering apoptosis (*140, 141*).

6.0 Mass Spectral Analysis of Protein-based Radicals Using DBNBS: Non Radical Adduct Formation vs Spin Trapping

6.1 Abstract

Protein-based radicals generated in the reaction of cyt c with H_2O_2 were investigated by ESI-MS using DBNBS. Up to four DBNBS-cyt c adducts were observed in the mass spectra. However, by varying the reaction conditions (0-5 molar equivalents of H_2O_2 and substituting cyt c with its cyanide adduct which is resistant to peroxidation) noncovalent DBNBS adduct formation was inferred. Nonetheless, optical difference spectra revealed the presence of a small fraction of covalently trapped DBNBS. To probe the nature of the noncovalent DBNBS adducts, the less basic proteins, Mb and α-lactalbumin, were substituted for cyt c in the cyt c/H_2O_2/DBNBS reaction. A maximum of two DBNBS adducts were observed in the mass spectra of the products of the Mb/H_2O_2/DBNBS reactions, whereas no adducts were detected following α-lactalbumin/H_2O_2/DBNBS incubation, which is consistent with adduct formation via spin trapping only. Titration with DBNBS at pH 2.0 yielded noncovalent DBNBS-cyt c adducts and induced folding of acid-denatured cyt c, as monitored by ESI-MS and optical spectroscopy, respectively. Thus, the noncovalent DBNBS-cyt c mass adducts observed are assigned to ion-pair formation occurring between the negatively charged sulfonate group on DBNBS and positively charged surface residues on cyt c. The results reveal the pitfalls inherent in using mass spectral data with negatively charged spin traps such as DBNBS to identify sites of radical formation on basic proteins such as cyt c.

6.2 Introduction

Reactive oxygen species, such as H_2O_2 and superoxide, are generated by all aerobic cells as byproducts of a number of metabolic reactions and in response to various stimuli. Oxidative damage can occur when H_2O_2 reacts with heme proteins, such as cyt c, to form highly reactive oxyferryl-heme and transient $X^{\bullet}$ species that are linked to the initiation of lipid peroxidation (*30, 31*). Detection of $X^{\bullet}$ in biological systems is often difficult because they are short-lived and highly reactive. Spin traps, which are diamagnetic compounds containing a functional group that reacts with $X^{\bullet}$ to form $XST^{\bullet}$, are frequently used in EPR investigations (*72*). Although EPR signals can provide information about a radical center and its environment, the *specific sites* of radical formation in biomolecules are not identified. LC/MS has been used to identify spin adducts of various small molecules (*74-76*). Our research group has extended the use of LC/MS of spin adducts to proteins to overcome the inherent limitations of EPR. We have found that conversion of the spin adduct $XST^{\bullet}$ to a stable XMA via ascorbate reduction permits the assignment of XMA to a *specific amino acid residue* using ST/LC/MS (*44, 56, 78, 79*). In addition to the increased specificity offered by ST/LC/MS, it possesses enhanced sensitivity over EPR, since considerably smaller quantities (picomole vs nanomole) of sample can be analyzed (*45*).

DBNBS, sometimes referred to as Perkin's trap, was developed to trap carbon-centered radicals. It is stable to temperature and light, and the introduction of the sulfonate group onto the benzene ring has helped overcome problems encountered in the use of lipophilic nitroso spin traps such as MNP (*151*). However, it is known that DBNBS adducts can be formed through several nonradical reactions. For example,

prolonged incubation of DBNBS with unsaturated fatty acids (*152*) or with free tryptophan (*82*) causes chemical modifications through nonradical reactions such as the ene reaction between the nitroso group in DBNBS and the double bond in tryptophan.

Barr and coworkers (*37, 45*) recently reported the trapping of a protein-based tyrosyl radical by DBNBS in the reaction of cyt c with H_2O_2 using EPR. In addition, peaks corresponding to $(DBNBS)_n$-cyt c adducts with n = 1-4 were observed by MALDI-MS, suggesting that as many as four protein-based $X^{\bullet}$ species were trapped by DBNBS during the reaction of cyt c with 5 molar equivalents of H_2O_2. However, the sites of DBNBS-cyt c adduct formation were not identified. The radicals formed in the reaction of cyt c with H_2O_2 are of interest, since they could cause mitochondrial membrane damage and play a role in the apoptotic process (*141*). Using ST/LC/MS, we reexamined the products of the cyt c/H_2O_2/DBNBS reaction to determine the extent of protein radical formation. Surprisingly, we detected DBNBS-cyt c mass adducts in the absence of H_2O_2, and in the cyanide-ligated protein, even though cyanide binding inhibits heme-mediated peroxidation (*45, 113*).

Cyt c, a highly basic protein (pI 10), unfolds at low pH, resulting in increased absorption and blue-shifting of the Soret maximum from 408 at pH 7.0 to 394 nm in the acid-denatured protein at pH 2.0 (*153*). The addition of anions converts the unfolded state of cyt c to a conformation resembling the molten-globule by reducing the electrostatic repulsion of positive charges on the protein surface via Debye-Hückel screening and ion-pairing (*153, 154*). We provide data here that support the formation of noncovalent adducts under the MS conditions (pH 2.0); in fact, DBNBS was found to stabilize a molten globule state of acid-unfolded cyt c at pH 2.0 in a manner similar to

that reported for 8-anilino-1-naphthalenesulfonate (ANS) (*154*). Our results reveal that caution must be used in interpretation of the mass spectra of DBNBS-protein adducts and the different limitations in EPR and MS approaches to the analysis of spin-trapped species are also highlighted.

6.3 Experimental Procedures

6.3.1 Materials

Horse (Type VI), cow and tuna (Type XI) heart cyts c, horse heart Mb, α-lactalbumin from cow milk, TFA and DBNBS were purchased from Sigma, and used without further purification. H_2O_2 was purchased from Fisher, while KCN was obtained from BDH Chemicals. Sequencing grade trypsin (Roche Molecular Biochemicals) was used for digestion and ammonium acetate (JT Baker Chemical Co.) containing 200 μM DTPA (ICN) were prepared using 18-MΩ-cm water obtained from a Barnstead Nanopure system.

6.3.2 Methods

Reactions were carried out by mixing 500 μM protein with 10 mM DBNBS and 0, 1 or 5 molar equivalents of H_2O_2 in 50 mM ammonium acetate (pH 7.5) containing 200 μM DTPA. The reactions were terminated after 10 min by injecting the reactants onto a Vydac C_{18} column (4.6 x 300-mm), and separating the protein from salts and low-molecular-weight reactants by HPLC (HP1090, Agilent Technologies) using a 10-55% ACN gradient in 0.05% TFA at 1 ml/min over 20 min. The protein peak was collected, lyophilized, suspended in 1:1 methanol/water with 0.5% acetic acid and infused at a flow

rate of 5 µl/min using a syringe pump (Harvard Apparatus) directly into the ESI source of a Finnigan SSQ7000 mass spectrometer (ThermoFinnigan) for molecular weight determination. The protein was further digested with 1:50 (w/w) trypsin at 50°C for 4 h. The digests were separated for peptide mass mapping on a Vydac microbore C_{18} column (1 x 300 mm) using a 10-55% ACN gradient in 0.05% TFA at 40 µl/min over 100 min. The spray voltage was set at 4.5 kV and the capillary temperature was maintained at 210°C, while the sheath and auxiliary gas pressures were 40 and 15 psi, respectively. Full-scan acquisition was performed in profile mode using scan rates of 320-380 amu/s.

To probe DBNBS interaction with acid-unfolded cyt c, the protein was incubated for 30 min with increasing amounts of DBNBS in 0.05% TFA (pH 2.0) before carrying out optical or MS measurements. For molecular weight determination, samples were infused into the ESI source of the mass spectrometer by flow injection at 50 µl/min using a 75% ACN (0.05% TFA) isocratic elution. Optical spectra were recorded on a Beckman DU 650 spectrophotometer between 200-600 nm, using a scan rate of 2400 nm/min. Difference spectra were generated using Origin 3.0 software (MicroCal).

6.4 Results and Discussion

6.4.1 Analysis of DBNBS Mass Adduct Formation with Ferricytochrome c in the Presence and Absence of H_2O_2

The deconvolved ESI mass spectrum (Figure 6.1a) of horse cyt c revealed that $(DBNBS)_n$-cyt c adducts (n = 1-4) are formed in the reaction of cyt c with 5-fold molar excess of H_2O_2, as observed previously by MALDI-MS (*37, 45*). A similar pattern of $(DBNBS)_n$-cyt c adduct formation was observed when cyt c was reacted with only 1

molar equivalent of H_2O_2 (Figure 6.1b) despite the fact that H_2O_2, a two-electron oxidant, can remove a maximum of two electrons to generate two radical sites on cyt c. The reaction of horse cyt c with 1-5 molar equivalents of H_2O_2 was repeated several times in the presence of DBNBS and multiple DBNBS adducts were consistently observed. Moreover, in the absence of H_2O_2, up to two DBNBS adducts were detected not only with horse cyt c, but also with cow and tuna cyts c (Figures 6.1c-e). These data suggest that DBNBS interacts with cyt c via a non-spin-trapping mechanism.

CN^- serves as a high-affinity ligand for the ferric state of cyt c by displacing the axial Met80 ligand (*113, 155*). Hence, cyanocyt c, which inhibits heme-catalyzed reactions and prevents cyt c heme degradation by organic hydroperoxides (*45, 113*), was used to probe direct (i.e., non-heme-mediated) peroxidation of the polypeptide. Figure 6.1f reveals that the addition of 3 mM KCN to the horse cyt c/H_2O_2/DBNBS reaction results in the same mass spectrum as that observed in the absence of H_2O_2 (Figure 6.1f vs c). Therefore, the $(DBNBS)_n$-cyt c adducts from the cyanocyt c/H_2O_2/DBNBS reaction are unlikely due to peroxidation, supporting the absence of non-heme-mediated oxidation of cyt c residues by H_2O_2. Nonetheless, the mass spectra reveal that the $(DBNBS)_n$-cyt c adduct intensities increase in the presence of H_2O_2 (Figures 6.1a, b vs c); hence, spin trapping of $X^\bullet$ by DBNBS is also likely occurring, consistent with the EPR data that indicated trapping of a tyrosyl radical in cyt c (*45*).

To further probe the nature of the DBNBS adducts detected by MS, optical spectra of the reaction products obtained for horse cyt c in the absence and presence of H_2O_2 were recorded (Figure 6.2). The difference spectrum (Figure 6.2, trace 3) of HPLC-purified products from the cyt c/H_2O_2/DBNBS (1:5:20) reaction minus those from

the cyt c/H_2O_2 (1:5) reaction reveals loss of DBNBS absorption seen at 288 nm (Figure 6.2, trace 2) and growth of a new absorption band at 300 nm. This is consistent with increased conjugation of the chromophore, where the nitroso group of DBNBS traps a radical on the aromatic ring of a tyrosine residue (*45*). The possibility that the 300-nm absorption was due to H_2O_2-induced oxidation of DBNBS was also considered, but incubation of DBNBS with 5 molar equivalents of H_2O_2 gave rise to a DBNBS species with an absorption spectrum (Figure 6.2, trace 1) identical to that of untreated DBNBS (Figure 6.2, trace 2). Moreover, the cyt c/DBNBS (1:10) minus cyt c difference spectrum (data not shown) resembles that of DBNBS alone (Figure 6.2, trace 2). As an additional control, the cyt c/H_2O_2 (1:5) minus cyt c difference spectrum (Figure 6.2, trace 4) was generated. A relatively flat baseline between 230 and 370 nm with negligible UV absorption was observed, suggesting minimal oxidation of aromatic residues by H_2O_2. Thus, the new band at 300 nm in the cyt c/H_2O_2/DBNBS minus cyt c/H_2O_2 difference spectrum (Figure 6.2, trace 3) is not an artifact due to the subtraction procedure, but can be assigned to a protein-based DBNBS spin adduct. Unfortunately, tryptic digestion of the products of the cyt c/H_2O_2/DBNBS reaction yielded only native peptides. It has been observed that ascorbate reduction of MNP-Mb spin adducts yields stable XMAs that can be identified by ST/LC/MS (*56, 78*). However, addition of 5 mM ascorbate to the cyt c/H_2O_2/DBNBS reaction did not convert XST$^{\bullet}$ to XMA, since the mass spectrum (data not shown) was the same as that in Figure 6.1a. This is likely due to either the low trapping efficiency of DBNBS towards cyt c radicals or instability of the covalently trapped DBNBS-cyt c adduct under the digestion conditions. The radical is directly bonded to the nitroxide in the XST$^{\bullet}$ formed with DBNBS, which renders reverse or

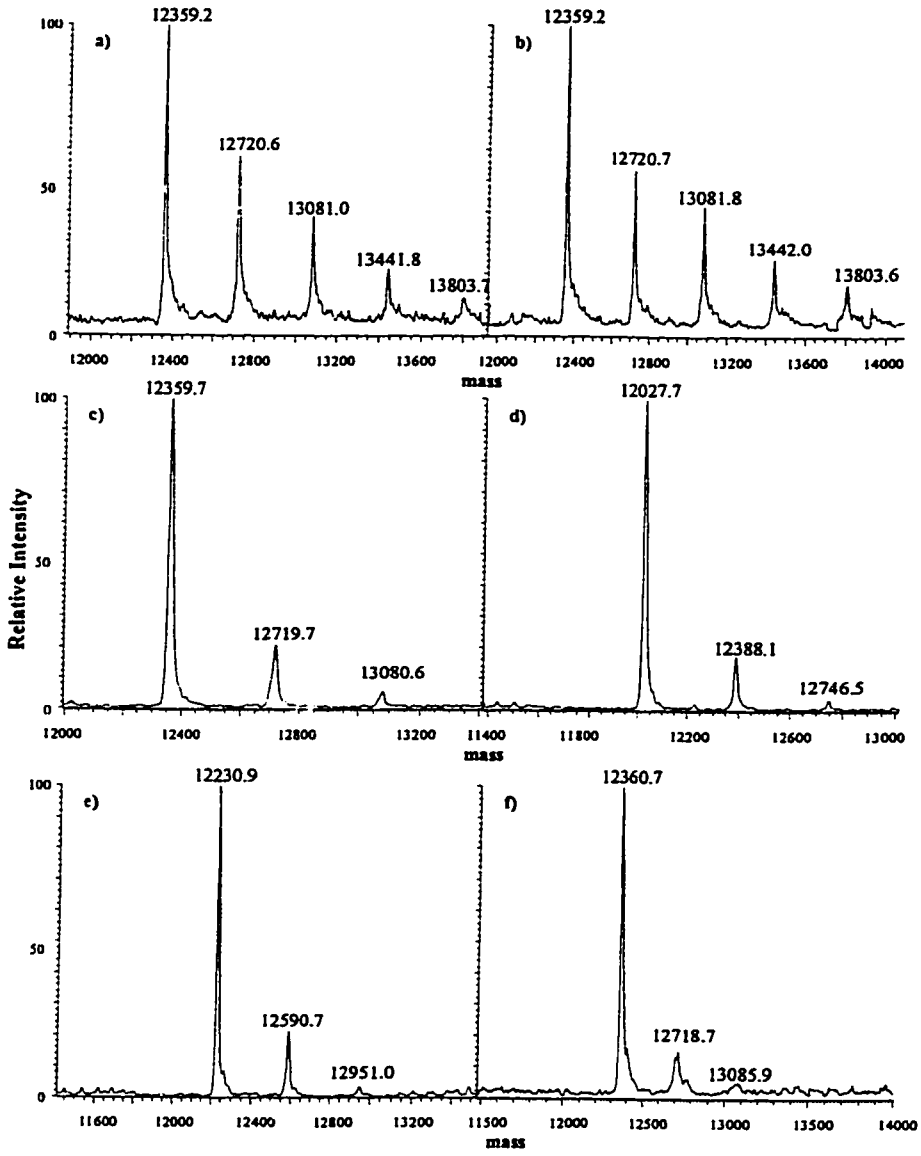

Figure 6.1. Deconvolved ESI mass spectra of the products of a 10-min reaction of 500 μM cyt c with H_2O_2 in the presence of 10 mM DBNBS. (a) Horse cyt c with 2.5 mM H_2O_2; (b) horse cyt c with 500 μM H_2O_2; (c) horse cyt c without H_2O_2; (d) tuna cyt c without H_2O_2; (e) cow cyt c without H_2O_2; (f) horse cyt c with 2.5 mM H_2O_2 and 3 mM KCN (to form cyanocyt c). Reactions were carried out in 50 mM ammonium acetate (pH 7.5) containing 200 μM DTPA. The HPLC purified reaction products (see "Experimental Procedures") were collected, lyophilized and suspended in 1:1 methanol/water with 0.5% acetic acid. Samples (~ 1 mg/ml) were directly infused into the ESI source of the mass spectrometer at 5 μl/min for molecular weight determination.

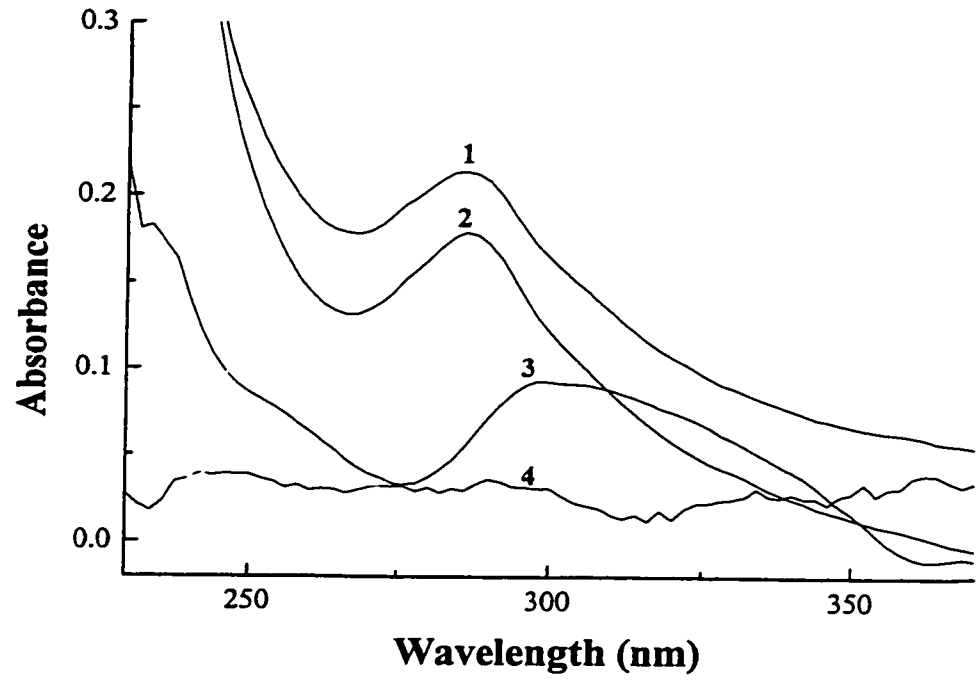

Figure 6.2. Absorption spectra of 132 μM DBNBS following a 10-min incubation with 660 μM H_2O_2 (trace 1) and untreated 111 μM DBNBS (trace 2). Difference optical spectra of the HPLC-purified DBNBS-cyt c adduct (~ 11 μM cyt c) minus the products from the 10-min reaction of 11 μM horse cyt c with 55 μM H_2O_2 (trace 3), and 11 μM horse cyt c following a 10-min incubation with 55 μM H_2O_2 minus 11 μM horse cyt c (trace 4). All solutions were prepared in 50 mM ammonium acetate (pH 7.5) containing 200 μM DTPA. Spectra were recorded at a scan rate of 2400 nm/min and difference spectra were generated using Origin 3.0 software.

cleavage reactions of the spin-trapped species favorable (*72*). Interestingly, Kim and coworkers (*156*) observed by EPR that the decay of DMPO adducts of Mb and hemoglobin were accelerated by denaturation (urea or guanidine-HCl) and proteolysis of the protein moiety. The data in Figure 6.2 demonstrate, nonetheless, that DBNBS-cyt c spin adducts formed in the presence of H_2O_2 can be distinguished from those formed in the absence of H_2O_2 by optical difference spectroscopy.

Many reactions other than spin trapping have been reported for DBNBS. For example, the formation of a nitroxyl free radical was detected by EPR after a 60-min incubation of DBNBS with free tryptophan (*82*). Chemical modification after 24-h incubation of low-density lipoprotein by DBNBS was detected by agarose-gel electrophoretic mobility (*152*). The DBNBS labeling was assigned to the ene reaction between the nitroso group and a double bond, which results in an allylic hydroxylamine (*157*). However, both reported studies indicated that labeling required prolonged ($\geq$ 1 h) exposure to DBNBS. We limited cyt c exposure to DBNBS to 10 min and immediately separated the protein from the low-molecular-weight reactants by HPLC.

The possibility of "inverted spin trapping" was also considered, which could occur if the cyt c/H_2O_2/DBNBS reaction yielded an oxidized form of the spin trap ($DBNBS^{\bullet+}$). Inverted spin trapping of $DBNBS^{\bullet+}$ by an amino acid residue could lead to a DBNBS-cyt c adduct identical to that formed by "normal" spin trapping of $X^{\bullet}$ by DBNBS [reviewed in (*73*)]. Horseradish peroxidase/H_2O_2 (E° Fe^{IV}=O/Fe^{III} = 0.94 V) catalyzed the oxidation of DBNBS over a 24-h incubation, as seen by EPR (*158*). However, $DBNBS^{\bullet+}$ generation was not observed by the peroxidase activity (E° Fe^{IV}=O/Fe^{III} ~ 1 V) of Mb/H_2O_2 or cyt c oxidase/H_2O_2 (*159, 160*), the Fenton reaction,

Fe^{II}/H_2O_2 (E° Fe^{III}/Fe^{II} = 0.77 V) (*161*), nor in the oxidation of selenite by Ce^{IV} (E° Ce^{IV}/Ce^{III} = 1.44 V) (*162*). Since MNP and DBNBS contain identical redox-active nitroso functional groups, it can be assumed that the E° $DBNBS^{\bullet+}$/DBNBS is comparable with E° $MNP^{\bullet+}$/MNP (E° = 2.06 V) (*73*), which is beyond the reach of the high-oxidation states of the above systems under non-forcing conditions. Hence, "inverted spin trapping" is ruled out in the cyt c/H_2O_2/DBNBS reaction since (i) the reaction time was only 10 min and (ii) the Fe^{IV}=O center is rapidly converted to Fe^{III} by endogenous electron transfer to heme (data not shown). Also, the reduction potential of the Fe^{III}/Fe^{II} couple in horse cyt c (E° = 0.25 V) is clearly insufficient to oxidize the nitroso group.

DBNBS could also form a sulfonamide with the ε-amino group of lysines, which account for ~ 20% of the residues in cyt c. However, the deconvolved mass spectra (Figures 6.1a-f) reveal Δm increments of 360 ± 2 Da for the cyt c adducts, corresponding to ammoniated DBNBS adducts, whereas sulfonamide formation would give rise to Δm increments of 326 Da. Furthermore, peptide mass mapping of the products of the cyt c/H_2O_2/DBNBS reaction yielded exclusively native horse cyt c peptides (data not shown), indicating that no stable derivatives such as sulfonamides were formed. These results agree with those of Kalyanaraman and coworkers (*152*) who reported that DBNBS-modified low-density lipoprotein was formed by a lysine-independent process.

6.4.2 Analysis of DBNBS Mass Adduct Formation with Metmyoglobin and α-lactalbumin in the Presence and Absence of H_2O_2

To establish whether or not DBNBS adduct formation with proteins exhibits specificity, Mb and α-lactalbumin were selected for further MS investigations. Mb, a

heme-containing protein with a pI of 7.0, does not have a high affinity for anionic compounds (*163*). Spin-trapping of $X^{\bullet}$ generated in the Mb/H_2O_2 reaction has been demonstrated by both EPR and ST/LC/MS using DBNBS and other spin traps and $X^{\bullet}$ has been assigned primarily to Tyr103 (*55, 59, 60, 62, 78*). The difference spectrum (data not shown) of HPLC-purified products from the Mb/H_2O_2/DBNBS (1:5:20) reaction minus those from the Mb/H_2O_2 (1:5) is similar to that seen with cyt c (Figure 6.2, trace 3), which is indicative of DBNBS-tyrosine spin adduct formation in both proteins. An estimate of ε_{302} for the DBNBS-tyrosine spin adduct (42 mM^{-1} cm^{-1}) was obtained by assuming a trapping efficiency of 70% for the tyrosyl radical in Mb, based on the relative intensities of the peaks in the mass spectrum of the Mb/H_2O_2/DBNBS (1:5:20) reaction products (Figure 6.3a). Using this estimated ε_{302}, the yield of DBNBS-cyt c spin-adduct formation in the cyt c/H_2O_2/DBNBS (1:5:20) reaction is ~ 20%, compared to ~ 10% estimated from EPR measurements (*45*). Yields of 10-20% are sufficient to identify modified peptides by mass mapping, but tryptic digests of DBNBS-labeled cyt c contained exclusively native peptides, indicating that DBNBS-labeling is not stable to peptide mass mapping, as discussed above.

In Figure 6.3a, the deconvolved mass spectrum of the Mb/H_2O_2/DBNBS (1:5:20) reaction products shows the formation of $(DBNBS)_n$-Mb adducts with n = 1 and 2. DBNBS ene addition to Mb and/or ion-pair formation can be ruled out since only native globin is detected in the deconvolved mass spectrum in the absence of H_2O_2 (Figure 6.3b). Inverted spin trapping was not reported in the Mb/H_2O_2/DBNBS reaction (*160*), since the oxidized heme of Mb (E° $Fe^{IV}=O/Fe^{III}$ ~ 1 V) cannot oxidize DBNBS. When H_2O_2 was present at 1 molar equivalent (Figure 6.3c), the relative intensity of the

$(DBNBS)_2$-Mb peak was negligible and that of the (DBNBS)-Mb peak decreased by 40% compared to the 1:1-adduct following oxidation with 5 molar equivalents of H_2O_2 (Figure 6.3a). Likewise, a less intense (DMPO)-Mb peak was observed by ESI-MS upon decreasing the amount of H_2O_2 from 3 to 1 molar equivalents in the Mb/H_2O_2/DMPO reaction (*59*). It was reported that formation of oxyferryl Mb requires > 1 molar equivalent of H_2O_2, since H_2O_2 is consumed in side reactions at the porphyrin or other locations on the globin (*56, 164*). Nevertheless, the efficiency of $(XST^{\bullet})_n$-Mb adduct formation depends on the number of oxidizing equivalents in the Mb/H_2O_2/ST reaction for both DMPO and DBNBS, in contrast to the cyt c/H_2O_2/DBNBS reaction (Figure 6.1a vs b).

DBNBS adduct formation with α-lactalbumin was also investigated here, since it is an acidic protein with a pI ~ 4 and contains basic residues evenly dispersed over its surface. In fact, due to its high negative charge under the experimental conditions used (pH 7.5), α-lactalbumin should repel the negatively charged DBNBS. Similarly, Matulis and coworkers (*165*) observed by fluorescence spectroscopy that very little ANS bound to bovine serum albumin (pI 5.8) at pH > 11. α-lactalbumin also lacks the heme prosthetic group found in Mb and cyt c; thus there should be no reaction with H_2O_2 to generate $X^{\bullet}$ unless H_2O_2 directly oxidizes the polypeptide. As expected, the deconvolved mass spectra of α-lactalbumin both in the presence (Figure 6.4a) and absence (Figure 6.4b) of H_2O_2 revealed no DBNBS adduct formation, since only native α-lactalbumin was detected. This rules out direct peroxidation of the polypeptide consistent with the results for cyanocyt c (Figure 6.2f) and also rules out ion-pair formation.

6.4.3 DBNBS Adduct Formation with Horse Cyt c in the Absence of H_2O_2 at pH 2.0

Anion-dependent stabilization of compact structures that resemble the molten globule state have been observed by monitoring the Soret band upon incubation of cyt c with ANS or with various strong acids and their neutral salts (*153, 154*). The molten globule state of cyt c, which forms at high salt (500 mM NaCl) and low pH (pH 2.0), is characterized by a red-shift from 394 nm (the Soret maximum of acid-denatured cyt c) to 400 nm, which is accompanied by band broadening (*153*). To elucidate the mechanism by which the $(DBNBS)_n$-cyt c mass adducts (Figure 6.1) are formed, acid-unfolded horse cyt c was titrated with DBNBS at pH 2.0, and changes in the Soret and mass spectra were monitored. The Soret maximum red-shifted from 394 to 402 nm following 30-min incubation of cyt c with 25 molar excess DBNBS, consistent with molten globule formation (Figure 6.5a). Similar effects were observed with ANS (*154*), which promotes the refolding of cyt c at low pH by Debye-Hückel screening and ion-pair formation (*153*). The mass spectra in Figures 6.1a, b vs c reveal enhanced binding of DBNBS to the H_2O_2-oxidzied cyt c, which is also seen in the greater red-shifting of the Soret bands in Figure 6.5b vs a. Of note, the absorbancies of the acid denatured oxidized cyt c (ε_{394} = 140 mM^{-1} cm^{-1}) and its DBNBS-stabilized molten globule (ε_{402} = 94 mM^{-1} cm^{-1}) are less than those of the unoxidized forms (ε_{394} = 209 mM^{-1} cm^{-1}; ε_{394} = 120 mM^{-1} cm^{-1}).

DBNBS titration of horse cyt c was also monitored by MS (Figure 6.6). The $(DBNBS)_n$-cyt c (n = 1-4) peaks in the mass spectra of samples with ≥ 10-fold excess DBNBS recorded without prior HPLC purification are more intense than the corresponding peaks in the HPLC-purified sample (Figure 6.6c-f vs Figure 6.1c). Figure 6.6 also reveals that the abundance and stoichiometry of the $(DBNBS)_n$-cyt c adducts

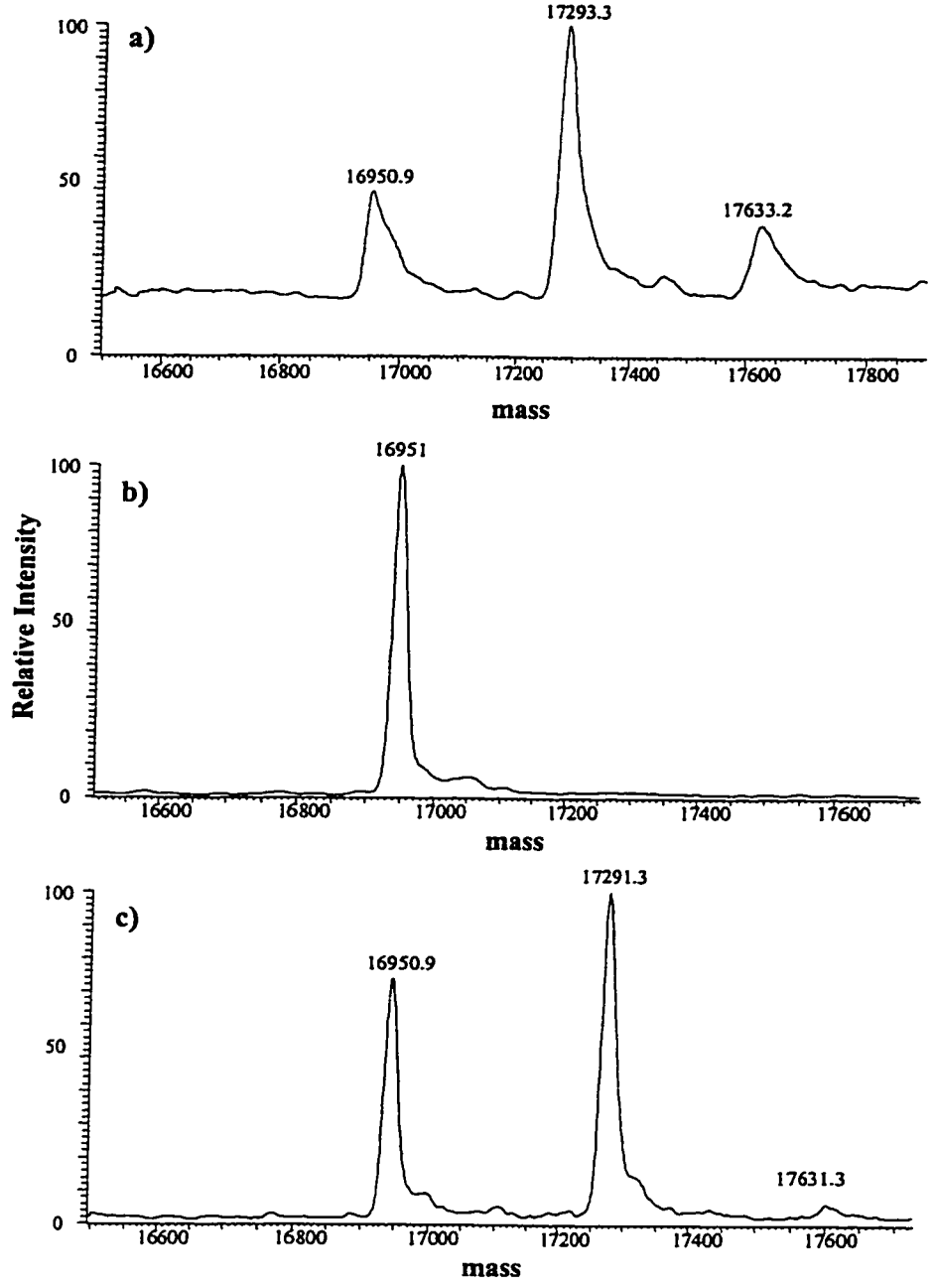

Figure 6.3. Deconvolved ESI mass spectra of the products of a 10-min reaction of 500 μM horse heart metmyoglobin with H_2O_2 in the presence of 10 mM DBNBS: with 2.5 mM H_2O_2 (a); without H_2O_2 (b); and with 500 μM H_2O_2 (c). Experimental conditions are given in the legend to Figure 6.1.

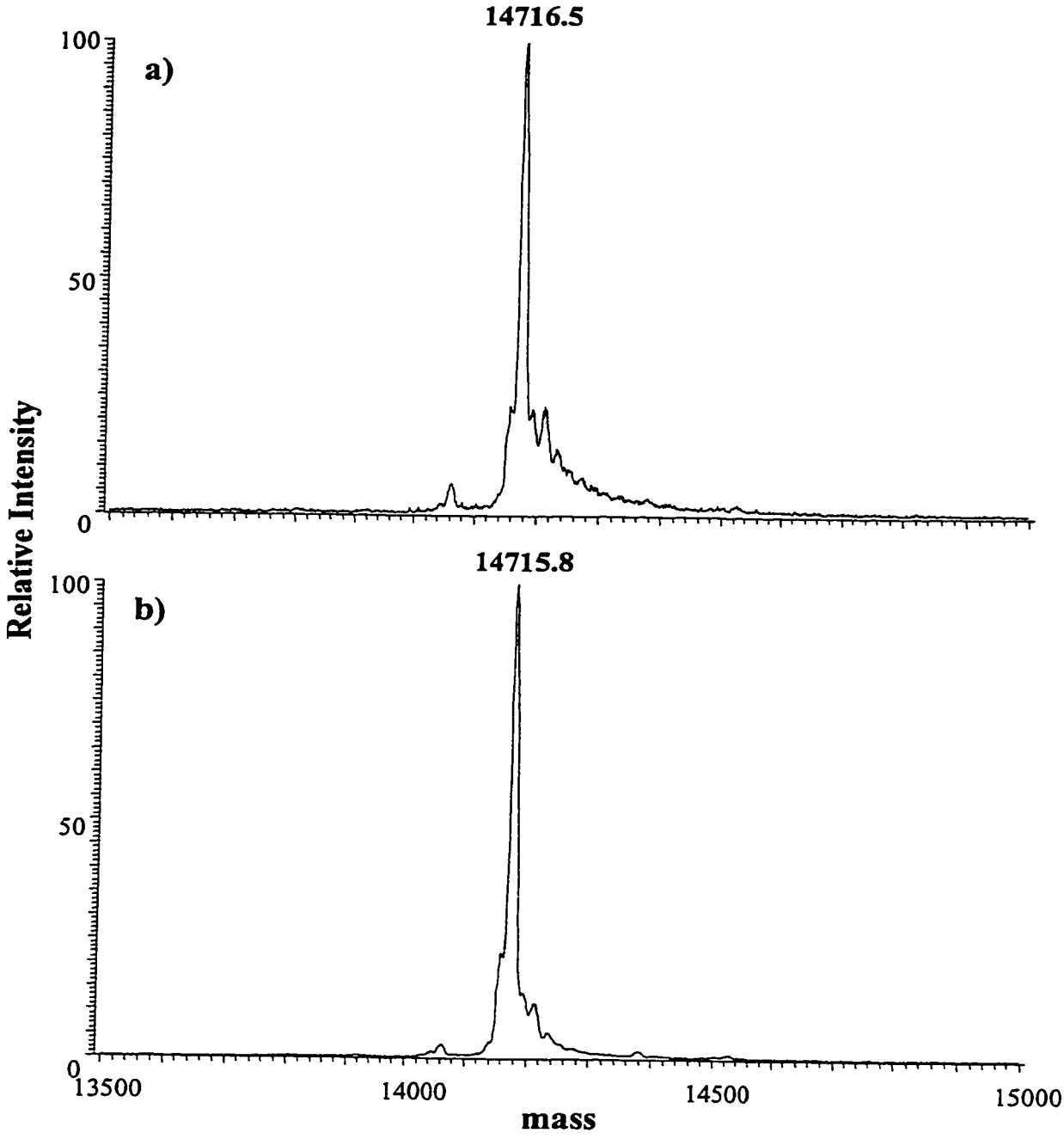

Figure 6.4. Deconvolved ESI mass spectra of the products of a 10-min reaction of 500 μM α-lactalbumin with H_2O_2 and 10 mM DBNBS: with 2.5 mM H_2O_2 (a); and without H_2O_2 (b). Experimental conditions are given in the legend to Figure 6.1.

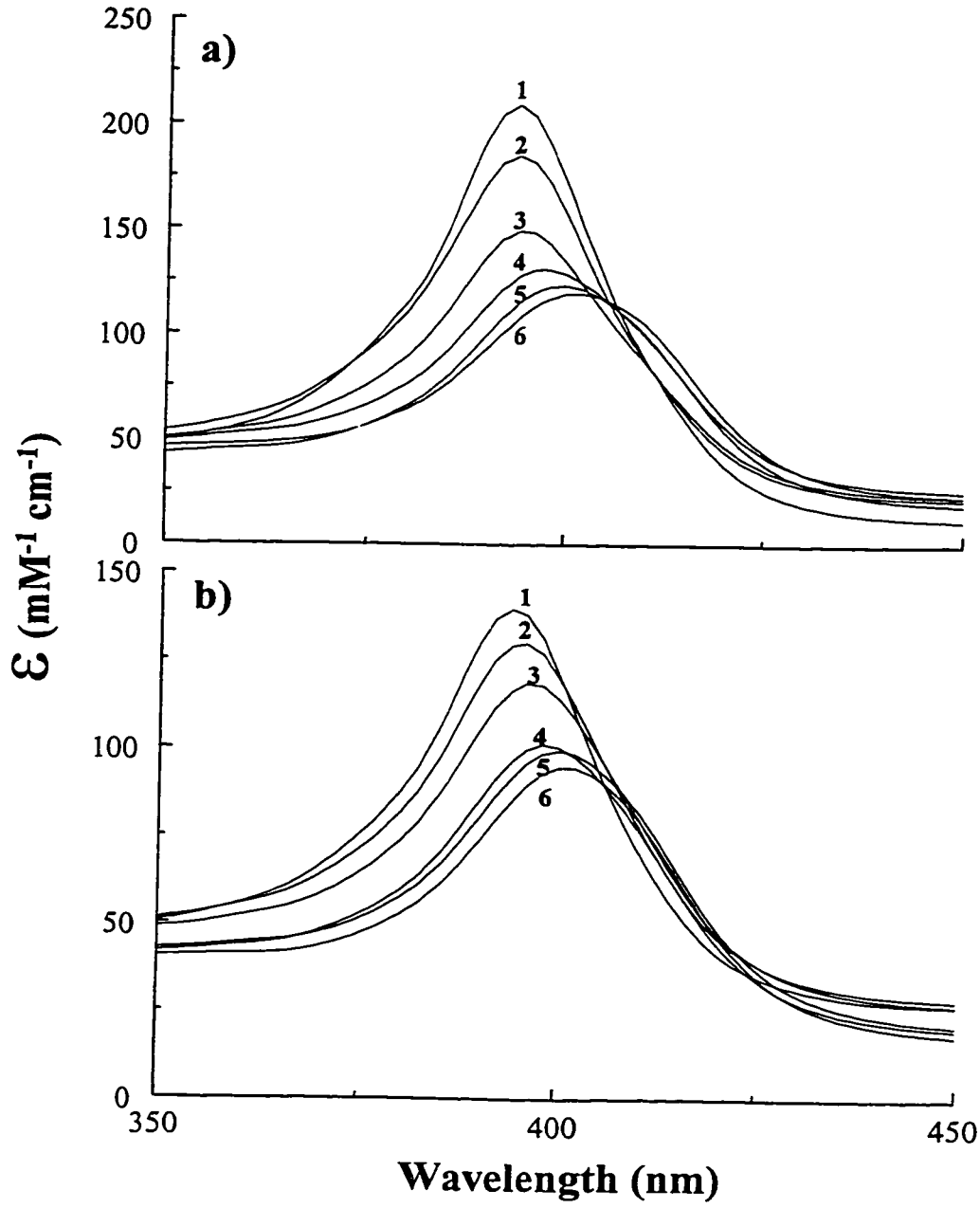

Figure 6.5. Soret absorption spectra of 10 μM non-oxidized (a) and oxidized (b) horse cyt c incubated for 30 min in 0.05% TFA (pH 2.0) in the presence of 0 (trace 1), 1 (trace 2), 5 (trace 3), 15 (trace 4), 20 (trace 5) and 25 (trace 6) molar equivalents of DBNBS. Oxidized protein was prepared by treating 100 μM horse cyt c with 5 molar equivalents of H_2O_2 for 5 min at pH 7.5. Spectra were recorded at a scan rate of 2400 nm/min.

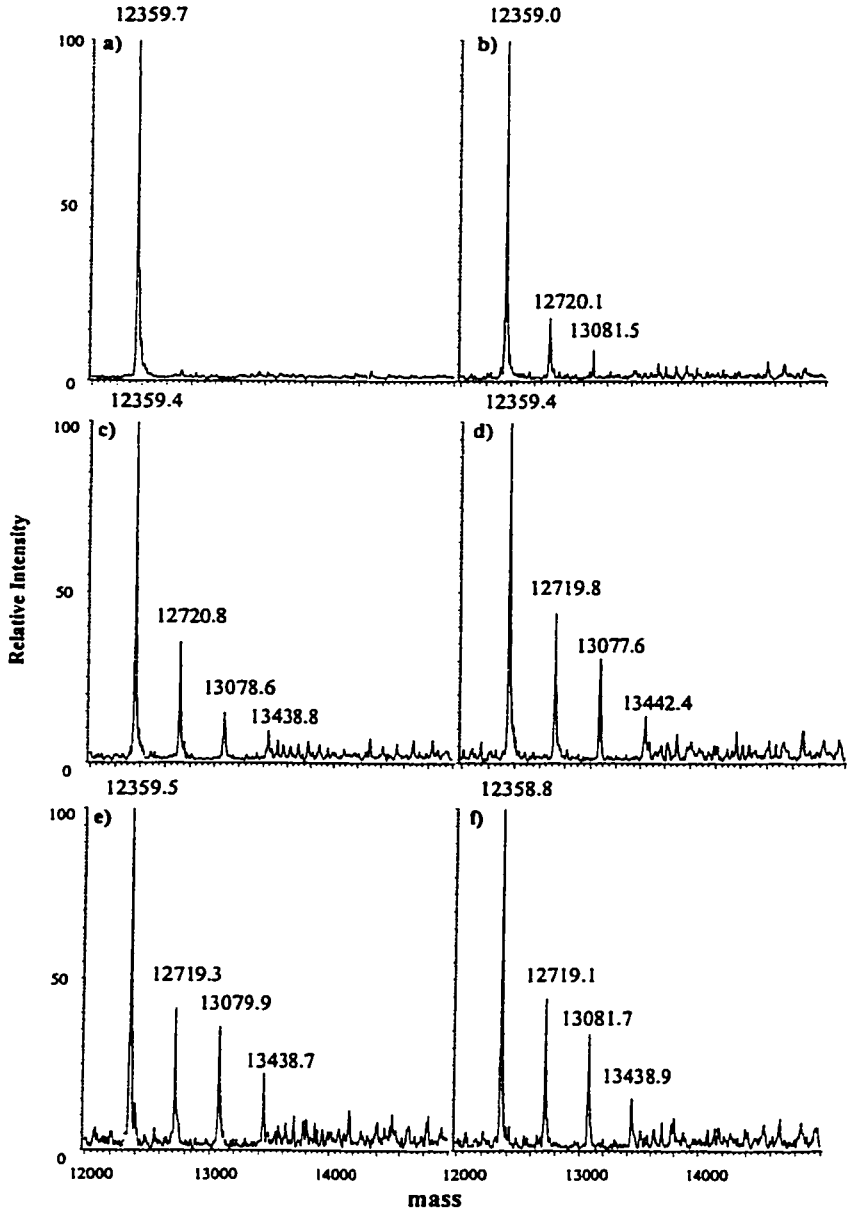

Figure 6.6. Deconvolved ESI mass spectra of 20 μM horse cyt c incubated for 30 min in 0.05% TFA (pH 2.0) in the presence of 0 (a), 1 (b), 10 (c), 15 (d), 20 (e) and 25 (f) molar equivalents of DBNBS. Samples in 75% ACN containing 0.05% TFA were infused into the ESI source of the mass spectrometer by flow injection at 50 μl/min.

increased as a function of DBNBS concentration, which is consistent with noncovalent adduct formation. Ali and coworkers observed peaks corresponding to $(ANS)_n$-cyt c adducts (n = 1-7) at pH 2.0 by ESI-MS, but no adduct formation was observed with nile red, a neutral hydrophobic dye (*153*), revealing the importance of electrostatic interactions.

Precipitation of cyt c was also observed upon addition of a large excess of DBNBS at pH 7.5, which required limiting the amount of DBNBS added to 500 μM cyt c to 10 mM. Ion-pair formation between the sulfonate group of DBNBS and basic residues of cyt c would reduce the solubility of the protein. Interestingly, cyt c is known to possess anionic binding sites; specifically, there are two phosphate binding sites, one near Lys87 with a dissociation constant (K_d) of 200 μM and another close to Lys25-His26-Lys27 with a K_d of > 2 mM (*1*). However, the DBNBS-cyt c adducts must possess K_d values in the low μM range, since phosphate-cyt c adducts are not observed by ESI-MS following reversed-phase HPLC purification, whereas DBNBS-cyt c adducts are seen in Figure 6.1c-e. In fact, a K_d of ~ 36 μM was estimated from a double reciprocal plot (ΔAbs^{-1} vs $[DBNBS]^{-1}$) of the data in Figure 6.5 for both oxidized and non-oxidized horse cyt c, similar to the calculated K_d (3-50 μM) for the interaction of ANS to cationic polyamino acids at pH 2.0 (*165*).

6.5 Conclusions

DBNBS complexes with cyt c via strong electrostatic interactions at pH 2.0, thereby complicating the analysis of spin trapping by ST/LC/MS. However, noncovalent DBNBS adduct formation clearly shows specificity for cyt c (Figures 6.1c-e vs 6.3b and

6.4b), indicating that its formation can not simply be correlated with the total number lysine residues, since horse cyt c possesses 19, while horse Mb and cow α-lactalbumin have 19 and 12, respectively. Lysine residues are highly conserved in cyts c and are clustered predominately around the exposed heme edge, forming anionic binding sites (*1*). In Mb and α-lactalbumin, the lysine residues are more or less distributed evenly over the entire protein surface. Also, the fact that DBNBS and ANS exhibit comparable efficiencies in inducing cyt c folding at low pH, despite the significantly larger hydrophobic moiety of ANS, is consistent with electrostatic interactions being the principal determinant of binding. Ion-pair formation between proteins and negatively charged probes such as DBNBS and ANS may be a common occurrence at the low pHs used for ESI-MS analyses in positive-ion mode. Therefore, it is essential to carry out the appropriate controls before interpreting MS data involving protein-probe adducts such as the $(DBNBS)_n$-cyt c adducts obtained in the present study. Finally, our results reveal that compared to Tyr103 of Mb, the cyt c radicals are not very reactive and/or accessible at pH 7.5.

7.0 A Mass Spectrometric Investigation of Protein-based Radicals Formed in the Metmyoglobin/H_2O_2 Reaction using DBNBS

7.1 Abstract

The high trapping efficiency of DBNBS and its ease of handling make it an ideal spin trap to use in ST/LC/MS studies of the Mb/H_2O_2 reaction. Approximately 80% of Mb was labeled with reduced DBNBS (R-DBNBS) when the protein was reacted with 5 molar equivalents of H_2O_2. This represents a 3-fold increase in labeling over that found in our previous studies using MNP (*78*). Furthermore, the pH dependence of DBNBS labeling revealed increased trapping of a second radical site in the Mb/H_2O_2 reaction at pH 5.0 vs 7.5, since $(DBNBS)_2$-Mb adducts dominate the low-pH mass spectrum. This is consistent with the observed pro-oxidative activity of Mb under acidic conditions, such as that found at inflammation and ischemic sites (*5, 6*). Peptide mass mapping of the R-DBNBS-Mb adducts from the pH 7.5 and 5.0 reactions by MALDI-TOF and LC/ESI-MS yielded DBNBS-labeled peptides, 24-45, 97-118 and 103-118, which were not observed in the tryptic digest of native Mb. Sequencing of peptide 97-118 identified Tyr103 as a site of radical formation, and the difference absorption spectrum of the Mb/H_2O_2/DBNBS reaction products was also consistent with DBNBS-tyrosine adduct formation. Analysis of electron-transfer pathways revealed that Tyr103, Lys42/45 and His 64 should be more efficient electron donors to the heme than other residues in the protein.

7.2 Introduction

Mb is a 17-kDa heme protein whose normal function is storage of oxygen in muscle tissues. Mb also possesses pro-oxidant properties, since lipid and protein oxidation can result from the reaction of H_2O_2 with Mb (*166-169*). The Mb/H_2O_2 reaction (eqn. 7.1) involves two-electron oxidation of the protein to form Fe^{IV}=O and an unstable $X^{\bullet}$,

$$XFe^{III} + H_2O_2 \rightarrow X^{\bullet}Fe^{IV}=O + H_2O \qquad (7.1)$$

the identity of which has been the subject of speculation for over 50 years. Peroxide reactions are considered contributory factors in myocardial reperfusion injuries after a period of ischemia (*53, 54*). Recently, Slezak and coworkers (*51*) demonstrated that H_2O_2 was produced upon addition of oxygen-containing perfusate to a rat ischemic heart and hypervalent states of Mb were detected in isolated ischemic-reperfused rat hearts (*52*). These results support the hypothesis that the excess H_2O_2 produced during reperfusion can react readily with Mb (which is present at mM concentrations in cardiac myocytes) to form highly reactive intermediates (*51-54, 166-169*).

Both the $X^{\bullet}$ species formed in reaction 7.1 and their DBNBS, MNP and DMPO spin adducts have been detected by EPR (*58, 59, 61, 62, 160*). The EPR signals were tentatively assigned to tryptophanyl-derived peroxyl and tyrosyl radicals at residues 14 and 103, respectively. The assignment of EPR signals to specific protein residues is ambiguous but the *specific sites* of radical formation in biomolecules can be identified by ST/LC/MS. Recently, using ST/LC/MS analysis of ascorbate-reduced MNP-Mb adducts,

our group confirmed spin-adduct formation on Tyr103 and identified Lys42, as a second, less abundant, site of MNP-labeling at pH 7.4. No MNP adduct was found trapped on Trp14 (*78*), but His64 was MNP-labeled at pH 5.0. This is consistent with the observation of different EPR and UV/Vis spectra at neutral and acidic pHs (*170*), and suggests that the location of $X^{\bullet}$ varies with pH.

To establish whether the radical sites identified by ST/LC/MS are independent of the spin trap used, the Mb/H_2O_2 reaction was reinvestigated using DBNBS. Given its high solubility in buffers at neutral pH, DBNBS is a suitable trap for studies under physiological conditions. Therefore, it is desirable to characterize its spin-trapping efficiency and the stability of the resultant adducts, with and without ascorbate reduction, to peptide mass mapping under typical ST/LC/MS conditions. Furthermore, to understand the role of Mb in catalyzing H_2O_2-mediated cellular damage, the effects of pH on the $X^{\bullet}$ species trapped in the Mb/H_2O_2 reaction were also studied. Interestingly, the pro-oxidative activity of Mb has been demonstrated under acidic conditions (pH 5.0), such as those found at inflammation and ischemic sites (*53, 54*).

7.3 Experimental Procedures

7.3.1 Materials

Horse heart metmyoglobin, TFA and DBNBS were purchased from Sigma and used without further purification. H_2O_2 was purchased from Fisher. Sequencing-grade trypsin (Roche Molecular Biochemicals) was used for digestion, and ammonium acetate (JT Baker Chemical Co.) solutions containing 200 μM DTPA (ICN) were prepared using water (18-MΩ-cm) obtained from a Barnstead Nanopure system.

7.3.2 Spin Trapping

Reactions were carried out between pH 5.00-8.65 in 50 mM ammonium acetate containing 200 μM DTPA by mixing 500 μM protein with 0-10 molar equivalents of H_2O_2 in the presence of 10 mM DBNBS for 5 min. Samples were also incubated with 5 mM ascorbate for 30 min to reduce the spin adducts to more stable spin-paired species (*78*). The protein products were separated from salts and low-molecular-weight reactants by HPLC (HP1090, Agilent Technologies) on a Vydac C_{18} column (4.6 x 250-mm) with a 10-55% ACN gradient in 0.05% TFA at 1 ml/min over 20 min. Post-column splitting (1:50) allowed 40 μl/min of effluent to be directed to the ESI source of a Finnigan SSQ7000 mass spectrometer (ThermoFinnigan) for molecular-weight determination of the samples of interest. Mass spectra were acquired in positive-ion mode with full-scan acquisition performed in profile and centroid modes using a scan rate of 460 amu/s. The spray needle voltage was set at 4.5 kV with a capillary temperature of 210°C. The sheath and auxillary gas flow rates were 40 psi and 15 ml/min, respectively.

Absorption spectra were recorded on a Beckman DU 650 spectrophotometer between 200-600 nm using a scan rate of 2400 nm/min. Difference spectra were generated using Origin 3.0 software (MicroCal).

7.3.3 Peptide Mass Mapping

The DBNBS-modified Mb was digested with trypsin (1:50 w/w) in ammonium acetate (pH 7.5) for 16 h at 25°C. The resulting tryptic peptides were separated on a Vydac microbore C_{18} column (1 x 250 mm) using a 5-55% ACN gradient in 0.05% TFA

at 40 μl/min over 120 min and directly analyzed by ESI-MS using the MS conditions described in the previous section. Peptide mass mapping was also performed on a Bruker Bioflex III MALDI-TOF mass spectrometer. A 1:1 mixture (1 μl) of tryptic digest with a saturated solution of α-cyano-4-hydroxycinnamic acid in 45:45:10 ethanol:water:formic acid was spotted onto the MALDI target and co-crystalization was allowed to proceed at room temperature. A nitrogen laser at 337 nm was used to desorb/ionize the sample, and data from 300 laser shots were averaged using the software provided on the instrument, exported as ASCII files and replotted using Origin 3.0 software for analysis.

7.3.4 Peptide Sequencing

Sequencing of modified peptides was performed by LC/MS/MS using a Micromass Quattro mass spectrometer following LC (Waters Alliance) separation of the tryptic peptides on a Phenomonex Luna C_{18} column (50 x 4.6 mm) using a 5-50% ACN gradient in 0.1% TFA at 1 ml/min over 20 min. Post-column splitting (1:5) allowed 200 μl to be directed the ESI source. MS/MS spectra were acquired in positive-ion mode at scan rate of 1280 amu/s using a sheath gas flow of 100 l/h. The spray needle, cone, and collision energy voltages were set at 3000, 30 and 25 V, respectively, while the source block and desolvation temperatures were 100 and 350°C, respectively.

7.3.5 Analysis of Electron-transfer Pathways in Mb

Electron-transfer pathways from amino acid residues to heme in Mb were determined using HARLEM software, which is derived from Rasmol and Gaussian 94™, and written by Igor V. Kurnikov, University of Pittsburgh. Inquiries pertaining to the use

of this software should be directed to his thesis supervisor, David N. Beratan, at Beratan@pitt.edu.

7.4 Results and Discussion

7.4.1 DBNBS Mass Adduct Formation in the Mb/H_2O_2/DBNBS Reaction

Previously, our research group used the spin trap MNP to identify the *specific sites* of radical formation in the Mb/H_2O_2 reaction by ST/LC/MS (*78*). To establish whether the radical sites identified are independent of the spin trap used, MNP was substituted by DBNBS in the Mb/H_2O_2 reaction. When Mb was reacted with 5 molar equivalents of H_2O_2 in the presence of DBNBS at pH 7.5 (Figure 7.1a), two DBNBS-Mb mass adducts were observed at ~ 343 and 686 Da higher than the Mb molecular ion (16950 Da), suggesting trapping at two sites on the polypeptide. From the relative areas of the peaks in Figures 7.1a, 70% of Mb is DBNBS-labeled, with 20% doubly-labeled. This represents ~ 300% and 50% increase in DBNBS-labeling compared to MNP (*78*) and DMPO (*59*), respectively, which may reflect the effective spin trap concentrations present in aqueous solutions. For example, spin trapping by the MNP monomer has to compete with monomer-dimer equilibrium, as well as thermal and photo-induced decomposition (*72, 80*). Spin trapping by DMPO must compete with its oxidation to DMPOX (5,5-dimethyl-2-ketopyrrolidone-*N*-oxyl), which is ineffective as a spin-trapping agent (*59, 61, 171*). DBNBS is less sensitive to light and heat than either MNP or DMPO, and although it gives rise to a dimeric form, the monomer-dimer equilibrium favors the monomer (*80*), rendering DBNBS an efficient radical scavenger.

It was established in our lab that MNP-Mb spin adducts were unstable under

peptide mass mapping conditions since tryptic digests contained exclusively native Mb peptides (*78*). To overcome this problem, it was found necessary to reduce the spin adducts with ascorbate to form more stable diamagnetic mass adducts. Figure 7.1b shows the deconvolved mass spectrum of the species obtained following ascorbate reduction of the Mb/H_2O_2/DBNBS (1:5:20) reaction products. The reduced DBNBS-Mb (R-DBNBS-Mb) adducts exhibit an increased mass compared to native Mb of 328 ± 2 Da per R-DBNBS group vs 343 ± 2 Da DBNBS group, which would be consistent with loss of the nitroxide oxygen upon ascorbate reduction. The yield of R-DBNBS-Mb (65%) is slightly lower than that of DBNBS-Mb (70%), which is mainly due to loss of doubly-labeled Mb (Figure 7.1b). Ascorbate competition for radical sites is possible and in fact, it was observed by MALDI-TOF that increasing the amount of ascorbate (0.5-5.0 mM) present during the cyt c/H_2O_2/DBNBS reaction decreased the yield of DBNBS-labeled cyt c (*37*). Ascorbate, an effective antioxidant in vivo, readily reduces protein-based radicals since EPR-monitored DMPO-trapped radical intensity rapidly decreased when ascorbate was added to the human Mb/DMPO reaction prior to addition of H_2O_2 (*62*). Nonetheless, the yield of DBNBS-labeled Mb in the presence of ascorbate is comparable to that in its absence (Figure 7.1a vs. b,c). However, in the present experiments ascorbate was added 5 min after the Mb/H_2O_2/DBNBS reaction was initiated, which is 15-fold larger than the time (20 s) for the Mb/H_2O_2 reaction to be >99% complete, assuming k = 210 $M^{-1}s^{-1}$ (*48*).

Next, we investigated the effect on labeling yields of increasing the Mb/H_2O_2 molar ratio, while maintaining the Mb/DBNBS molar ratio at 1:20. Addition of 1 molar equivalent of H_2O_2 to Mb/DBNBS yielded 47% singly R-DBNBS-labeled and 3%

doubly-labeled Mb based on the relative peak intensities in Figure 7.1c. Thus, the yield of R-DBNBS labeling is decreased from 65 to 50% when the number of H_2O_2 molar equivalents is decreased from 10 to 1. The maximum yield of R-DBNBS-Mb occurs with 5 molar equivalents of H_2O_2 (data not shown), as a result, the pH dependence of DBNBS spin trapping was investigated using 1 and 5 molar equivalents of H_2O_2.

7.4.2 pH Dependence of DBNBS Spin Trapping in the Mb/H_2O_2 Reaction

DBNBS spin trapping experiments were carried out as a function of pH, since previous studies have demonstrated the pro-oxidative activity of Mb under acidic conditions (*53, 54*). It was reported that ≥ 2 molar equivalents of H_2O_2 are needed for oxidation of Mb to Fe^{IV}=O under acidic (pH 4.5) and basic (pH 8.0) conditions (*48, 172*). Actually, Mb is able to decompose 5-10 molar equivalents of H_2O_2 through its catalase-like activity without extensive oxidation of the globin (*48, 56*). Nonetheless, a green chromophore (λ_{max} = 584 nm), which has been assigned to a heme-Tyr103 crosslinked species, is reportedly formed in higher yields under acidic conditions (pH < 6.0) (*60*). Following incubation of Mb/H_2O_2/DBNBS (1:1:20) for 5 min at pH 5.0 and with ascorbate for an additional 30 min, both singly and doubly R-DBNBS labeled Mb dominate the deconvolved mass spectrum of the reaction products (Figure 7.2a). Increased labeling at pH 5.0 (65%) compared to pH 7.5 (50%) (Figure 7.2a vs 7.1c) suggests more extensive radical formation at low pH, consistent with the pH dependence of the EPR and UV/Vis spectra of the Mb/H_2O_2 (1:1.4) reaction products (*170*). The detection of (R-DBNBS)$_2$-Mb mass adducts indicates formation of two radical sites on

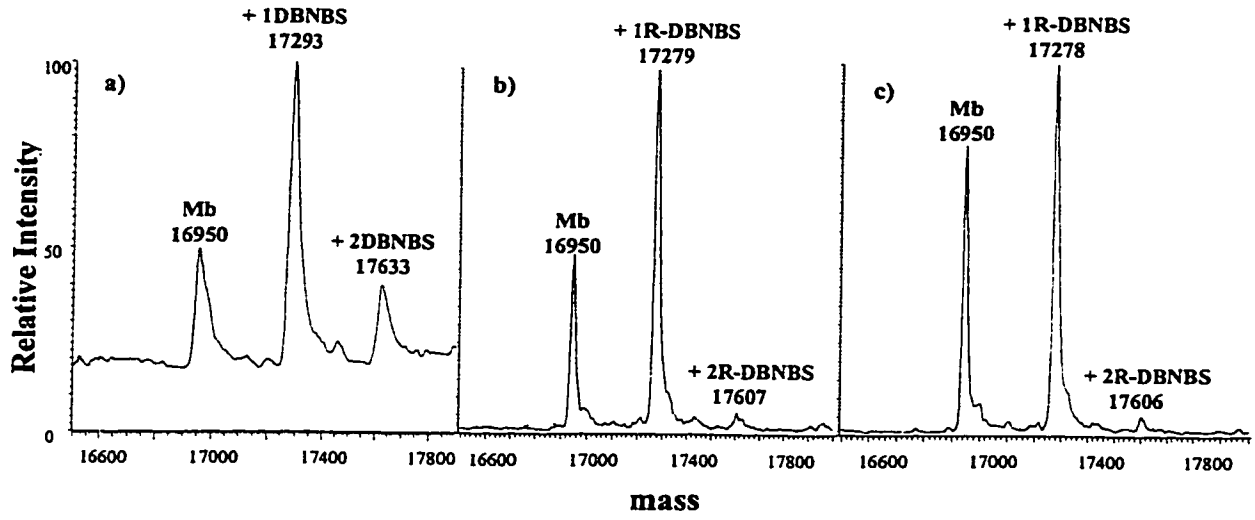

Figure 7.1. Deconvolved ESI mass spectra of the products of the reaction of 500 μM Mb and 10 mM DBNBS with (a) 2.5 mM H_2O_2, (b) 5.0 mM H_2O_2 and (c) 500 μM H_2O_2. Reactions were carried out in 50 mM ammonium acetate (pH 7.5) containing 200 μM DTPA for 5 min followed by a 30-min incubation with ascorbate in (b) and (c). The HPLC-purified reaction products were analyzed on-line by ESI-MS for molecular weight determination (see Experimental Procedures). R-DBNBS indicates that the DBNBS-Mb spin adducts have been reduced with ascorbate which results in loss of 15 Da [see Section 7.4.1 and (*78*)].

the polypeptide, as observed at pH 7.5. In addition to Tyr103 and Lys42, our group previously identified His64 as an alternate site of radical formation at pH 5.0 by ST/LC/MS using MNP (*78*). Likewise, Fox and coworkers concluded from pH-dependent changes in the UV/Vis spectrum of cow Mb that a histidyl radical was formed at acidic but not at neutral pH (*172*).

Increasing the H_2O_2 concentration in the Mb/H_2O_2/DBNBS (1:1:20) reaction at pH 5.0 to 5 molar equivalents produced predominately (R-DBNBS)$_2$-Mb mass adducts. The total yield of DBNBS-labeled Mb is ~ 80% (Figure 7.2b), consistent with increased radical formation in the presence of 5 molar equivalents of H_2O_2. The same effect is seen at pH 7.5 (Figure 7.1) and in the Mb/H_2O_2/DMPO reaction where ESI-MS analysis of the products revealed more extensive DMPO-labeling of Mb upon increasing H_2O_2 from 1 to 3 molar equivalents (*59*). The mass spectrum of the Mb/H_2O_2/DBNBS (1:5:20) reaction products at pH 6.6 also reveals 80% labeling but (R-DBNBS)-Mb and (R-DBNBS)$_2$-Mb adducts dominate the spectra at pH 6.6 and 5.0, respectively (Figure 7.2b vs 7.2c). Similarly, when the pH is increased to 8.65, 80% R-DBNBS-labeling is observed but (R-DBNBS)$_1$-Mb adducts are formed in the Mb/H_2O_2/DBNBS (1:5:20) reaction (Figure 7.2d). The varying yield of doubly R-DBNBS-labeled Mb suggests that the location, stability and/or accessibility of one of the radicals ($X^{\bullet}$) is highly pH dependent.

7.4.3 Peptide Mass Mapping of Mb/H_2O_2/DBNBS Reaction Products

Analysis of tryptic digests of Mb from the Mb/H_2O_2/DBNBS (1:5:20) reaction at pH 7.5 by LC/MS revealed R-DBNBS-labeled peptides that were not observed in the native digest (Figure 7.3a vs 7.3b). The doubly charged ions [$(M+2H)^{2+}$] observed in the

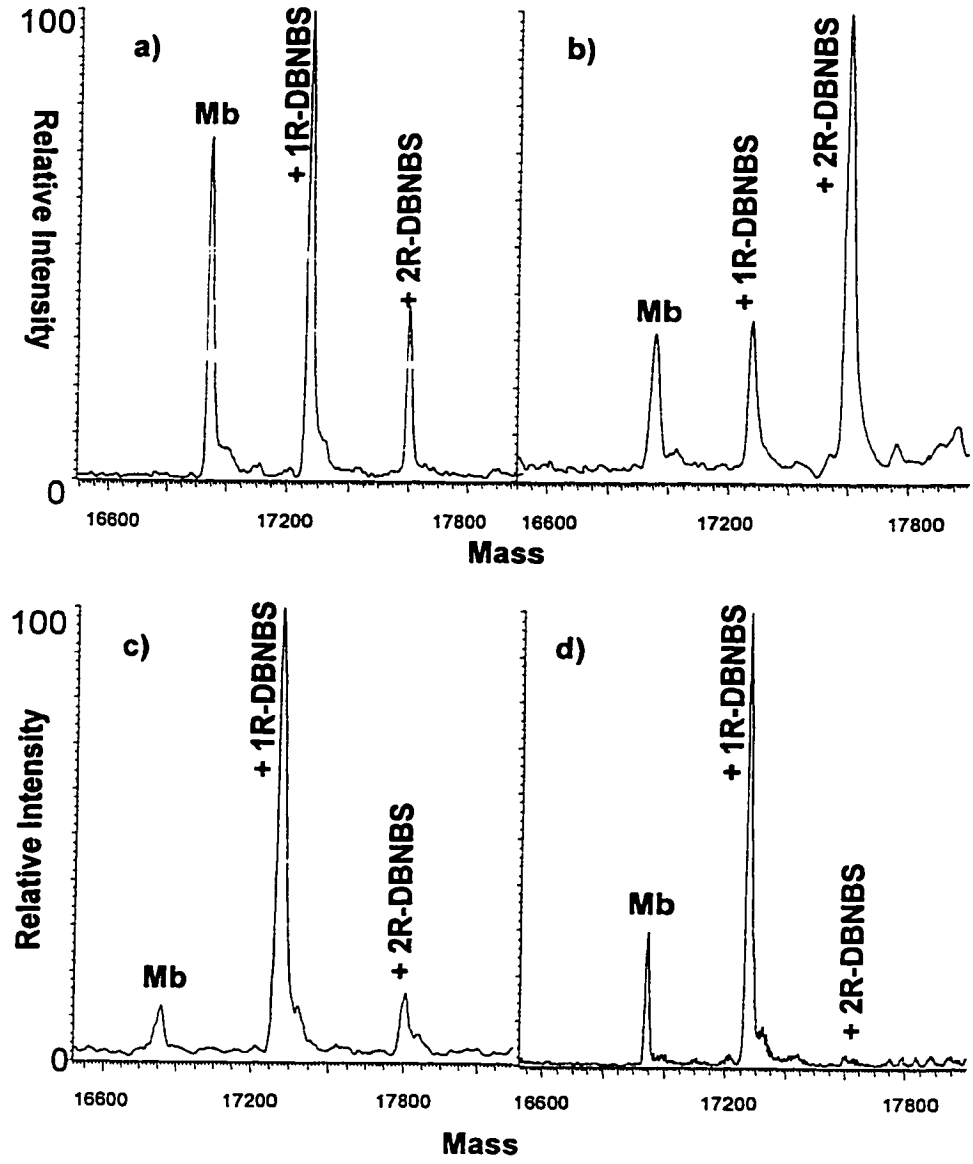

Figure 7.2. Deconvolved ESI mass spectra of the products of the reaction of 500 μM Mb and 10mM DBNBS with (a) 0.5 mM H_2O_2 at pH 5.0, (b) 2.5 mM H_2O_2 at pH 5.0, (c) 2.5 mM H_2O_2 at pH 6.6 and (d) 2.5 mM H_2O_2 at pH 8.65. The reactions were carried out in 50 mM ammonium acetate containing 200 μM DTPA for 5 min, followed by incubation with 5 mM ascorbate for 30 min.

XIC (Figure 7.3a) at *m/z* 1465.9 and 1108.2 correspond to peptides 97-118 (⊕, HKIPIKY LEFISDAIIHVLHSK) and 103-118 (⊗, YLEFISDAIIHVLHSK) plus 328 Da. This assignment is consistent with adduct formation on Tyr103 as seen previously with MNP (*78*) and the corresponding $(M+H)^+$ ions are observed at *m/z* 2214.578 and 2931.312 in the MALDI mass spectrum (Figure 7.4a vs 7.4b), corroborating the LC/ESI-MS results. The ion at *m/z* 2851.304 is a fragment ion of 2931.312 due to loss of SO_3 (80 Da), which has been also been reported for DBNBS-labeled peptides (*37*).

Post-source decay (PSD) was performed in the MALDI-TOF instrument to sequence peptide 97-118 (Figure 7.5a) to confirm the *specific site* of R-DBNBS labeling. Assignment of peaks in the PSD spectrum is somewhat tentative due to the large background signal. Nonetheless, Tyr103 can be inferred as the site of modification since the weak y_{16}^+ ion is R-DBNBS-labeled whereas the y_{15}^+ ion is unlabeled (Figure 7.5a, c). Collision induced dissociation (CID) of the R-DBNBS-labeled tryptic peptides was performed by LC/ESI-MS/MS and the y_{15}^{2+} ion is again unlabeled but a_1^+ ion a_2^+ ions containing the R-DBNBS label are observed (Figure 7.5b), consistent with Tyr103 as the site of the DBNBS-labeling. DBNBS-labeled peptide 24-45 (∅, HGQVELIRLFTGHPE TLEKFDK) was also observed, as seen from the XIC of the $(M+2H)^{2+}$ ion at *m/z* 1461.4 (Figure 7.3a). Based on our previous studies with MNP (*78*), labeling of Lys42 was inferred and inhibition of tryptic digestion at Lys42 would be consistent with labeling of this residue.

Lys45, Gly25 or Gly35 are also possible candidates for R-DBNBS labeling since glycine radicals have been identified in ribonucleotide reductase (*173*). CID sequencing of the modified peptide would resolve this issue, but unfortunately sequencing of the R-

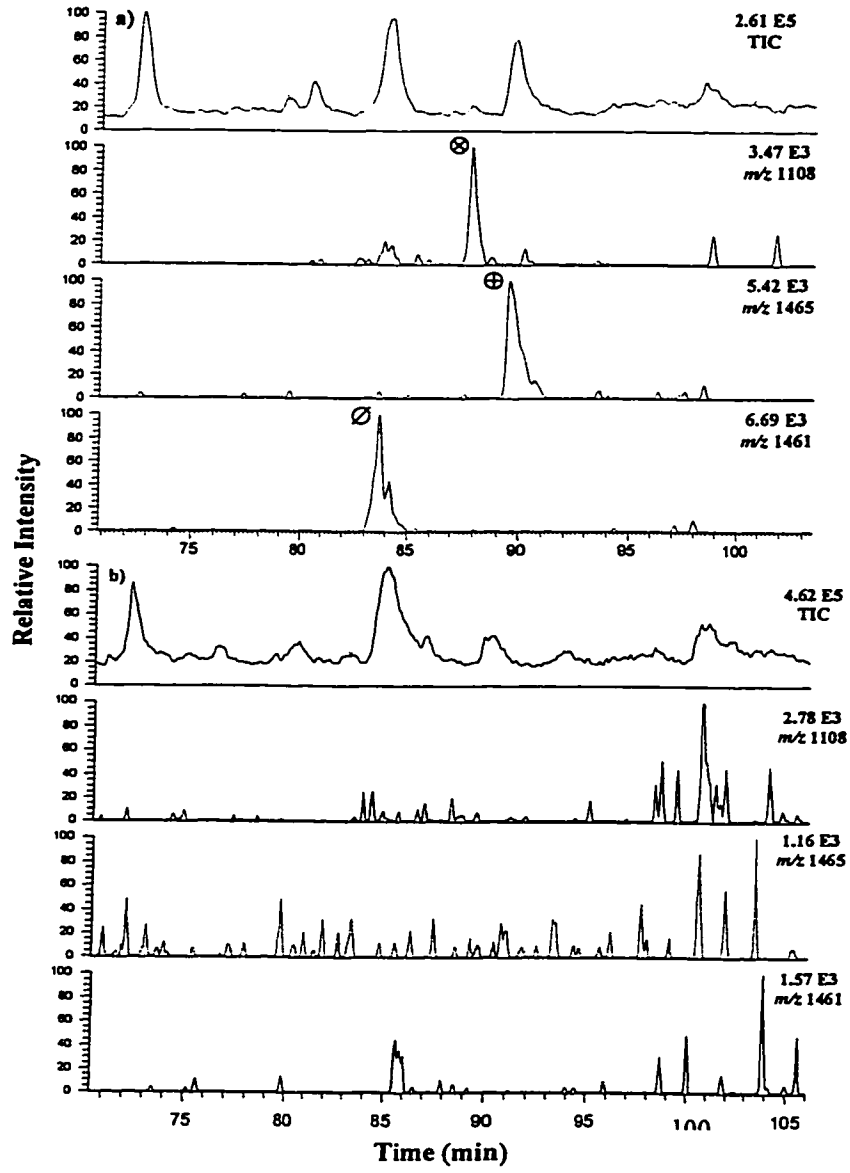

Figure 7.3. LC/ESI-MS peptide mass maps of (a) R-DBNBS-labeled Mb and (b) native Mb. Extracted ion chromatograms feature DBNBS-labeled peptides with m/z (⊗) 1108, (⊕) 1465, and (∅) 1461 that are not present in the native digest. Trapping conditions are given in Figure 7.1. R-DBNBS-labeled Mb was digested with trypsin (1:50 w/w) in ammonium acetate (pH 7.5) for 16 h at 25°C. The resulting tryptic peptides were separated on a Vydac microbore C_{18} column (1 x 250 mm) using a 5-55% ACN gradient elution in 0.05% TFA at 40 µl/min over 120 min and directly analyzed by ESI-MS.

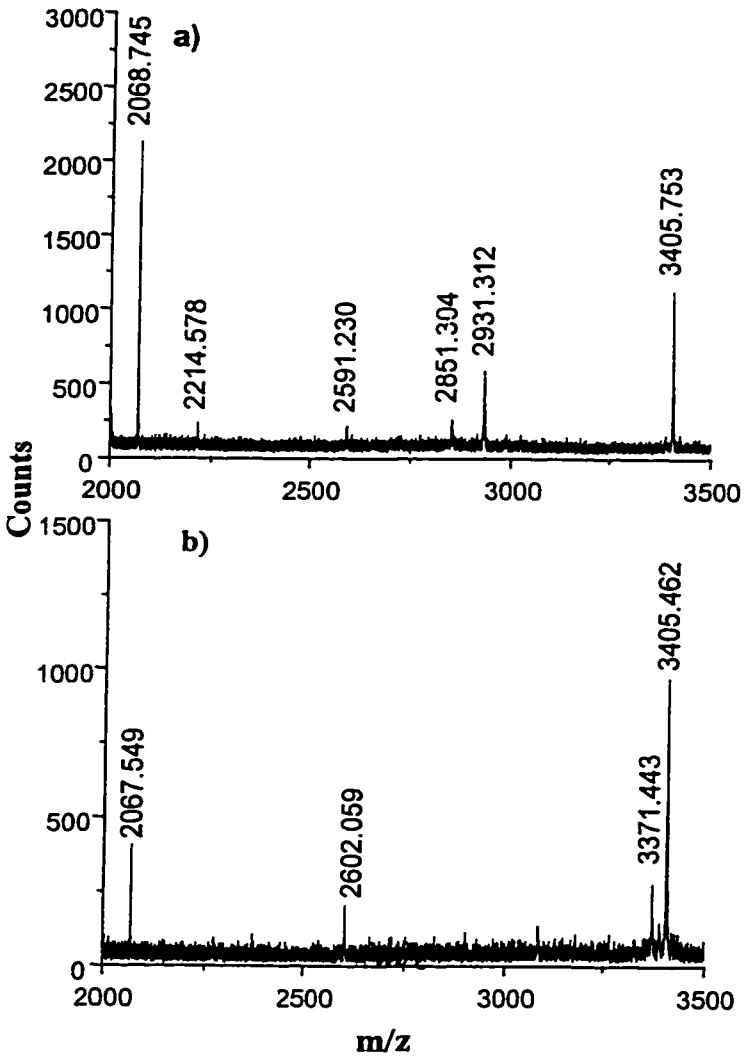

Figure 7.4. MALDI-TOF peptide mass maps of (a) R-DBNBS-labeled Mb and (b) native Mb. R-DBNBS-labeled Mb peptides 103-118 (m/z 2214.6) and 97-118 (m/z 2931.3) are observed. Trapping and tryptic digestion conditions are given in Figure 7.3. A 1:1 mixture of tryptic digest with a saturated solution of α-cyano-4-hydroxycinnamic acid in 45:45:10 ethanol:water:formic acid was spotted onto the MALDI target and co-crystallization was allowed to proceed at room temperature before peptide mass mapping was performed.

Figure 7.5. Mass spectrometric sequencing of R-DBNBS-modified tryptic peptide (a) 97-118 by MALDI PSD, (b) 103-118 by LC/MS/MS and (c) the predicted y and b fragment ions. Sequencing by LC/MS/MS was performed on a Micromass Quattro mass spectrometer following LC separation of the tryptic peptides on a Phenomonex Luna C_{18} column (50 x 4.6 mm) using a 5-50% ACN gradient elution in 0.1% TFA at 1 ml/min (1:5 split) over 20 min. The +3 ion at *m/z* 739 was selected in the first quadrupole and fragmented in the collision cell with Ar gas at 2.5 mTorr and collision energy of 25 V. The fragment ions were then analyzed in the third quadrupole. Sequencing by MALDI PSD was performed on a Bruker Bioflex III by selecting the +1 ion at *m/z* 2930 and fragmenting it using acceleration and reflectron voltages of 19 and 20 kV, respectively. Masses of the major ions a, b and y are indicated, and the fragment ions containing the R-DBNBS label are highlighted in bold.

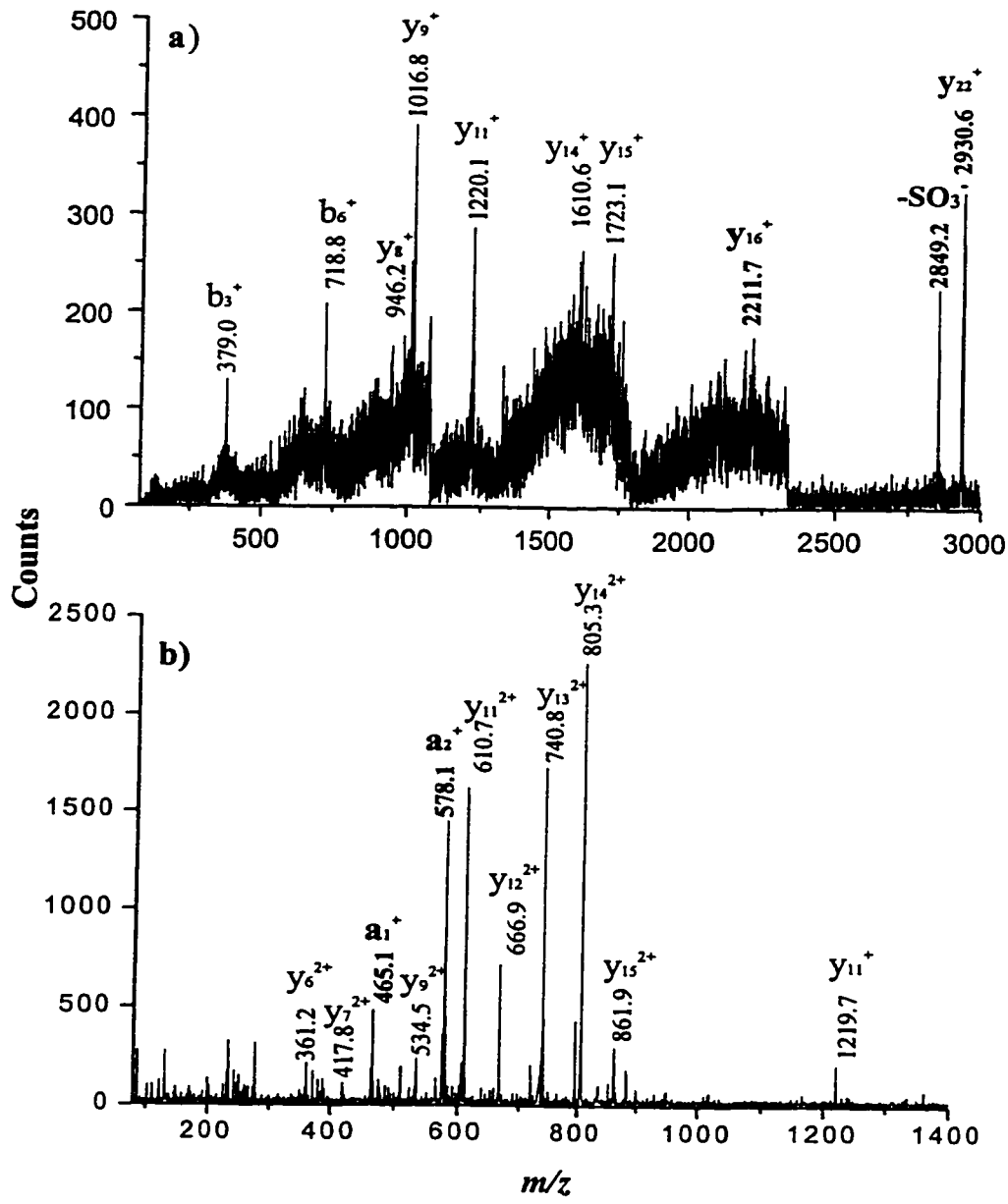

c) Residues 97-118

b_1	b_2	b_3	b_4	b_5	b_6	b_7	b_8	b_9	b_{10}	b_{11}	b_{12}	b_{13}	b_{14}	b_{15}	b_{16}	b_{17}	b_{18}	b_{19}	b_{20}	b_{21}
H	K	I	P	I	K	Y	L	E	F	I	S	D	A	I	I	H	V	L	H	S	K
y_{21}	y_{20}	y_{19}	y_{18}	y_{17}	y_{16}	y_{15}	y_{14}	y_{13}	y_{12}	y_{11}	y_{10}	y_9	y_8	y_7	y_6	y_5	y_4	y_3	y_2	y_1

DBNBS-labeled peptide 24-45 was unsuccessful due to poor ionization in the ESI source under the peptide mass mapping conditions. DBNBS contains a negatively charged sulfonate group that can chelate metal ions, and stronger signals were observed from DBNBS-labeled cyt c tryptic peptides that were purified on an immobilized metal affinity chromatography (IMAC) column containing either iron or gallium (*50*). Thus, in the future, IMAC fractionation should be performed to reduce suppression and/or enhance recovery of the R-DBNBS-labeled Mb peptides, which should allow both PSD and CID sequencing of labeled peptide 24-45.

R-DBNBS-labeled peptides 97-118, 103-118 and 24-45 were observed at all pHs examined. Despite the increased trapping efficiency of DBNBS at lower pH, sequencing of peptide 24-45 was unsuccessful. Furthermore, His64 was not identified as a radical site since peptide 64-77 (HGTVVLTALGGIILK) remained unlabeled following the Mb/H_2O_2/DBNBS reaction at pH 5.0. These results are inconsistent with our previous results obtained at pH 5.0 using MNP as a spin trap (*78*) since MNP-labeled peptide 64-77 was observed in the Mb/H_2O_2/MNP reaction. However, His64 was only observed when an HCl acidified acetone solution (pH 2.0) was added following spin trapping and ascorbate reduction. The acid-acetone procedure is used to extract the heme group of Mb (*60*), but its role in stabilizing histidine adducts needs to be investigated further.

7.4.4 *Absorption Difference Spectroscopy of Mb/H_2O_2 Reaction Products*

In Chapter 6 (*77*), we demonstrated that covalent DBNBS-protein adducts formed in the presence of H_2O_2 exhibit an absorption band at 302 nm. Trace 1 in Figure 7.6 shows that free DBNBS has an absorption maximum at 288 nm. The difference spectrum

of HPLC-purified products from the Mb/H_2O_2/DBNBS (1:5:20) reaction minus those from the Mb/H_2O_2 (1:5) reaction reveals loss of DBNBS absorption at 288 nm and growth of a new absorption band at 302 nm (Figure 7.6, trace 2). The band at 302 nm is similar to that seen for DBNBS-labeled cyt c (Figure 6.2, trace 3), and the red-shift is consistent with increased conjugation of the chromophore following trapping of a tyrosyl radical by the nitroso group of DBNBS. An estimate of ε_{302} (42 mM^{-1} cm^{-1}) for a DBNBS-tyrosine spin adduct is obtained by assuming 7x0% DBNBS-labeling of the tyrosine based on the relative area of the $(DBNBS)_1$-Mb peak in the deconvolved mass spectrum of the Mb/H_2O_2/DBNBS (1:5:20) reaction products (Figure 7.1a).

7.4.5 Analysis of Electron-transfer Pathways in Mb

Electron-transfer pathways in Mb were examined to pinpoint the oxidizable residues that have large electronic couplings to the heme center in Mb (Figure 7.7). Pathways analysis software, which estimates the electronic matrix element (T_{DA}) for very weak electron tunneling between donor (D) and acceptor (A) sites (*174*) was used for this purpose, where the larger the T_{DA}, the greater the probability for electron translocation. This method assumes that tunneling occurs via a dominant "pathway tube", where T_{DA} can be quantified as a product of contributions from through-space jumps, covalent bonds and hydrogen bonds [reviewed in (*175*)]. The pathways model does have some limitations since the paths are determined using the "frozen" crystallographic protein structure, without taking into account protein motions, and this model is accurate only when tunneling is dominated by a few pathway tubes that interfere constructively. The sensitivity of T_{DA} to protein conformation and dynamics increases when multiple pathway

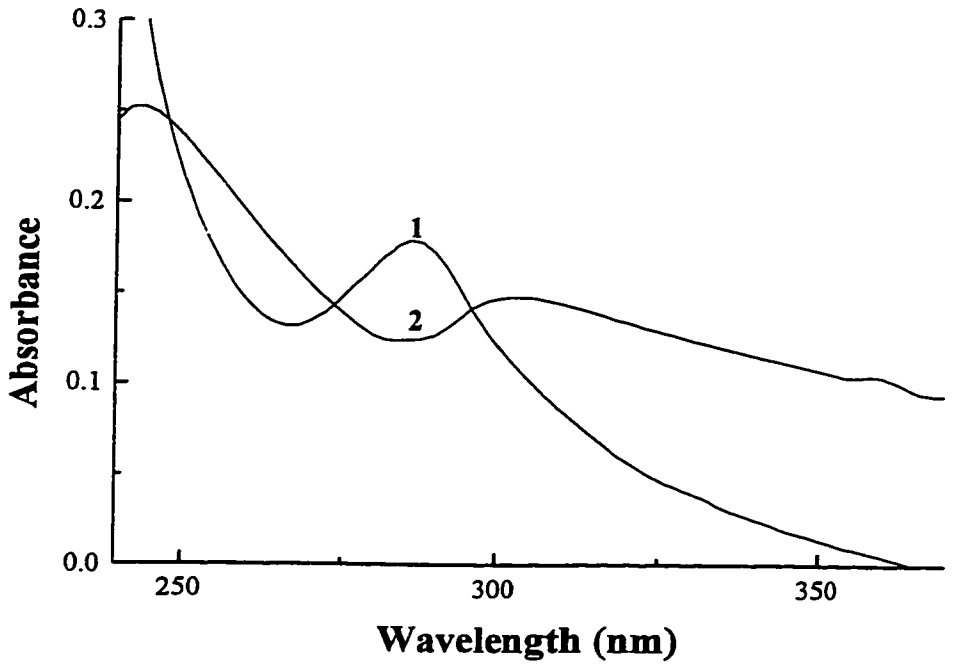

Figure 7.6. Absorption spectrum of 111 μM DBNBS (trace 1), and difference absorption spectrum of the HPLC-purified products from the Mb/H_2O_2/DBNBS (1:5:20) reaction minus those from the Mb/H_2O_2 (1:5) reaction (trace 2). Reactions containing 7 μM Mb were carried out in 50 mM ammonium acetate (pH 7.5) containing 200 μM DTPA and quenched after 5 min by separating protein products from salts and low-molecular-weight reactants by HPLC. Spectra were recorded in the same solution at a scan rate of 2400 nm/min and difference spectra were generated using Origin 3.0 software.

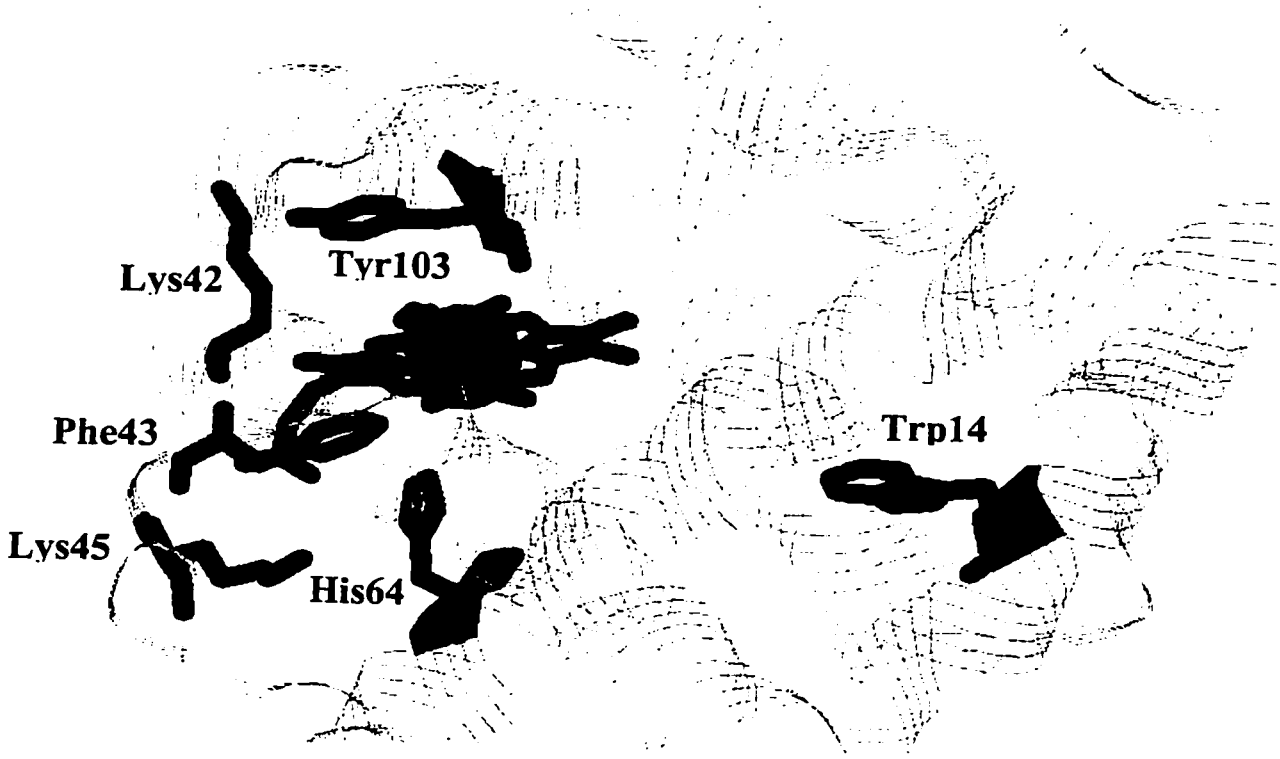

Figure 7.7. C_α backbone of horse heart myoglobin with its heme (red) and potential electron donors to the heme (black). The model was generated using Rasmol and the crystal structure coordinates from Protein Data Bank entry 1AZI.

tubes are destructively interfering. Nonetheless, the pathways model has been successfully used to identify electron-transfer pathways in a number of Mb derivatives with ruthenium-labeled surface histidines (*176*).

Under our experimental conditions, Tyr103 was confirmed as a major site of radical formation, while Lys42 was identified as a possible site. Pathways analysis reveals that the heme is strongly coupled to Tyr103 (0.039047), which is in van der Waals contact with heme edge (3.01 Å). Tyrosine residues (E° $TyrO^{\bullet}/TyrOH$ = 0.94 V) (*149*) are likely electron donors to Fe^{V}=O heme, which will have a reduction potential greater than that for the oxyferryl heme (E° Fe^{IV}=O/Fe^{III} ~ 1 V) (*81*). Furthermore, Tyr103 was recently proposed from EPR experiments to be the kinetically and/or thermodynamically most stable site for radical formation in Mb upon its reaction with H_2O_2 (*57, 58*).

Previously, MNP-labeled Lys42 was identified by ESI-MS (*78*) and DBNBS-labeled peptide 24-45 was identified here (Figure 7.3). Electron transfer from Lys42 to the heme is favourable, since the calculated T_{DA} is 0.019366 and it is within van der Waals contact with the heme (3.42 Å). However, electron transfer from Lys45 should be preferred over Lys42 due to its closer proximity to the heme edge (3.00 Å) and its calculated coupling to the heme (0.036000) is 2-fold greater than that of Lys42. Hence, as mentioned in Section 7.4.3, further work is necessary to identify the site of DBNBS-labeling on peptide 24-45, and to establish if MNP and DBNBS trap the same radicals at pH 5.0.

H_2O_2-oxidized Mb exhibits different EPR and UV/Vis spectra at pH 6.0 (*170*). In fact, it was demonstrated by ESI-MS that MNP labels His64 in the Mb/H_2O_2/MNP

reaction at pH 5.0 indicating that, in addition to Tyr103, there is also radical formation at this site at low pH (*78*). The His64-heme T_{DA} (0.025759) and separation (3.77 Å) are advantageous for electron transfer, but as mentioned in Section 7.4.3, DBNBS-labeled His64 was not detected in peptide mass maps of the products of the Mb/H_2O_2/DBNBS reaction at pH 5.0.

Phe43, which is located 3.24 Å from the distal heme edge where H_2O_2 binds to the heme iron (Figure 7.7), could also be considered a potential electron donor because it is electronically well coupled to the heme (0.026194). However, the reduction potential of free phenylalanine (E° $Phe^{\bullet}$/PheH = 1.6 – 1.9 V) (*57*) is beyond the reach of Mb/H_2O_2 (E° Fe^{IV}=O/Fe^{III} ~ 1 V) (*81*). On the other hand, the reduction potential of free tryptophan (E° $Trp^{\bullet}$/TrpH = 1.05 V) (*149*) is within reach of Mb/H_2O_2. Tryptophanyl radicals are formed during the enzymatic turnover of cytochrome c peroxidase and ribonucleotide reductase, and in the photoactivation of photolyase (*174*). Trp14 was proposed as the initial site of radical formation in the reaction of the W14F mutant of sperm whale Mb with H_2O_2 (*179*). Although site-directed mutagenesis can provide information on likely sites of the radical formation, it does have some drawbacks. Mutations can perturb protein stability and conformation, consequently affecting radical translocation along the polypeptide. For example, pathways analysis calculates a 200-fold higher T_{DA} for His64 (0.025476) vs Val64 (0.000804) coupling to the heme in Mb, whereas the calculated T_{DA} remains the same for Tyr103 (0.039047) vs Phe103 (0.039047) coupling to the heme. Furthermore, our ST/LC/MS data are inconsistent with radical formation at Trp14, since neither MNP (*78*) nor DBNBS labeling at this site was detected. Both the Trp14-heme distance (8.53 Å) and coupling (0.000059) are

unfavorable for electron-transfer between these sites compared to Tyr103, Lys42/45 or His64. Interestingly, Gebicki and coworkers (*180-182*) observed by iodometric titration that free lysine was peroxidized with greater efficiency than tryptophan upon exposure to hydroxyl free radicals. Thus, it is possible that the suggested Trp14 peroxyl radical observed by EPR (*160, 179*) is in fact a lysyl peroxyl radical.

7.5 Conclusions

The major spin-trapped radical formed during the Mb/H_2O_2 reaction at pH 7.5 is independent of the spin trap (MNP or DBNBS) used, since Tyr103 was observed to be labeled using both ST/LC/MS and ST/MALDI-MS techniques. However, labeling yields are strongly dependent on the trap used since DBNBS exhibits significantly higher trapping efficiencies compared to both MNP and DMPO. The increased formation of doubly vs singly DBNBS-labeled Mb at pH 5.0, suggests that (a) more radicals are formed, (b) radicals are more accessible to the spin traps, and/or (c) adducts are more stable. Identification by ESI-MS of MNP-His64 adducts only at low pH in the Mb/H_2O_2/MNP reaction would be consistent with (a), whereas (c) would be consistent with the observation that the chemical nature of MNP-Mb adducts affects their stability (*56, 78*). The well-documented "opening" of the heme crevice of Mb where the protonated form of the distal His64 residue swings out towards the solvent would be consistent with both (a) and (b) (*183, 184*). Finally, the increased DBNBS-labeling of Mb at pH 5.0 supports the reported greater pro-oxidant activity of Mb at low pH (*53, 54*).

Although it still remains to be established whether or not spin trapping at pH 5.0 is independent of the trap used, DBNBS appears to be the most effective trap used to date

with Mb. Future studies on mass spectral analysis of the sites that are DBNBS labeled should exploit the use of IMAC fractionation.

8.0 Conclusions and Suggestion for Future Work

8.1 Chapters 2, 3 and 4

Tryptic digestion of cyt c at various temperatures revealed that the local stability of horse and cow cyts c is greater than tuna cyt c, since they are both resistant to proteolytic digestion at 37°C, yet tuna cyt c is not. However, the increased rate of digestion of tuna cyt c is not simply explained by the number of Lys and Arg residues, since cow and horse cyts c both have 21 whereas tuna cyt c has only 17. Nevertheless, this is consistent with observed 695-nm T_cs at 35, 50 and 58°C for the thermally induced alkaline isomerization for horse, cow and tuna cyts c, respectively. Furthermore, the formation of a separate low-temperature isomer (35°C) of tuna cyt c does *not* involve the same ionization trigger nor the same conformational change as the alkaline isomerization above 50°C of horse and cow cyts c as monitored by FTIR. It is important to establish whether the locally unfolded forms detected *in vitro* are important in the physiological function of cyt c. The results reveal that the Met80 loop represents the site of greatest flexibility, which controls the local stability of all three cyts c examined here but has no effect on their global stability.

The sequential unfolding events of horse, cow and tuna cyt c as a function of increasing temperature were investigated by resolution-enhanced 2D IR correlation spectroscopy revealing that the overall sequence of unfolding is similar for all three cyts c. This occurs despite the different local stabilities observed in Chapters 2 and 3.

However, subtle differences were observed, such as unfolding of all helical components in cow cyt c occurs as one cooperative unit, whereas the helical components in horse and tuna cyts c unfold separately. Furthermore, the absence of stable extended-chain structures in tuna cyt c is consistent with a decreased heme-crevice stability of tuna cyt compared to the mammalian cyts c. Ultimately, the difference in the sequence of unfolding events and local stability in tuna compared to horse and cow cyts c can be linked to the less stable heme-crevice of the tuna protein due to amino acid substitutions affecting the flexibility about the Met80 loop. Finally, the studies performed in Chapters 3 and 4 highlight the power of FTIR spectroscopy in probing protein conformational changes. Particularly, selective thermal titration of amide II intensity in D_2O and resolution-enhanced 2D IR correlation can provide detailed information on secondary structure and tertiary folding intermediates.

8.2 Chapters 5 and 6

CN^- inhibition of heme bleaching and spin trapping of protein-based radicals by POBN in the cyt c/H_2O_2 reaction is consistent with Fe^{III}-mediated activation of H_2O_2 with subsequent reduction of Fe^{IV}=O by endogenous donors. However, heme intermediates are very short-lived ($t_{½}$ < 1 ms) and protein-based radicals are poorly trapped at pH 7.5, since Fe^{IV}=O is not detected in stopped-flow experiments and trapping efficiency is ~ 10-20% with MNP, DBNBS or DMPO, respectively. In contrast, compound I formation and trapping of a radical on Tyr103 are readily detected in Mb. With the ease of Tyr67 nitration by peroxynitrite (*150*) and its proximity to the heme (3.27 Å) it is believed that Tyr67 is an effective endogenous donor to the heme in cyt c analogous to Tyr103 in Mb.

However, radical translocation to Tyr74 in the horse and cow cyts c and Trp33 in tuna cyt c was inferred. Tyr74 and Trp33 are highly solvent exposed, consequently, radical generation on these exposed residues may play a role in triggering apoptosis (*140, 141*). Hence, unlike Tyr103 of Mb, our results reveal that the cyt c radicals are not very reactive and/or accessible at pH 7.5.

Noncovalent DBNBS adduct formation was predominately observed over trapping and showed specificity for cyt c since, its formation can not simply be correlated with the total number lysine residues (horse cyt c possesses 19, while horse Mb and cow α-lactalbumin have 19 and 12, respectively). The noncovalent adducts are due to electrostatic interactions between the negatively charged sulfonate group on DBNBS and positively charged surface residues on cyt c. Ion-pair formation between basic proteins and negatively charged probes may be a common interaction at low pH, therefore, it is essential to carry out the appropriate controls before interpreting MS data involving protein-probe adducts such as the $(DBNBS)_n$-cyt c adducts obtained in the present study.

8.3 Chapter 7

DBNBS trapping of protein-based radicals generated in the Mb/H_2O_2 reaction are similar to those found using MNP since, Tyr103 was identified as a radical site, yet its trapping efficiency is significantly better as found by ST/LC/MS and ST/MALDI-MS techniques. Hence, DBNBS appears to be the most effective trap used to date with Mb. The pH dependence of DBNBS trapping efficiency, where increased formation of doubly DBNBS-labeled Mb at low pH is observed, is consistent with the observed greater pro-oxidant activity of Mb at low pH (*53, 54*). This, suggests that either (a) more radicals are

formed, (b) radicals are more accessible to the spin traps, and/or (c) adducts are more stable.

8.4 Suggestions for Future Work

(1) Correlation between proteolytic susceptibility and heme-crevice stability of a larger set of cyts c could be performed to see if the results obtained with horse, cow and tuna cyts c are just an anomaly or if the Met80 loop truly does dictate the local stability of cyts c.

(2) FTIR monitoring of the thermal denaturation of mimetic cyt c alkaline isomers, such as lipid bound or experiments performed at pH 9, would further corroborate the results obtained with the CN^--cyt c adducts. The alkaline transition of mimetic cyt c alkaline isomers can also be monitored by 695-nm absorption and proteolytic susceptibility.

(3) Comparison of temperature- (performed in Chapter 4) vs pH-induced alkaline isomerization of cyt c by 2D IR would reveal if these two processes undergo similar unfolding mechanism or just result in similar end products.

(4) To increase the yield of cyt c adducts, labeled cyt c should be isolated by ion-exchange chromatography from the large amount of unlabeled protein and digested separately. This would prevent any labeled peptides from going undetected in a large excess of peptides from the unlabeled protein.

(5) After trypsin digestion cyt c can be separated from unlabeled tryptic peptides by IMAC. This would decrease suppression and/or enhance recovery of DBNBS-labeled tryptic peptides.

(6) Cyt c/H_2O_2 reactions should also be carried out using cyt c in its alkaline form (i.e., formed at 25°C and pH 9.0, at 55°C and pH 7.5 or in the presence of lipids), which may be more physiologically relevant than reactions carried out at 25°C and pH 7.5.

(7) It would be interesting to see if a spin trap-Trp difference absorption spectrum could be observed in tuna cyt c as seen with the DBNBS-Tyr difference spectrum in horse cyt c since this would allow a very simple spectroscopic tool to detect spin adduct formation in proteins.

9.0 References

1. Moore, G. R., and Pettigrew, G. W. (1990) *Cytochromes c-Evolutionary, Structural and Physiochemical Aspects*, Springer-Verlag, Berlin.
2. Bushnell, G. W., Louie, G. V., and Brayer, G. D. (1990) *J. Mol. Biol. 214*, 585.
3. Dickerson, R. E. (1980) *Sci. Am. 242*, 137.
4. Kaminsky, L. S., Miller, V. J., and Davison, A. J. (1973) *Biochemistry 12*, 2215.
5. Schejter, S., and George, P. (1964) *Biochemistry 3*, 1045.
6. Theorell, H., and Akesson, A. (1941) *J. Am. Chem. Soc. 63*, 1812.
7. Angstrom, J., Moore, G. R., and Williams, R. J. P. (1982) *Biochim. Biophys. Acta 703*, 87.
8. Pettigrew, G. W., Aviram, I., and Schejter, A. (1975) *Biochem. J. 149*, 155.
9. Endo, S., Nagayama, K., and Wada, A. (1985) *J. Biomol. Struct. Dyn. 3*, 409.
10. Hu, Y., Fenwick, C., and English, A. M. (1996) *Inorg. Chimica Acta 242-243*, 1.
11. Filosa, A., and English, A. M. (2000) *J. Biol. Inorg. Chem. 5*, 448.
12. Schejter, A., Luntz, T. L., Koshy, T. I., and Margoliash, E. (1992) *Biochemistry 31*, 8336.
13. Taler, G., Schejter, A., Navon, G., Vig, I., and Margoliash, E. (1995) *Biochemistry 34*, 14209.
14. Davis, L. A., Schejter, A., and Hess, G. P. (1974) *J. Biol. Chem. 249*, 2624.
15. Ferrer, J. C., Guillemette, J. G., Bogumil, R., Inglis, S. C., Smith, M., and Mauk, A. G. (1993) *J. Am. Chem. Soc. 115*, 7507.

16. Dopner, S., Hilderbrandt, P., Rosell, F. I., and Mauk, A. G. (1998) *J. Am.. Chem. Soc. 120*, 11246.

17. Hong, X. L., and Dixon, D. W. (1989) *FEBS Lett. 246*, 105.

18. Rosell, F. I., Ferrer, J. C., and Mauk, A. G. (1998) *J. Am. Chem. Soc. 120*, 11234.

19. Smith, H. T., and Millett, F. (1980) *Biochemistry 19*, 1117.

20. Hildebrandt, P., Heimburg, T., Marsh, D., and Powell, G. L. (1990) *Biochemistry 29*, 1661.

21. Heimburg, T., and Marsh, D. (1993) *Biophys. J. 65*, 2408.

22. Kimelberg, H. K., and Lee, C. P. (1970) *J. Membr. Biol. 2*, 252.

23. Liu, X., Kim, C. N., Yang, J., Jemmerson, R., and Wang, X. (1996) *Cell 86*, 147.

24. Jemmerson, R., Liu, J., Hausauer, D., Lam, K. P., Mondino, A., and Nelson, R. D. (1999) *Biochemistry 38*, 3599.

25. Matsuyama, S., Llopis, J., Deveraux, Q. L., Tsien, R. Y., and Reed, J. C. (2000) *Nat. Cell Biol. 2*, 318.

26. Garland, J. M., and Rudin, C. (1998) *Blood 4*, 1235.

27. Kluck, R. M., Martin, S. J., Hoffman, B. M., Zhou, J. S., Green, D. R., and Newmeyer, D. D. (1997) *EMBO J. 16*, 4639.

28. Hampton, M. B., Zhivotovsky, B., Slater, A. F. G., Burgess, D. H., and Orrenius, S. (1998) *Biochem. J. 329*, 95.

29. Chance, B., Sies, H., and Boveris, A. (1979) *Physiol. Rev. 59*, 527.

30. Radi, R., Turrens, J. F., and Freeman, B. A. (1991) *Arch. Biochem. Biophys. 288*, 118.

31. Radi, R., Bush, K. M., and Freeman, B. A. (1993) *Arch. Biochem. Biophys. 300*, 409.

32. Lenaz, G. (1998) *Biochim. Biophys. Acta 1366*, 53.

33. Stradtman, E. R. (1992) *Science 257*, 1220.

34. Yakes, F. M., and Van Houten, B. (1997) *Proc. Nat. Acad. Sci. USA 94*, 514.

35. Mignotte, B., and Vayssiere, J. (1998) *Eur. J. Biochem. 252*, 1.

36. Stridh, H., Kimlanf, M., Jones, D. P., Orrenius, S., and Hampton, M. B. (1998) *Febs Lett. 429*, 351.

37. Deterding, L. J., Barr, D. P., Mason, R. P., and Tomer, K. B. (1998) *J. Biol. Chem. 273*, 12863.

38. Radi, R., Thomson, L., Rubbo, H., and Prodanov, E. (1991) *Arch. Biochem. Biophys. 288*, 112.

39. Galaris, D., Sevanian, A., Cadenas, E., and Hochstein, P. (1990) *Arch. Biochem. Biophys. 281*, 163.

40. Aust, S. D., Morehouse, L. A., and Thomas, C. E. (1985) *Free Radic. Biol. Med. 1*, 3.

41. Florence, T. M. (1985) *J. Inorg. Biochem. 23*, 131.

42. Villegas, J. A., Mauk, A. G., and Vazquez-Duhalt, R. (2000) *Chem. Biol. 7*, 237.

43. Radi, R., Turrens, J. F., Chang, L. Y., Bush, K. M., Crapo, J. D., and Freeman, B. A. (1991) *J. Biol. Chem. 226*, 22028.

44. Filosa, A., and English, A. M. (1999) *Proceedings of the 47th ASMS Conference on Mass Spectrometry and Allied Topics*, Dallas, TX.

45. Barr, D. P., Gunther, M. R., Deterding, L. J., and Tomer, K. B. (1996) *J. Biol. Chem. 271*, 15498.

46. Barr, D. P., and Mason, R. P. (1995) *J. Biol. Chem. 21*, 12709.

47. English, A. M., and Tsaprailis, G. (1995) *Advances in Inorganic Chemsitry 43*, 75.

48. Yonetani, T., and Schleyer, H. (1967) *J. Biol. Chem. 242*, 1974.

49. Tajima, G.-I., and Shikama, K. (1993) *Int. J. Biochem. 25*, 101.

50. Deterding, L. J., Chen, Y. R., Cutalo, J. M., Mason, R. P., and Tomer, K. B. (2000) *Proceedings of the 48th ASMS Conference on Mass Spectrometry and Allied Topics*, Long Beach, CA.

51. Slezak, J., Pan, H.-L., Stahl, G. L., and Longhurst, J. C. (1995) *Am. J. Pathol. 147*, 772.

52. Arduini, A., Eddy, L., and Hochstein, P. (1990) *Free Radic. Biol. Med. 9*, 511.

53. Fantone, J., Jester, S., and Loomis, T. (1989) *J. Biol. Chem. 264*, 9408.

54. Rodriguez-Malaver, A. J., Leake, D. S., and Rice-Evans, C. A. (1997) *FEBS Lett. 406*, 37.

55. Filosa, A., and English, A. M. (2000) *Proceedings of the 48th ASMS Conference on Mass Spectrometry and Allied Topics*, Long Beach, CA.

56. Fenwick, C. W. (1997) *Ph. D. Thesis,* Concordia University, Montreal, Canada.

57. Giulivi, C., and Cadenas, E. (1998) *Free Radic. Biol. Med. 24*, 269.

58. Gunther, M. R., Sturgeon, B. E., and Mason, R. P. (2000) *Free Radic. Biol. Med. 28*, 709.

59. Gunther, M. R., Tschirret-Guth, R. A., Witkowska, H. E., Fann, Y. C., Barr, D. P., Ortiz De Montellano, P. R., and Mason, R. P. (1998) *Biochem. J. 330*, 1293.

60. Catalano, C. E., Choe, Y. S., and Ortiz de Montellano, P. R. (1989) *J. Biol. Chem. 264*, 10534.

61. Van der Zee, J. (1997) *Biochem. J. 322*, 633.

62. Witting, P. K., Douglas, D. J., and Mauk, A. G. (2000) *J. Biol. Chem. 275*, 20391.

63. Haris, P. I., and Chapman, D. (1992) *Trends Biochem. Sci. 17*, 328.

64. Haris, P. I., and Chapman, D. (1995) *Biopolymers 37*, 251.

65. Dong, A. C., Huang, P., and Caughey, W. S. (1992) *Biochemistry 31*, 182.

66. Surewicz, W. K., and Mantsch, H. H. (1988) *Biochim. Biophys. Acta 952*, 115.

67. de Jongh, H. H., Goormaghtigh, E., and Ruysschaert, J. M. (1995) *Biochemistry 34*, 172.

68. Holzbaur, I. E., English, A. M., and Ismail, A. A. (1996) *Biochemistry 35*, 5488.

69. Fabian, H., Mantsch, H. H., and Schultz, C. (1999) *Proc. Nat. Acad. Sci. USA 96*, 13153.

70. Wang, Y., Murayama, K., Myojo, Y., Tsenkova, R., Hayashi, N., and Ozaki, Y. (1998) *J. Phys. Chem. B 102*, 6655.

71. Noda, I. (1993) *Appl. Spectrosc. 47*, 1329.

72. Perkins, M. J. (1980) *Advances in Physical Organic Chemistry 17*, Academic Press, Toronto, 1.

73. Eberson, L. (1998) *Advances in Physical Organic Chemistry 31*, Academic Press, Toronto, 91.

74. Iwahashi, H., Parker, C. E., Mason, R. P., and Tomer, K. B. (1990) *Rapid. Commun. Mass Spectrom. 4*, 352.

75. Iwahashi, H., Parker, C. E., Mason, R. P., and Tomer, K. B. (1991) *Biochem. J. 276*, 447.

76. Janzen, E. G., Towner, R. A., Krygsman, P. H., Lai, E. K., Poyer, J. L., Brueggemann, G., and McCay, P. B. (1990) *Free Rad. Res. Commun. 9*, 353.

77. Filosa, A., and English, A. M. (2001) *J. Biol. Chem.* (in press)

78. Fenwick, C. W., and English, A. M. (1996) *J. Am. Chem. Soc. 118*, 12236.

79. Tsapraillis, G. (1997) *Ph. D. Thesis,* Concordia University, Montreal, Canada.

80. Tomasi, A., and Iannone, A. (1993) *Biological Magnetic Resonance: EMR of Paramagnetic Molecules 13*, Plenum Press, New York, 353.

81. Koppenol, W. H. (1983) *J. Phys. Chem. 88*, 99.

82. Hiramoto, K., Hasegawa, Y., and Kikugawa, K. (1994) *Free Rad. Res. 21*, 341.

83. Eaton, W. A. and Hochstrasser, R. M. (1967) *J. Chem. Phys. 46*, 2533.

84. Myer, Y. P., MacDonald, L. H., Verma, B. C. and Pande, A. (1980) *Biochemistry 19*, 199.

85. Yuan, X., Hawkridge, F. M. and Cheblowski, J. F. (1993) *J. Electroanal. Chem. 350*, 29.

86. Jaenicke, R. andRudolph, R. (1990) *Protein Structure-A Practical Approach*, IRL Press, Oxford.

87. Hubbard, S. J., Campbell, S. F. and Thornton, J. M. (1991) *J. Mol. Biol. 220*, 507.

88. Bai, Y., Sosnick, T. R., Mayne, L. and Englander, S. W. (1995) *Science 269*, 192.

89. Hu, Y. (1994) *M. Sc. Thesis*, Concordia University, Montreal, Canada.

90. Babul, J. and Stellwagen, E. (1972) *Biochemistry 11*, 1195.

91. Gadsby, P. M., Peterson, J., Foote, N., Greenwood, C. and Thomson, A. J. (1987) *Biochem. J. 246*, 43.

92. Santucci, R., Giartosio, A. and Ascoli, F. (1989) *Arch. Biochem. Biophys. 275*, 496.

93. Filosa, A., Ismail, A. A. and English, A. M. (1999) *J. Biol. Inorg. Chem. 4*, 717.

94. Schejter, A., Koshy, T. I., Luntz, T. L., Sanishvili, R., Vig, I. And Margoliash, E. (1994) *Biochem. J. 302*, 95.

95. Schejter, A., Zuckerman, M. and Aviram, I. (1979) *J. Biol. Chem. 254*, 7042.

96. Wilson, M.T. and Greenwood, C. (1996) *Cytochrome c-A Multidisciplinary Approach*, University Science Books, Sausalito.

97. Myer, Y. P. and Saturno, A. F. (1991) *J. Protein Chem. 10*, 481.

98. Saigo, S. (1981) *Biochim. Biophys. Acta 669*,13.

99. Vitello, L. B., Erman, J. E., Miller, M. A., Mauro, J. M. and Kraut, J. (1992) *Biochemistry 31*, 11524.

100. Harrington, J. P. (1981) *Biochim. Biophys. Acta 671*, 85.

101. Osterhout, J. J., Jr., Muthukrishnan, K. and Nall, B. T. (1985) *Biochemistry 24*, 6680.

102. Schroeder, H. R., McOdimba, F. A., Guillemette, J. G. and Kornblatt, J. A. (1997) *Biochem. Cell Biol. 75*, 191.

103. Moore, G. R. and Williams, R. J. (1980) *Eur. J. Biochem. 103*, 523.

104. Moore, G. R. and Williams, R. J. (1980) *Eur. J. Biochem. 103*, 533.

105. Gao, Y., Lee, A. D., Williams, R. J. and Williams, G. (1989) *Eur. J. Biochem. 182*, 57.

106. Fredericks, Z. L. and Pielak, G. J. (1993) *Biochemistry 32*, 929.

107. Osheroff, N., Borden, D., Koppenol, W. H. and Margoliash, E. (1980) *J. Biol. Chem. 255*, 1689.

108. Battistuzzi, G., Borsari, M., Sola, M. and Francia, F. (1997) *Biochemistry 36*, 16247.

109. Takano, T. and Dickerson, R. E. (1981) *J. Mol. Biol. 153*, 79.

110. Martinez, G. and Millhauser, G. (1995) *J. Struct. Biol. 114*, 23.

111. van Stokkum, I. H. M., Lindsell, H., Hadden, J. M., Haris, P. I., Chapman, D. and Bloemandal, M. (1995) *Biochemistry 34*, 10508.

112. George, P. and Tsou, C. L. (1952) *Biochem. J. 50*, 1568.

113. Dyer, C., Schubert, A., Timkovich, R. and Feinberg, B. (1979) *Biochim. Biopys. Acta 579*, 253.

114. Wuthrich, K. (1969) *Proc. Natl. Acad. Sci. USA 63*, 1071.

115. Dickerson, R. E. and Timkovich, R. (1975) *The Enzymes XI*. Academic Press, New York.

116. Aviram, I. and Schejter, S. (1980) *J. Biol. Chem. 255*, 3020.

117. Dong, A., Huang, P. and Caughey, W. S. (1990) *Biochemistry 29*, 3303.

118. Ernst-Fonberg, M. L., Worsham, L. M. S. and Williams, S. G. (1993) *Biochim. Biophys. Acta 1164*, 273.

119. Hadden, J. M., Bloemendal, M., Haris, P. I., Srai, S. K. S. and Chapman, D. (1994) *Biochim. Biopys. Acta 1205*, 59.

120. Zhang, Z. and Smith, D. L. (1993) *Protein Science 2*, 522.

121. McLendon, G. and Smith, M. (1978) *J. Biol. Chem. 253*, 4004.

122. Susi, H. and Byler, D. M. (1986) *Methods Enzymol. 130*, 290.

123. Qi, P. X., Beckman, R. A. and Wand, A. J. (1996) *Biochemistry 35*, 12275.

124. Venyaminov, S. Y. and Kalnin, N. N. (1990) *Biopolymers 30*, 1259.

125. Dousseau, F. and Pezolet, M. (1990) *Biochemistry 29*, 8771.

126. Prestrelski, S. J., Byler, D. M. and Thompson, M. P. (1991) *Int. J. Pept. Protein Res. 37*, 508.

127. Dwividi, A. M. and Krimm, S. (1984) *Biopolymers 23*, 922.

128. Kennedy, D. F., Crisma, M., Toniolo, C. and Chapman, D. (1991) *Biochemistry 30*, 6541.

129. Mantsch, H. H., Perczel, A. H. and Fasman, G. D. (1993) *Biopolymers 33*, 201.

130. Scheiner, S. and Cuma, M. (1996) *J. Am. Chem. Soc. 118*, 1511.

131. Brandon, C. and Tooze, J. (1991) *Introduction to Protein Structure*, Garland Publishing, Inc., New York.

132. Chou, P. Y. and Fasman, G. D. (1990) *Biochemistry*, Benjamin/Cummings Publishing Company, Inc., New York.

133. Behere, D. V., Ales, D. C. and Goff, H. M. (1986) *Biochim. Biophys. Acta 871*, 285.

134. Ismoyo, F., Wang, Y., and Ismail, A. A. (2000) *Appl. Spectrosc. 54*, 939.

135. Clark, A. H., Saunderson, D. H., and Suggett, A. (1981) *Int. J. Peptide Protein Res. 17*, 353.

136. Jackson, and Mantsch, H. H (1995) *Crit. Rev. Biochem. Mol. Biol. 30*, 95.

137. Ismail, A. A., Mantsch, H. H., and Wong, P. T. T. (1992) *Biochim. Biophys. Acta 1121*, 183.

138. Boye, J. I., Alli, I., Ismail, A. A., Gibbs, B. F., and Konishi, Y. (1995) *Int. Dairy J. 5*, 337.

139. Milne, J. S., Xu, Y., Mayne, L. C., and Englander, S. W. (1999) *J. Mol. Biol. 290*, 811.

140. Nomura, K., Imai, H., Koumura, T., Kobayashi, T., and Nakagawa, Y. (2000) *Biochem. J. 351*, 183-193.

141. Shidoji, Y., Hayashi, K., Komura, S., Ohishi, N., and Yagi, K. (1999) *Biochem. Biophys. Res. Commun. 264*, 343.

142. Harel, S., Salan, M. A., and Kanner, J. (1988) *Free Radic. Res. Commun. 5*, 11.

143. Torres, E., Sandoval, J. V., Rosell, F. I., Mauk, A. G., and Vazquez-Duhalt, R. (195) *Enzyme Microb. Technol. 17*, 1014.

144. Vazquez-Duhalt, R., westlake, D. W. S., and Fedorak, P. M. (1993) *Enzyme Microb. Technol. 15*, 494.

145. Kagan, V. E., Fabisiak, J. P., Shvedova, A. A., Tyurina, Y. Y., Tyurin, V. A., Schor, N. F., and Kawai, K. (2000) *FEBS Lett. 477*, 1.

146. Nantes, I. L., Faljoni-Alario, A., Nascimento, O. R., Bandy, B., Gatti, R., and Bechara, E. J. (2000) *Free Radic. Biol. Med. 28*, 786.

147. Anni, H., and Israel, Y. (1999) *Alcohol Clin. Exp. Res. 23*, 26.

148. Blodig, W., Smith, A. T., Winterhalter, K., and Piontek, K. (1999) *Arch. Biochem. Biophys. 370*, 86.

149. DeFillipis, M. R., Murthy, C. P., Broitman, F., Weinraub, D., Faraggi, M., and Klapper, M. H. (1991) *J. Phys. Chem. 95*, 3416.

150. Cyt c nitration

151. Kaur, H., Leung, K. H. W., and Perkins, M. J. (1981) *J. Chem. Soc. Chem. Commun.*, 142.

152. Kalyanaraman, B., Joseph, J., Kondratenko, N., and Parthasarathy, S. (1992) *Biochim. Biophys. Acta 1126*, 309.

153. Goto, Y., Takahashi, N., and Fink, A. L. (1990) *Biochemistry 29*, 3480.

154. Ali, V., Prakash, K., Kulkarni, S., Ahmad, A., Madhusudan, K. P., and Bhakuni, V. (1999) *Biochemistry 38*, 13635.

155. Blumenthal, D. C., and Kassner, R. J. (1980) *J. Biol. Chem. 255*, 5859-5863.

156. Kim, Y. M., Jeong, S. H., Yamazaki, I., Piette, L. H., Han, S., and Hong, S. J. (1995) *Free Rad. Res. 22*, 11.

157. Mason, R. P., Kalyanaraman, B., Tainer, B. E., and Eling, T. E. (1980) *J. Biol. Chem. 255*, 5019.

158. Nazhat, N. B., Saadalla-Nazhat, R. A., Fairburn, K., Jones, P., Blake, D. R., Nielsen, B. R., Symons, M. C., and Winyard, P. G. (1999) *Biochim. Biophys. Acta 1427*, 276.

159. Chen, Y. R., Gunther, M. R., and Mason, R. (1999) *J. Biol. Chem. 274*, 3308.

160. Gunther, M. R., Kelman, D. J., Corbett, J. T., and Mason, R. P. (1995) *J. Biol. Chem. 270*, 16075.

161. Kohno, M., Yamada, M., Mitsuta, K., Mizuta, Y., and Yoshikawa, T. (1991) *Bull. Chem. Soc. Jpn. 64*, 1447.

162. Ozawa, T., and Hanaki, A. (1991) *Bull. Chem. Soc. Jpn. 64*, 1976.

163. Righetti, P. G., and Caravaggio, T. (1976) *J. Chromatogr. 127*, 1.

164. George, P., and Irvine, D. H. (1952) *Biochem. J. 52*, 511.

165. Matulis, D., and Lovrien, R. (1998) *Biophys. J. 74*, 422.

166. Irwin, J. A., Ostdal, H., and Davies, M. J. (1999) *Arch. Biochem. Biophys. 362*, 94.

167. Baron, C. P., Skibsted, L. H., and Andersen, H. J. (2000) *Free Radic. Biol. Med. 28*, 549.

168. Newman, E. S., Rice-Evans, C. A., and Davies, M. J. (1991) *Biochem. Biophys. Res. Commun. 179*, 1414.

169. Miura, T., Muraoka, S., and Ogiso, T. (1995) *Biochem. Mol. Biol. Int. 36*, 587.

170. King, N. K., and Winfield, M. E. (1966) *Aust. J. Biol. Chem. 19*, 211.

171. Davies, M. J. (1988) *Biochim. Biophys. Acta 964*, 28.

172. Fox, J. B. J., Nicholas, R. A., Ackerman, S. A., and Swift, C. E. (1974) *Biochemistry 13*, 5178.

173. Gunther, M. R., Sampath, V., and Caughey, W. S. (1999) *Free Radic. Biol. Med. 26*, 1388.

174. Stubbe, J., and van der Donk, W. A. (1998) *Chem. Rev. 98*, 705.

175. Betts, J. N., Beratan, D. N., and Onuchic, J. N. (1992) *J. Am. Chem. Soc. 114*, 4043.

176. Nocek, J. M., Zhou, J. S., De Forest, S., Priyadarshy, S., Beratan, D. N., Onuchic, J. N., and Hoffman, B. M. (1996) *Chem. Rev. 96*, 2459.

177. Roitberg, A. E., Holden, M. J., Mayhew, M. P., Kurnikov, I. V., Beratan, D. N., and Vilker, V. L. (1998) *J. Am. Chem. Soc. 120*, 8927.

178. Casimiro, D. R., Wong, L.-L., Colon, J. L., Zewert, T. E., Richards, J. H., Chang, I.-J., Winkler, J. R., and Gray, H. B. (1993) *J. Am. Chem. Soc. 115*, 1485.

179. DeGray, J. A., Gunther, M. R., Tschirret-Guth, R., Ortiz de Montellano, P. R., and Mason, R. P. (1997) *J. Biol. Chem. 272*, 2359.

180. Sosynski, M., Filipiak, A., Bartosz, G., and Gebicki, J. M. (1996) *Free Radic. Biol. Med. 20*, 45.

181. Gebicki, S., and Gebicki, J. M. (1993) *Biochem. J. 289*, 743.

182. Gebicki, S., Bartosz, G., and Gebicki, J. M. (1995) *Biochem. Soc. Trans. 23*, 249S.

183. Morikis, D., Champion, M. P., Springer, B. A., and Sligar, S. G. (1989) *Biochemistry 28*, 4791.

184. Tian, W. D., Sage, J. T., and Champio, P. M. (1993) *J. Mol. Biol. 233*, 155.